Molecular Dynamics Investigation on Production and Utilisation of Low-Carbon Fuels

Mengwei Yu

Supervisor: Prof. Xi Jiang

School of Engineering and Materials Science
Queen Mary University of London

This dissertation is submitted for the degree of
Doctor of Philosophy

March 2023

Statement of originality

I, Mengwei Yu, confirm that the research included within this thesis is my own work or that where it has been carried out in collaboration with, or supported by others, that this is duly acknowledged below and my contribution indicated. Previously published material is also acknowledged below.

I attest that I have exercised reasonable care to ensure that the work is original, and does not to the best of my knowledge break any UK law, infringe any third party's copyright or other Intellectual Property Right, or contain any confidential material.

I accept that the College has the right to use plagiarism detection software to check the electronic version of the thesis.

I confirm that this thesis has not been previously submitted for the award of a degree by this or any other university.

Signature:

Date: March 2023

Details of collaboration and publications:

Mengwei Yu, Cheng Chen, and Xi Jiang. Understanding the miscibility of polyoxymethylene dimethyl ethers (OMEn) and diesel blend using molecular dynamics simulation. *Fuel* 2022; 323: 124348. https://doi.org/10.1016/j.fuel.2022.124348.

Mengwei Yu, Cheng Chen, Zhihao Xing, Xi Jiang. ReaxFF molecular dynamics simulation of nickel catalysed gasification of cellulose in supercritical water. *International Journal of Hydrogen Energy* 2023; 48(1): 123-137. https://doi.org/10.1016/j.ijhydene.2022.09.202.

Mengwei Yu, Xin Yu, Dunxi Yu, Xi Jiang. Molecular dynamics investigation of the effect of ammonia on coal pyrolysis and the nitrogen transformation. *Energy Conversion and Management* 2023 (under review).

Zhihao Xing, **Mengwei Yu**, Cheng Chen, Xi Jiang. A molecular investigation on the effects of OME_x addition on soot inception of diesel pyrolysis. *Fuel* 2022. (submitted)

Acknowledgements

First of all, I would like to express the sincere gratitude to my supervisor Prof. Xi Jiang for his constant guidance and encouragement throughout my PhD study. Prof. Jiang continuously provided encouragement and was always willing and enthusiastic to assist in any way he could throughout the research project. The instructive advice and insightful discussion during my research have greatly inspired me in my academic pursuit.

I would like to express my deepest appreciation to my country. I could not have undertaken this journey without funding from the China Scholarship Council (CSC). Best wishes to my country. Thanks should also go to the institutes and faculties who have provided the supercomputing services, including the UK national supercomputing service of Archer and QMUL Apocrita.

Also, I would like to thank all my friends, Dr. Xuanze He, Dr. Cheng Chen and Dr. Guoxiang Zhao, Zhihao Xing et al., for their help and encouragement.

Lastly, I would be remiss in not mentioning my family, especially my parents, sister, and wife. Their belief in me has kept my spirits and motivation high during this process.

Abstract

Producing and utilising low-carbon fuels are essential to achieving net-zero carbon emission and meeting the requirement of the 2 °C scenario. Molecular dynamics simulation can provide an in-depth understanding of the chemical mechanism of fuel production and physiochemical properties of low-carbon fuels, which can be used to guide the production and utilisation of sustainable low-carbon fuels. This study is focused on investigating biomass catalytic gasification for fuel production and two important low-carbon fuels, i.e., polyoxymethylene dimethyl ethers (OME_n) and ammonia. It considers the mechanisms of nickel catalysed gasification of cellulose in supercritical water and key physiochemical properties of OME_n/diesel and coal-ammonia mixtures.

Reactive force field molecular dynamic simulation was performed to elucidate the mechanism of Ni-catalysed supercritical water gasification of cellulose. Simulations showed that Ni could decrease the activation energy of C-C and C-O bond cleavage, promoting the depolymerisation and ring-opening process of cellulose. The yields of gaseous products increase with the increasing temperature. H_2 yield mainly depends on H free radical number, which can be generated from cellulose dehydrogenation and water-splitting reactions. In the presence of Ni catalyst, water plays a limited role in providing H free radicals to produce H_2, while the hydrogen atoms in cellulose are the primary source of H_2 generation.

Co-firing ammonia, a carbon-free fuel, has been identified as a promising option to reduce CO_2 emissions from coal-fired power plants. The effect of ammonia on coal pyrolysis and nitrogen transformation was studied by ReaxFF simulation. The results show that ammonia decomposition products, $NH_2^\bullet$, will combine with coal decomposition fragments, preventing char formation. The active site on coal fragments would increase at high temperatures owing to the dehydrogenation reaction of coal, which makes more $NH_2^\bullet$ interact with carbon in coal, thus increasing the nitrogen content in char. In addition, the transformation and evolution of nitrogen atoms on coal fragments were investigated.

Polyoxymethylene dimethyl ethers as an alternative fuel have attracted considerable interest in recent years owing to their much-reduced environmental impact. Since OME_n is often blended with diesel, the miscibility and stability of OME_n/diesel mixtures are essential for engine operation. In this study, the molecular dynamics method was used to investigate the miscibility of $OME_{1\text{-}6}$ and diesel blends. The results suggest that the

miscibility of OME_n and diesel blends decreases with the increasing number of oxymethylene units. The aromatics and heteroatomic molecules help maintain the stability of OME_n/diesel blends. The intermolecular interactions between OME_{1-6} and diesel molecules were investigated, which revealed that the electrostatic interaction plays a significant role in the liquid-liquid equilibrium of OME_n/diesel blends.

Table of contents

List of figures

List of tables

Nomenclature

Greek Symbols

ε	Energy; Depth of the LJ potential well
λ	Scaling factor for the velocity of atoms
σ	Time scale; The distance at which the LJ potential energy is zero
τ	Instantaneous temperature
ξ	Friction parameter of heat reservoir
χ	Scaling factor for the volume of MD box
θ	Bond angle
ϕ	Dihedral angle
ρ	Density
ε_0	Permittivity of vacuum
χ_{demix}	Demixing index

Roman Symbols

$\boldsymbol{a}$	Acceleration
A	Pre-exponential factor
E	Energy
Ea	Activation energy
$\boldsymbol{F}$	Force placed on atom
$g^{md}(r)$	The minimum-distance distribution function
k_B	Boltzmann constant

k_T	Isothermal compressibility.
L	Length of MD box
m	Mass of atom
M	Molecular mass
N	Number of atoms
N_f	Freedom degrees of the MD system
P	Pressure
p	Instantaneous pressure
p_{bo}	Empirical parameters in the ReaxFF force field
q	Partial charges on atom
Q_l	Steinhardt's bond orientational order parameters
Q_T	Effect mass of the reservoir
r	Distance between atoms; Bond length
$\boldsymbol{r}$	Position of atom
R	Universal gas constant
R^2	Coefficient of determination
T	Temperature
t	Time
U	Potential energy
v	Velocity
V	Volume of MD box

Subscripts

0	Initial state
a	Two-bond angle
b	Bond stretching interaction
d	Dihedral angle
eq	Equilibrium state
nb	Non-bonded interactions

Abbreviations

ANT	Anthracene
CAR	Carbazole
DBT	Dibenzothiophene
DCP	*n*-Decylcyclopentane
DEC	*n*-Decane
DHN	Decahydronaphthalene
DME	Dimethyl ether
DMO	2,4-Dimethyloctane
EIC	Eicosane
MET	2-Methyltetradecane
MTBE	Methyl tert-butyl ether
NAP	Naphthalene
NCH	*n*-Nonylcyclohexane
OME_n	Polyoxymethylene dimethyl ethers
PEN	*n*-Pentadecane
AMBER	Assisted Model Building with Energy Refinement
C/W	Cellulose-to-water mass ratio
C_{end}	C atom located at the end of the carbon chain
CHARMM	Chemistry at Harvard Macromolecular Mechanics
Char-N	Nitrogen atoms maintained in char
Cmiddle	C atom that located in the middle of the carbon chain
COP27	The United Nations Climate Change Conference of the Parties
C_{ring}	C atom located in the aromatic ring
GHG	Greenhouse gas emissions
LAMMPS	Large-scale Atomic/Molecular Massively Parallel Simulation
LCFs	Low-carbon fuels
LJ	Lennard-Jones function
MD	Molecular dynamics simulation

N5	Pyrrolic nitrogen
N6	Pyridinic nitrogen
NiNP	Ni nanoparticle
NPT	Isothermal-isobaric ensemble
N-Q	Quaternary nitrogen
NVE	Microcanonical ensemble
NVT	Canonical ensemble
OPLS	Optimised Potentials for Liquid Simulations
OPLS-AA	Optimised potentials for liquid simulations all-atom force field
PBC	Periodic boundary conditions
PM	Particulate matter
QEq	Charge equilibration method
QM	Quantum mechanical method
ReaxFF	Reactive force field
SCW	Supercritical water
SCWG	Supercritical water gasification
TraPPE	Transferable Potentials for Phase Equilibria
vdW	Van der Waals interactions
VMD	Visual molecular dynamics

Chapter 1

Introduction

The importance of low carbon fuel production and utilisation as renewable energy in reducing greenhouse gas emissions (GHG) is introduced in this Chapter. The different production methods and applications of hydrogen and ammonia are emphasised. The definition and utilisation of typical oxygenated fuel additives are introduced. The literature review of catalytic supercritical water gasification (SCWG) of cellulose, the coal and ammonia co-firing, and the utilisation of polyoxymethylene dimethyl ethers (OME_n) and diesel blend are presented.

1.1 Low-carbon fuels

The reduction of GHG is an urgent issue worldwide. Scientists announced that global carbon dioxide emissions (CO_2) from fossil fuels are projected to increase by 1% in 2022, hitting a new record of 37.5 billion tonnes at the United Nations Climate Change Conference (COP27). If the current trend continues, humans may pump enough CO_2 into the atmosphere to raise pre-industrial temperatures by 1.5 °C in just nine years [1]. In 2020, traditional fossil fuels made up a significant portion of the global energy supply, as shown in Fig. 1.1(a) [2]. These fuels continue to play a significant role in transportation and power generation. The utilisation of fossil fuels remains the primary source of CO_2 emissions, as depicted in Fig. 1.1(b) [3], which presents the CO_2 emissions from various fuels and industries over the past twenty years. Replacing fossil fuels with low-carbon fuels (LCFs) is a common strategy for reducing GHG emissions from energy use. LCFs represent these fuels that would release less or no carbon during their utilisation process, such as biofuels, natural gas, hydrogen, ammonia, etc.

Hydrogen and ammonia are considered to be key LCFs that could play a crucial role in achieving a net zero society due to their lack of carbon emissions at the point of use. Both of these fuels are highly versatile, capable of being generated and utilised in a variety of ways, including through the use of renewable energy sources. They can be used to decarbonise sectors such as heavy transport, industry, and heat, as well as for energy storage and transportation. These fuels are already widely utilised in industry and agriculture, but their current production methods result in a significant greenhouse gas footprint. In addition to the use of hydrogen and ammonia, the mixing of oxygenated fuel additives (such as ethanol, methanol, biodiesel, and ethers) with gasoline or diesel is also a promising approach for reducing carbon emissions. The requirements and benefits of utilising oxygenated fuel additives are discussed in Section 1.1.3.

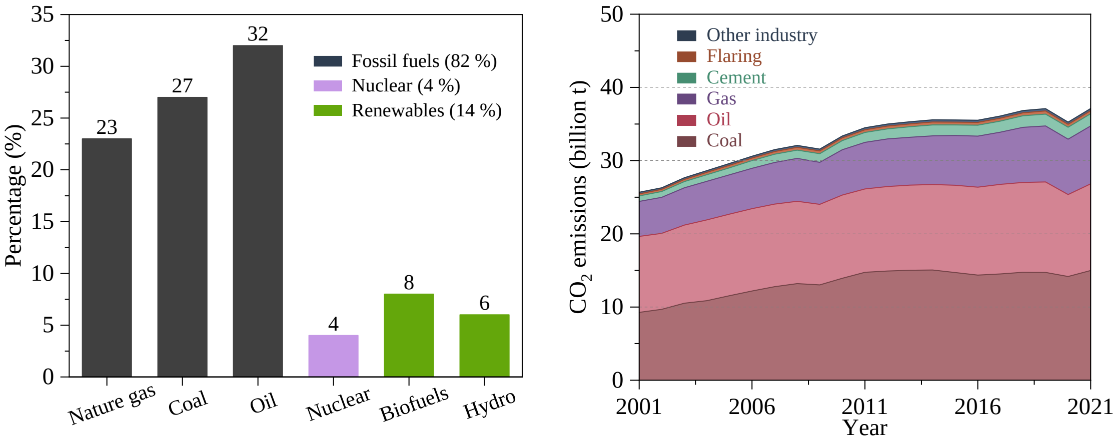

(a) (b)

Fig. 1.1 (a) Share of global energy supply in 2020 [4]; (b) CO_2 emissions by different types of fuel or industries worldwide [3].

1.1.1 Hydrogen production and utilisation

Hydrogen can be produced from diverse domestic resources with the potential for near-zero greenhouse gas emissions. The combustion of hydrogen only emits water vapour. It holds promise for growth in both the stationery and transportation energy sectors. More specifically, the advantages of hydrogen fuel can be summarised as [4]:

- Hydrogen can be produced using diverse energy resources.
- The production methods of hydrogen are multifarious.
- Unlike other carbon-based fuels, the usage of hydrogen does not emit CO_2 emissions.
- Hydrogen can play a crucial role in the decarbonisation of the maritime industry by using off-grid offshore wind energy to produce clean fuel for the maritime industry.
- Hydrogen is an ideal energy carrier that can be employed as a medium for energy

storage.

Fig. 1.2 presents the different types of hydrogen production methods and utilisation. Hydrogen can be generated by electrochemical, biological, and thermochemical methods. Depending on the raw materials and production route, hydrogen can be classified as grey, blue, and green: (i) grey hydrogen is obtained via the reforming of fossil fuels; (ii) blue hydrogen represents that the carbon emissions are captured, stored, or used during the hydrogen production process; and (iii) green hydrogen refers to the use of a renewable feedstock and a renewable source of energy for the conversion of raw materials and the operation of the processing facility [5]. Over 95% of the global hydrogen is derived from the reforming of fossil fuels, and about half of that amount comes from steam reforming of natural or shale gas [6].

One of the obstacles to the usage of hydrogen is its high production cost. The cost of producing hydrogen varies depending on the method used to produce it. The price can vary depending on a number of factors, including the availability of raw materials and the cost of electricity. In general, however, hydrogen production is relatively expensive compared to other energy generation methods [7]. Improving the hydrogen production efficiency and lowering the production cost is one of the challenges of using hydrogen [4].

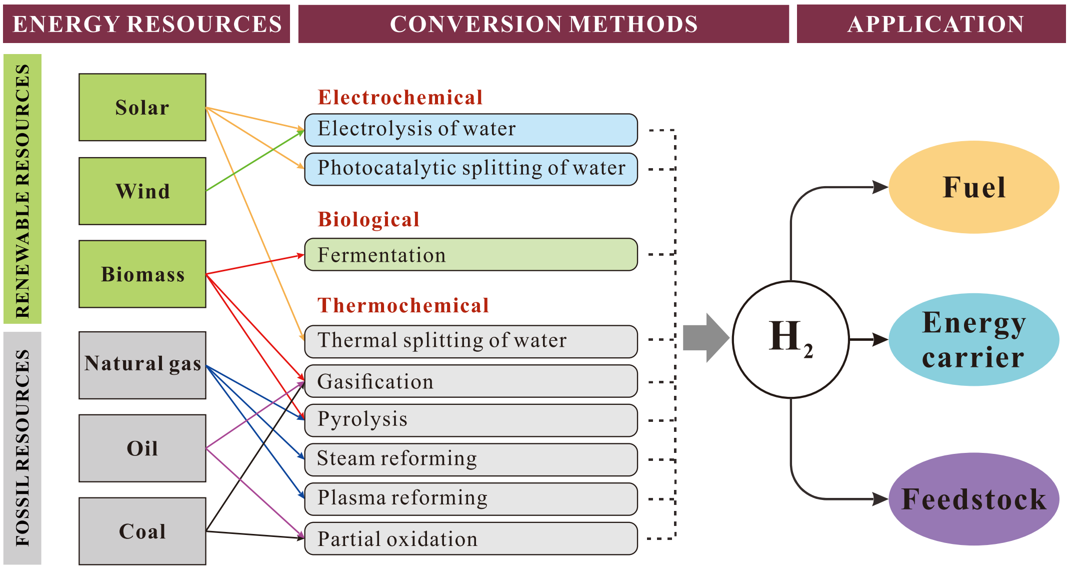

Fig. 1.2 The different types of hydrogen production and utilisation methods [4].

1.1.2 Ammonia production and utilisation

Ammonia is typically produced by the Haber-Bosch process, which involves combining nitrogen from the air with hydrogen gas to produce ammonia [8]. Ammonia is referred to with the same label as the hydrogen from which it was synthesised. Ammonia is labelled as brown if hydrogen is produced by using coal gasification or grey if hydrogen is made using natural gas reforming. Blue ammonia uses the same feedstock as brown and grey ammonia but includes a carbon capture and storage unit. Green ammonia is made entirely from renewable power, water, and air; the hydrogen for its synthesis is generated from electrolyser stacks.

Approximately 175 million tonnes of ammonia are produced annually worldwide, and most of it is used in the production of fertilisers [9]. The existing and expanded end uses of ammonia are shown in Fig. 1.3. Ammonia has been proposed as a potential fuel for use in energy production. There are several advantages of using ammonia as a source of energy compared to hydrogen. First, ammonia is more accessible and less expensive to produce than hydrogen. It can be made from readily available materials, such as nitrogen and hydrogen gas, using relatively simple industrial processes. In contrast, hydrogen must be produced through more complex and energy-intensive processes, such as steam reforming or electrolysis. Another advantage of ammonia is that it has a relatively higher energy density than hydrogen. The volumetric energy density of a range of fuel options is presented in Fig. 1.4 [10]. It can be seen that a given volume of ammonia contains more potential energy than an equal volume of hydrogen. This makes it more practical for use as a fuel, as it requires less space for storage and transportation. Additionally, ammonia is less flammable and safer to handle than hydrogen. It has a much higher ignition temperature, which makes it less likely to ignite accidentally. This makes it a safer fuel for use in vehicles and other applications where there is a risk of fire or explosion. Overall, ammonia has several advantages that make it a potentially attractive alternative.

However, there are also several challenges associated with using ammonia as a fuel. One potential problem with using ammonia as a fuel is the potential for the production of nitrogen oxides (NO_x), which are pollutants that can have harmful effects on human health and the environment [11]. NO_x formation is influenced by several factors, including combustion temperature, pressure, residence time, oxygen concentration, fuel type and composition. The presence of nitrogen in the fuel can contribute to NO_x formation since the high temperatures cause the nitrogen and oxygen atoms in ammonia to combine, forming NO_x. The production of NO_x occurs when ammonia is burned at high temperatures, such as in an engine or a fuel cell. These nitrogen oxides can then be released into the atmosphere, where they can contribute to air pollution and have harmful effects on human health and the environment. To address this problem, it may be necessary to develop technologies and processes that can reduce or eliminate the production of NO_x when using ammonia as a fuel. This could include using catalysts or other methods to lower the combustion temperature of ammonia, or the development of engines or fuel cells specifically designed to minimise the production of NO_x. Overall, the potential for the production of NO_x is a challenge that must be addressed in order to make the use of ammonia as fuel more practical and feasible. Further research and development are needed to find solutions to this problem and minimise the production of NO_x when using ammonia as a fuel.

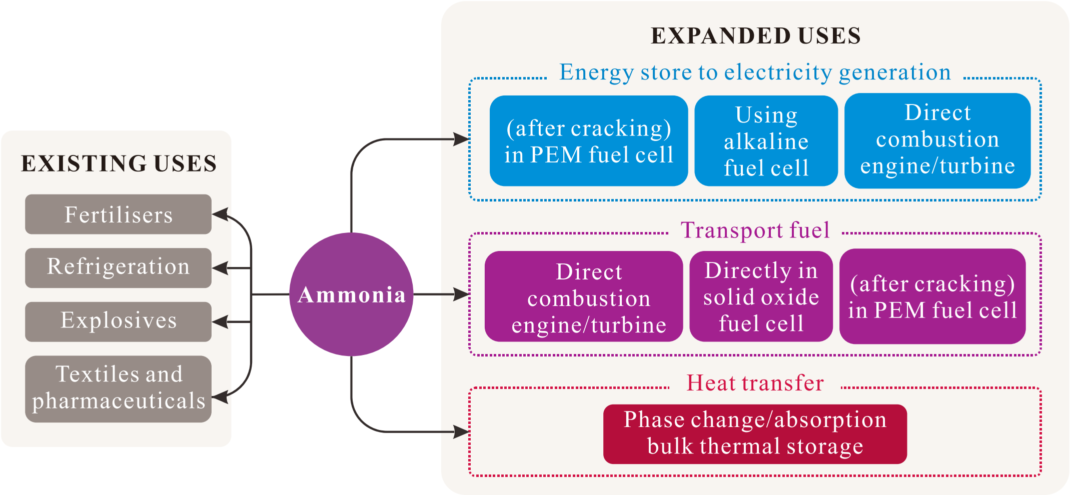

Fig. 1.3 Schematic of existing and expanded end uses of ammonia [10].

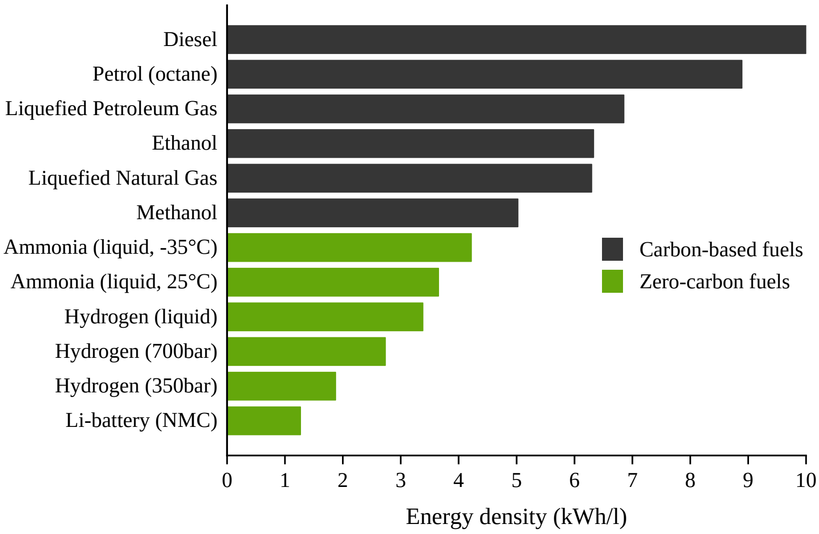

Fig. 1.4 The volumetric energy density of a range of fuel options [10].

1.1.3 Oxygenated fuel additive utilisation

Oxygenated additives are chemicals that are added to fuels such as gasoline or diesel in order to increase the oxygen content of the fuel. This can improve the combustion of the fuel and make it more efficient, which can lead to reduced emissions and improved fuel economy. Examples of oxygenated additives include ethanol, methanol, methyl tert-butyl ether (MTBE), dimethyl ether (DME), and OME_n. Good oxygenated fuel additives should have a few fundamental properties [12]:

- Solubility: The oxygenate should be soluble in the fuel in order to mix evenly and provide the desired effects.
- Volatility: The oxygenate should have a suitable vapour pressure to evaporate and mix with the air in the fuel-air mixture.
- Octane rating: The oxygenate should have a high-octane rating, which is a measure of a fuel's ability to resist knocking or pinging during combustion.

- Cetane number: The oxygenate should have the ability to effectively increase the cetane number of diesel fuel.
- Viscosity: The additive should not have a significant impact on the viscosity of the fuel.
- Lubricity: The additive should not decrease the lubricity of the fuel.
- Energy content: The oxygenate should have a high energy content to provide adequate energy when burned.
- Compatibility: The oxygenate should be compatible with the fuel and other additives so that it does not cause any adverse effects on the fuel system or the engine.

The oxygenated fuel additive is considered an LCFs since using oxygenated additives in fuels such as gasoline or diesel can help reduce carbon emissions. When oxygenated additives are added to fuel, they increase the oxygen content of the fuel, which can improve the combustion of the fuel and make it more efficient. This can result in the release of fewer carbon emissions when the fuel is burned. Additionally, some oxygenated additives are themselves made from renewable materials such as corn or other plant materials, which can further reduce carbon emissions. For example, ethanol is often made from corn or other crops, and the carbon dioxide released during ethanol production is typically offset by the carbon dioxide absorbed by the crops as they grow. This can result in a net reduction in carbon emissions compared to gasoline or diesel made from fossil fuels.

1.2 Hydrogen production - Supercritical water gasification of cellulose

Biomass is an effective energy carrier, contributing to the growing demand for clean and everlasting energy sources for the sustainable development of society. Biomass can be converted to biofuel through biochemical technologies (e.g., fermentation and anaerobic digestion) and thermochemical technologies (e.g., pyrolysis, liquefaction, gasification and torrefaction) [13]. One of the leading technical barriers to industrialising biomass-derived energy is the high energy input of conversion processes, especially for biomass with high moisture content. Wet bio-feedstocks require energy-costly drying operation, reducing the efficiency of the energy conversion process. However, SCWG technology may overcome this problem as the wet biomass can be directly gasified without an energy-intensive drying step, thereby reducing the processing cost. SCWG of wet biomass can produce H_2-rich syngas, which has a high heating value and can be used as a cleaner alternative of fossil fuels.

Biomass gasification is a process that converts feedstock materials into gaseous products such as syngas at high temperature conditions (above 700°C), with a controlled amount of oxygen and/or steam. One of the primary benefits of SCWG technology is associated with the high-pressure/high-temperature water that is used as the reaction medium. The physical properties of water drastically change when the pressure/temperature conditions are above its critical point. As the reaction medium, supercritical water (SCW) offers several advantages, such as low viscosity, high diffusion coefficient, and complete miscibility with varying organics and gases, thereby enhancing the mass transfer and reaction rate in the reactor [13].

Cellulose is one of the main structural components of lignocellulose biomass, constituting 40~50 wt% of lignocellulosic biomass on a dry weight basis [14]. Moreover, it is reported that the contribution of cellulose to H_2 production during the gasification process is more than that of hemicellulose and lignin [15]. Therefore, it is essential to investigate the conversion mechanism of cellulose during the SCWG process. Extensive experimental studies on SCWG of cellulose have been carried out [13, 16, 17]. Cellulose comprises glucose monomers linked together by β-1,4 D-glucopyranose bonds, forming strong intramolecular and intermolecular hydrogen bonds [16]. Cellulose undergoes rapid hydrolysis and decomposes to its monomer (e.g., glucose) at very short residence times under elevated pressure/temperature. Then glucose undergoes hydrolysis to liquid-phase organic intermediates, followed by the slower formation of small quantities of stable light gases [18]. Therefore, cellulose is one of the most refractory substances that are difficult to dissolve in hot water [19], requiring harsh operating conditions to convert it into biofuel. It is widely accepted that a higher operating temperature favours the formation of H_2 [13, 15]. However, heating the feedstock and water to supercritical conditions is an energy-consuming process. Lowering the reaction temperature of SCWG and improving the conversion efficiency are essential for promoting the commercial utilisation of SCWG.

The use of catalysts in SCWG is one of the most promising approaches to improve the gas yield while minimising the heat requirements, which can reduce the operating costs of the process [20]. Nickel-based catalyst is one of the most effective transition metal catalysts in biomass gasification for improving the gas yield and preventing the formation of tar (heavy hydrocarbons produced during SCWG, which can contaminate equipment and lead to increased maintenance costs) [21]. Extensive studies have been carried out to investigate the catalytic effect of nickel (Ni) on the gaseous product yield in the biomass SCWG process [20, 21]. It is widely accepted that Ni could effectively promote water gas shift reaction and steam reforming reaction [22, 23], which are the two main reactions occurred in SCWG to produce hydrogen. Ni is known for its tendency to catalyse the cleavage of C-C, C-O, and O-H bonds [24, 25], which promotes the formation of various carbonaceous products. The cracking products can be effectively dehydrogenated to produce more hydrogen [26]. Ruppert et al. [25] studied the thermochemical conversion of cellulose for hydrogen production with Ni/ZrO_2. They considered that the organic intermediates probably undergo dehydrogenation on the metal surface, hence increasing H_2 yield. The cleavage of C-C and C-O bonds can occur to form various carbonaceous products. However, the proposed mechanisms were primarily based on the analysis of products detected during the SCWG process. Detailed structural changes at the molecular level, such as radicals and intermediates in cellulose dissociation and steam reaction, can hardly be captured through experimental methods. The exact mechanism of Ni catalytic thermal decomposition of cellulose has not been fully understood and further investigation is needed

Due to the limitation of experimental methods, molecular dynamics (MD) simulations were adopted to study the underlying mechanisms the SCWG of biomass from atomic level (The detailed introduction of MD is presented in Chapter 2). The structural evolution of lignin and the chemical reactions of forming CO, CO_2, CH_4, and H_2 during SCWG were obtained by using MD simulations [27-29]. Zhang et al. [30] conducted a molecular study on SCWG of glucose under microwave heating. They found that the external electric fields promote glucose decomposition to produce formaldehyde and hydrogen-free radicals, increasing H_2 yield. Monti et al. [31] obtained an atomic-level characterisation of the crucial steps of the adsorption of the lignin molecules on the Palladium catalyst by using MD simulations. The SCWG of lignin with Pt and Ni nanoparticles was studied by using MD simulations [32]. It was found that the Pt and Ni reduce the degradation temperature, accelerating the aromatic ring-opening process. The MD simulation study of Fe-catalysed SCWG of lignin revealed that Fe iron with a low oxidation state contributes to the formation of CO, while iron with a high oxidation state was beneficial to increasing CO_2 yield [33]. The evolution of the lignin decomposition catalysed by Ni was investigated [34]. The results indicated that Ni could potentially accelerate the scission of C-O bonds and destroy the conjugated π bond of the aromatic ring during the ring-opening process. The generation process of H_2 molecules occurring on the Ni surface was presented. The thermal stability of carboxymethyl cellulose on the Fe_2O_3 surface was studied by Saha et al. [35]. It was found that cellulose can be adsorbed on the metal surface via the formation of bonds between Fe and oxygen atoms. The chemisorption would bulge the Fe slightly out of the Fe_2O_3 surface. The review of investigation of biomass SCWG by using MD simulation is listed in Table 1.1.

Table 1.1 The review of the investigation of biomass SCWG by using MD simulation

Feedstocks	Catalysts	Temperature (K)	Simulation duration (ns)	Forcefields	Main conclusions	Ref.
Lignin	Ni	1600	1.5	CHONNi 2010 [36]	• Smaller catalyst cluster possesses higher activity.	[34]
Lignin	Pt/Ni	1700	1.5		• The synergy of Pt and SCWG shows more excellent properties.	[32]
Lignin	Fe/FeO /Fe_3O_4 /Fe_2O_3	2100	1.6	CHOFe 2015 [37]	• Iron with a low oxidation state was beneficial to the formation of CO, while iron with a high oxidation state was CO_2. • SCW participates in the entire reaction, providing both H and O free radicals.	[33]
Lignin	-	2200~2800	3.0	CHON 2012 [38]	• The yields of CO_2, H_2, CH_4, and the corresponding H_2 proportions in the products increase with the temperature.	[27]
Lignin	-	1400~3600	1.0	CHON 2008 [39]	• The conversion of C5-C10 and other C1-C4 products to H_2 and CO is promoted by the H_2O molecules.	[40]
Lignin	-	1000~5000	1.0	CHON 2008 [39]	• Above 2500 K, H_2, CO and CO_2 are predominantly formed in which water molecules contribute hydrogen and oxygen for their formation.	[29]
Lignin + Plastics	-	2000~5000	2.0	CHON 2008 [39]	• Lignin cracks slowly but completely at low temperatures (2000K), whereas most PE remains intact.	[41]
Cellulose + polyethylene	-	600~1800	0.1	Not specified	• The co-gasification process accelerates the cleavage of long-chain char and improves the conversion of CE/PE into oil and gas. • The yield of oxygen-containing tar declines with increasing PE:CE mass ratio. • The light hydrocarbon groups released from PE assist	[42]

Feedstocks	Catalysts	Temperature (K)	Simulation duration (ns)	Forcefields	Main conclusions	Ref.
					in the decomposition of oxygen-containing components in CE to generate small molecule gases.	
Cellulose/ Lignin	-	1250~2000	6.0	CHON 2001 [43]	• The breakdown of cellulose and oxygenation of the products are enhanced in the presence of water, while lignin remains largely unaffected by water. • As temperature increases, the water's oxygenating effects in the cellulose are decreased.	[44]
Glucose	-	1000~6000	0.35	CHON 2001 [43]	• The external microwave can increase the production of hydrogen gas by promoting the yields of glucose decomposed into formaldehyde and hydrogen free radicals.	[30]
Furfural	-	600~1800	0.5	Not specified	• Supercritical water molecule clusters provide H and OH free radicals to enhance significantly H_2 and CO production.	[45]

1.3 Ammonia utilisation - Coal and ammonia co-firing

Coal still plays a significant role in power generation especially in developing countries, and coal-fired power plants are considered as one of the primary sources of CO_2 emissions. It was reported that emissions from coal burning would increase by around 1% and could set a new record [1]. Replacing coal with low-carbon fuels is of great significance for reducing CO_2 emissions and achieving carbon neutrality globally.

Ammonia (NH_3) is expected to be a potential fuel to substitute coal and fossil fuels because it does not release CO_2 and is easily handled by liquefaction. Co-firing of coal and NH_3 is a promising method that enables retrofitting of coal-fired power plants without major modifications while contributing to global decarbonisation goals. It is widely accepted that co-firing of coal with NH_3 allows for lower CO_2 emissions as compared to coal-only combustion [46]. However, it is concerned that the concentration of NO_x in the flue gas could increase due to the oxidation of ammonia. It is important to study the generation mechanism of NO_x for the development of coal/NH_3 co-firing technology, so that the operation of power plants can be optimised for minimal CO_2 and NO_x emissions.

The energy utilisation process in power plants is complex due to the intricacy of fuel combustion. A number of experimental and numerical studies have been done to explore the transformation behaviour of atomic nitrogen (N) during coal/NH_3 co-firing. These investigations mainly focused on the impact of NH_3 ratio, boiler temperature, and NH_3 injection methods on the final NO_x emissions [47-53]. The energy utilisation process can be divided into fuel pyrolysis and late combustion stages [54]. During pyrolysis stage, NH_3 could dissociate into amino radical ($NH_2^\bullet$) and imidogen radical ($NH^{2\bullet}$) via reactions $NH_3 \leftrightarrow NH_2^\bullet + H^\bullet$ and $NH_3 \leftrightarrow NH^{2\bullet} + H_2$ [55, 56]. $NH_2^\bullet$ and $NH^{2\bullet}$ would react with coal decomposition fragments, which enables nitrogen atoms carried by these radicals to be migrated into solid substances to form char-N (nitrogen atoms that are maintained in the char). The formation of char-N during pyrolysis is a crucial factor that affects NO_x formation in the subsequent combustion process. It was reported that around 60%~95% of the total NO_x emission is driven by char-N combustion [57]. The typical structures of char-N during coal-only pyrolysis are pyrrolic nitrogen (N5), pyridinic nitrogen (N6), and quaternary nitrogen (N-Q) [57, 58]. During the combustion of chars, each nitrogen functionality (N-functionality) contributes its own characteristic rate to NO emission. Stańczyk [57] found that the combustion of N5 and N6 is responsible for NO emissions, while the N-Q can hardly be oxidised to form NO_x. Deng et al. [59] investigated the NO_x emissions during the combustion of different types of coals. They found that compared with N6, combustion of N5 will lead to less NO emission at low oxygen concentrations but more NO emission at high oxygen concentrations. However, the conversion mechanism of ammonia nitrogen to char-N during coal/NH_3 co-pyrolysis is still unclear. The morphological evolution of N-functionalities that existed in char also requires further investigation. A deeper understanding of the N transfer mechanism during coal/NH_3 co-pyrolysis is essential to minimising NO_x emissions for coal/NH_3 co-firing technology.

Presently, it is challenging to investigate the reaction pathways of N transformation by experiments due to the uncertainty of experimental conditions and the complexity of the gaseous environment around the coal char during co-pyrolysis. MD simulation was also used to investigate the underlying mechanisms of nitrogen transformation during coal/NH_3 co-pyrolysis at an atomic level. MD has been used to study the impact of NH_3 on coal combustion and soot formation. For example, Hong et al. [60] investigated the coal/NH_3 co-firing in the boiler by using MD. They found that NH_3 will compete with coal char for O_2, resulting in an increase in the NH_3 oxidation rate and a decrease in the char oxidation rate. Temperature, fuel-to-oxidiser ratio, and NH_3 injection ratio will affect the competition between char-O_2 and NH_3-O_2 reactions. Zhang et al. [61] studied the inhibitory mechanisms of NH_3 addition on the formation and growth of polycyclic aromatic hydrocarbons (PAHs) and soot. Zheng and Li [62] studied the N transformation during coal char oxidation by MD simulation. The results show that the condition of high oxidation temperature is a good choice for NO conversion to N_2 in char combustion. The N transfer mechanism in the hydropyrolysis process of coal was studied by Wang et al. [63]. The results showed that active hydrogen atoms provided by hydrogen molecules could promote inactive tertiary amine and heterocyclic moiety decomposition in the solid phase.

1.4 Oxygenated fuel additive utilisation - OME_n and diesel blend

There are difficult-to-decarbonise industries such as sea and air transport. Diesel fuels have been broadly used in large marine engines due to their superior energy density and stability. However, the particulate matter (PM) emissions generated by diesel combustion have been causing a serious impact on human health and the environment [64]. The emission reduction requirements for fossil fuel combustion are becoming increasingly more stringent in order to reduce pollutants to protect the environment [65]. Cleaner combustion technologies especially fuels with minimal environmental impact and more effective combustion and emission control strategies should be developed to satisfy the stringent emission regulations.

Alternative fuels are thought to be effective in providing sustainable/renewable energy sources for engines to achieve high efficiency and clean combustion [66]. In recent years, the most frequently investigated alternative liquid fuels are alcohol, biodiesel, and DME [67-72]. Polyoxymethylene dimethyl ethers (abbreviated as $PODE_n$, DMM_n, or OME_n) as an oxygenated fuel additive have attracted considerable interest recently [73-76]. The general chemical structure of OME_n is CH_3-O-(CH_2-O)$_n$-CH_3, where n is the number of oxymethylene units. The main properties of $OME_{1\text{-}5}$ and diesel are listed in Table 1.2. A number of studies have shown that the addition of OME_n to diesel fuel could effectively reduce PM and GHG emissions due to its high oxygen content and absence of carbon-carbon bonds in the molecular structure [77-79]. The high cetane number of OME_n could also improve the anti-knock performance of the fuel [80]. Furthermore, OME_n is a sustainable and eco-friendly fuel which can be produced from biomass including waste biomass via syngas [81] and even from CO_2 [82].

Table 1.2 The main properties of OME_{1-5} and diesel [80].

	OME_1	OME_2	OME_3	OME_4	OME_5	Diesel (EN 590)
Oxygen content (wt%)	42.1	45.2	47.0	48.1	48.9	-
Density at 20 °C (g/cm^3)	0.86	0.98	1.03	1.07	1.11	0.820~0.840
Melting point (°C)	-105	-70	-43	-10	18	-20~0
Boiling point (°C)	42	105	156	202	242	170~390
Autoignition point EN 14522 (°C)	237	-	235	235	240	220
Flash point EN ISO 2719 (°C)	-32	-	54	88	115	>55
Cetane number	50	-	124	148	180	>51
Lubricity at 60 °C ISO 12156-1 (μm)	759	-	534	465	437	<460
Kinematic viscosity at 25 °C (mm^2/s)	0.36	-	1.08	1.72	2.63	2.0~4.5

Since blended fuels are often intended to be directly used in existing engines, the miscibility of different chemical substances in the mixture should be guaranteed when evaluating if an alternative fuel can be used in practical engines. The fuel mixture formation has significant effects on the spray and combustion characteristics [70]. The inhomogeneity of fuel blend caused by poor miscibility will affect the fuel/air mixing, combustion and pollutant emissions, which can also offset the effect of the oxygenation of OME_n on reducing PM emissions. The unwanted phase separation of the fuel blends would affect the combustion stability, causing damage to the engine and making noise. Cylinder pressure, heat release, emissions, and fuel economy of OME_n/diesel blend were tested by Liu et al. [83]. The OME_n adopted in their work is a mixture of 2.6% OME_2, 88.9% OME_3, and 8.5% OME_4. There was no solubility issue when OME_n was blended with diesel at room temperature. The miscibility of OME_n with diesel was also studied by Han et al. [84]. The OME_n contains 20% OME_1, 24% OME_2, 25% OME_3, 17% OME_4 and 14% OME_{5-8}. They found that a mixture of OME_{3-8} and diesel had good solubility and stability. Jin et al. [85] investigated the phase behaviour of OME_n and diesel mixture. The OME_n is composed of OME_3, OME_4, OME_5, and OME_6 with mass fractions of 45%, 28%, 17%, and 10%, respectively. It was found that the OME_n can be blended with diesel fuel without phase separation when the ambient temperature is higher than 10 °C. The blends have a relatively poor solubility at temperatures below 10 °C. Moreover, OME_n has been used as a co-solvent for the blends of alcohol/diesel [85] and alcohol/soybean oil [86]. The experimental results showed that the OME_n has the ability to maintain the stability of the alcohol/diesel blend.

Although there are several experiments reported that the OME_n can be blended with diesel without causing major issues, it is believed that the number of oxymethylene units affects the miscibility. In addition, low-temperature performance can be a concern. Li et al. [87] investigated the solubility of OME_n/diesel blend, and the results showed that the cloud points of OME_{3-8}/diesel blend and OME_{3-5}/diesel blend are 7 °C and -11 °C, respectively. Omari et al. [88] also reported that blends of 35 vol% OME_n in diesel exhibit increasing cloud point temperatures with rising OME_n chain length. In addition, the OME_n adopted in the aforementioned experiments is a mixture of OME_{1-8}. Fundamental and comprehensive studies on the pure components of OME_n and diesel blends have been rarely carried out. Yang et. al [89] investigated the solubility of pure OME_{1-8} in six diesel hydrocarbons and three surrogate diesel fuels at different temperatures by using simulation software to predict the thermo-physical data of chemical compounds. They found that the solubility of pure OME_{1-8} in the diesel hydrocarbons and the surrogate diesel fuels decrease with the increasing number of oxymethylene units. It was also observed that the solubility of OME_n and diesel mixtures become worse when switching from fossil to paraffin diesel [88]. However, the mechanisms behind the change of solubility are largely unknown, while the understanding on this can help optimise fuel blend compositions. Presently, the intermolecular interaction between OME_n and diesel molecules, including the types of paraffins and aromatics, have not been fully understood and further investigation is needed.

In addition to experiments, MD was applied to study the miscibility of the binary or ternary system [90-92]. Oliveira and Caires [93] investigated the molecular arrangement of the diesel/biodiesel blend by MD simulations. In another study, Oliveira et al. [94] adopted MD to study the effect of biodiesel as a co-solvent on the miscibility of diesel/ethanol blend. Pozar et al. [95] investigated the phase behaviour of ethanol and alkanes, and they evaluated the different statistical methods to describe the morphological changes in the mixtures.

1.5 Knowledge gaps, motivation, and thesis overview

The promotion and industrial applications of LCFs are significant to achieving a net-zero carbon society. However, there are still some challenges in producing and utilising LCFs. This study aims to solve some obstacles placed in utilising LCFs, such as lowering the production costs of LCFs and minimising the environmental impacts caused by using LCFs.

The gasification of biomass is one of the primary methods that produce hydrogen. Although significant experimental work has been performed on Ni catalytic SCWG of biomass, there is a lack of detailed understanding of the chemical processes involved at the molecular level. Further fundamental modelling studies are required to deepen the understanding of the catalytic and micro reaction degradation mechanisms during the SCWG process. This could provide a basis for optimising operating conditions and developing high-efficiency catalysts, thereby promoting the utilisation of SCWG technology.

The NO_x emission is one of the problems that hinder the utilisation of coal and ammonia co-firing technology. Although some experimental studies have been carried out to investigate the NO_x emission during coal and ammonia co-firing, little attention has been paid to the research of the N transfer mechanism during coal/NH_3 co-pyrolysis. Further fundamental modelling studies are required to deepen the understanding of the generation of NO_x precursors and char-N during the pyrolysis stage, which has a significant impact on reducing NO_x emissions.

The phase behaviour is crucial for using OME_n/diesel blend as a fuel, especially at low temperatures. A deeper understanding of the phase behaviour will contribute to the utilisation of blended OME_n and diesel fuels to avoid fuelling problems, to reduce pollutant emissions, and to resolve issues such as cold start of the engine. The fundamental understanding can provide guidance on solving the miscibility problem of OME_n and diesel blends, and on optimizing OME_n and diesel blend compositions in practical applications. The effects of the number of methylene groups and ether groups on the intermolecular and intramolecular interaction are not fully understood.

The objectives of the study are mainly in three aspects:

- To study the catalytic and micro reaction degradation mechanisms during the SCWG process of cellulose. The effects of temperature and cellulose-to-water mass ratio (C/W) on gaseous products will be investigated. Besides, the detailed gaseous product generation pathways and the influence of temperature and C/W on carbon deposition behaviour on Ni nanoparticle (NiNP) will be revealed.
- To investigate the nitrogen transfer mechanism during coal and ammonia co-pyrolysis. The effect of ammonia on coal pyrolysis rate and the reaction between ammonia and coal decomposition fragments will be studied. The detailed morphological evolution of the nitrogen functionalities in char and tar will be discussed.
- To reveal the phase behaviour of OME_n and diesel blends at the molecular level. The impact of oxymethylene unit number on the miscibility of the blends will be investigated. The aggregation and separation behaviour of $OME_{1\text{-}6}$ and different types

of diesel components will be studied. The non-bonded interactions, van der Waals (vdW) and electrostatic interactions, between different molecules will be analysed.

The thesis is organised into several chapters:

Chapter 1: The importance of low carbon fuel production and utilisation as renewable energy in reducing GHG emissions is introduced. The different production methods and applications of hydrogen and ammonia are emphasised. The definition and utilisation of typical oxygenated fuel additives are introduced. The literature review of catalytic SCWG of cellulose, the coal and ammonia co-firing, and the utilisation of OME_n and diesel blend are presented.

Chapter 2: The basics of MD simulations are introduced. The fundamental equations that describe the dynamics of the system and various finite-difference methods for the numerical integration of the equations of motion are discussed. The concept of typical ensembles used in MD and the methods for controlling temperature and pressure are also introduced. In addition, the classical and reactive force fields used in this study are presented.

Chapter 3: Reactive force field molecular dynamic simulation was performed to elucidate the mechanism of Ni-catalysed supercritical water gasification of cellulose considering the effects of temperature and cellulose to water ratio. The depolymerisation and ring-opening process of cellulose, effects of Ni and C/W on gaseous product yield, and carbon deposition behaviour on Ni catalyst are investigated.

Chapter 4: The impact of ammonia on coal pyrolysis and nitrogen transformation during ammonia/coal co-pyrolysis was studied by reactive force field molecular dynamic simulation and supported by validation through a self-designed thermogravimetric (TG) experiment. The ammonia and coal decomposition processes are discussed. The morphological evolution of the nitrogen functionalities in char and tar is investigated.

Chapter 5: The miscibility of OME_n and diesel blends at 300 K and 1 atm was studied using molecular dynamics simulation. Various analyses were conducted to determine the aggregation and separation behaviour of OME_n and diesel molecules. The intermolecular interactions between OME_n and diesel molecules were studied. Minimum-distance distribution functions were used to determine the molecular arrangement of diesel molecules around the OME_n molecules.

Chapter 6: The main conclusions of the thesis are summarised, and suggestions for future work are illustrated.

Chapter 2

Molecular Dynamics Simulations

This chapter provides an introduction to the basics of MD simulations. Using the simple example of the translational motion of a spherical particle, the fundamental equations that describe the dynamics of the system and various finite-difference methods for the numerical integration of the equations of motion are discussed. The concept of typical ensembles used in MD and the methods for controlling temperature and pressure is introduced. In addition, the classical and reactive force field used in this study are discussed.

2.1 Fundamentals

MD simulation is a computational technique used to study the motion and interactions of atoms and molecules over time. It is a powerful tool for understanding the properties and behaviour of pure components and mixtures at the atomic and molecular level, as well as for predicting the response of materials to external stimuli, such as temperature, pressure, and electric and magnetic fields. MD not only yields data for thermophysical properties but also allows gaining an insight into the systems on a molecular level.

Computational methods for studying materials at the atomic and molecular levels are typically organised into a hierarchy, with each level corresponding to a particular time and length scale. Fig. 2.1 presents the hierarchy of computational methods and corresponding time and length scales. The brief description of these computational methods is as follows:

- Quantum chemistry methods: These methods are used to study the electronic structure and properties of small molecules and isolated atoms. They are based on quantum mechanical principles and are accurate at the sub-angstrom length scale (less than 0.1

nanometres). Examples of quantum chemistry methods include density functional theory (DFT).

- MD simulations: These simulations are used to study the motion and interactions of atoms and molecules over time. They are based on classical mechanics and are accurate at the angstrom length scale (0.1~10 nanometres). The time scale of an MD simulation is typically on the order of nanoseconds to microseconds.
- Coarse-grained (CG) simulations: These simulations are used to study the behaviour of large systems, such as proteins and polymers, at a coarse-grained level of detail. They are based on simplified models of the interactions between atoms and molecules and are accurate at the nanometre length scale (10~1000 nanometres). The time scale of a CG simulation is typically on the order of microseconds to milliseconds. CG simulations are typically used to study the structural and dynamic properties of large systems, such as the folding of proteins and the behaviour of polymers.
- Continuum models: These models are used to study the behaviour of materials at the macroscopic level. They are based on the assumption that materials can be treated as a continuous medium, rather than as a collection of discrete atoms and molecules. Continuum models are accurate at the micrometre to millimetre length scale (1000 nanometres to 1 millimetre). The time scale of a continuum model is typically on the order of seconds to hours.

Each level of the hierarchy of computational methods has its own strengths and limitations, and the appropriate method depends on the length and time scales of the phenomena being studied. This study aims to reveal the physicochemical properties of low-carbon fuels during their production and application process. The simulation time reaches 50 ns, and the order of magnitudes of N_{atoms} could be up to 10^4. Therefore, MD method was adopted in this study.

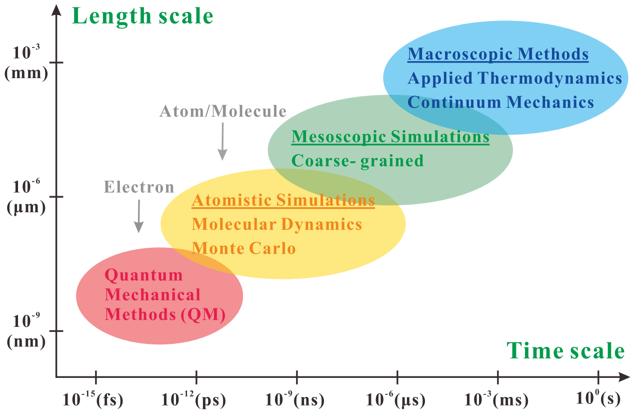

Fig. 2.1 Hierarchy of computational methods and corresponding time and length scales.

2.2 Basic methodology of molecular dynamics

In MD simulation, atoms and molecules are allowed to interact over a predetermined amount of time, revealing the "evolution" of the simulated system. In the most prevalent model, the trajectories of atoms and molecules are determined by numerically solving Newton's equations of motion for a system of interacting particles, where the forces between the particles and their potential energies are calculated using suitable force fields. This approach is primarily utilised in the fields of chemical physics, materials science, and biophysics.

The basic methodology of MD simulation is shown in Fig. 2.2. The first step in an MD simulation is to define the system being studied. This includes identifying the atoms and molecules in the system, as well as their initial positions and velocities. The system may also be defined in terms of boundary conditions, such as the size and shape of the simulation box. The next step is to specify the interactions between the atoms and molecules in the system. The forces between atoms are calculated by a suitable force field. The time evolution of each atom's position is determined by integrating Newton's second law of motion. The final step in an MD simulation is to analyse the results of the simulation. This may involve calculating thermodynamic properties, such as temperature, pressure, and energy, as well as structural properties, such as distances and angles between atoms and molecules.

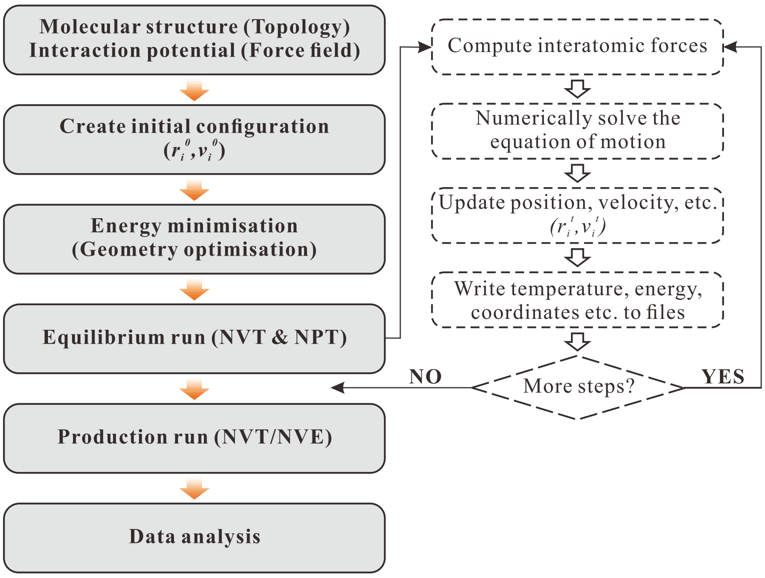

Fig. 2.2 Schematic of the basic molecular dynamics simulation procedure.

2.2.1 The initialisation of MD simulation

Appropriate initialisation in MD simulation is very important since it could avoid instabilities. One method of guaranteeing good initialisation is to ensure that atoms are initialised in equilibrium states. Several parameters have to be set before the simulation, and molecules must be produced and placed in the simulation box. There should be a reasonable distance tolerance between atoms when atoms are placed into the simulation box since any physical overlap between atoms would cause an unrealistic interaction. Normally, for gas and liquid simulation systems, atoms are distributed randomly in the box with a distance tolerance. While for the solid system, the initial configuration is created based on the component's crystal structure obtained from the experiment.

It is not compulsory to assign an initial velocity for atoms that ensures the starting initial kinetic energy is correctly related to the temperature. But an initial velocity could help to reduce the equilibration time. The initial velocities are given random values corresponding to the start temperature. The relationship between the velocities of the atom and the assigned temperature is described by:

$$\left\langle \frac{1}{2}\sum_i m_i v_i^2 \right\rangle = \frac{3}{2} N k_B T \tag{2.1}$$

where m is the mass of atoms, v is the velocity of atoms, N is the atom number, k_B is the Boltzmann constant, and T is the temperature. To start a simulation, random velocities are typically assigned to atoms using the Maxwell-Boltzmann distribution given by:

$$p(\mathbf{v}_i) = \left(\frac{M_i}{2\pi k_B T} \right)^{1/2} \exp\left(-\frac{M_i \mathbf{v}_i^2}{2 k_B T} \right) \tag{2.2}$$

where $\mathbf{v}_i$ is velocity of particle i, M_i is mass of particle i, k_B is Boltzmann constant, and T is temperature.

2.2.2 Time step

The Time step is an important parameter that needs to be specified before simulation, and the value of time step limits the length of the MD trajectory and the simulation. Typically, the time step for most of the MD simulation is on the femtosecond (fs) scale. Larger time steps allow for longer simulation results. However, the value of the time step is limited by the highest frequency of chemical bond vibration. For organic simulation, the chemical bond formed between the hydrogen atom and other atoms has the highest frequency vibration as hydrogen is the lightest atom. The value of the assigned time step should be ten times lower than the highest frequency [96]. Too large timesteps can cause an MD simulation to become unstable with energy increasing rapidly with time. The distance between atoms could be too close if the time interval of the position update is too long, which would cause a huge repulsive force and a high atom’s velocity. The atom would be “lost” if the movement of the atom exceed the box length within a single time step. Nevertheless, too small a time step would be highly computational cost. One strategy to solve this problem is to constrain all bonds containing hydrogen atoms. Thus, the vibration of hydrogen contained bonds would be neglected. Therefore, it is necessary to consider both calculation time and accuracy when choosing a time step.

2.2.3 Periodic boundary conditions

Computer simulations using atomistic models are usually performed on small systems, usually on the order of several thousand atoms. This is certainly not a good representation for a macroscopic sample because most of the particles will be situated near the “boundary”. For a simple cubic lattice with 1000 molecules, around 50% of them lie on the surface. The behaviour of these atoms lied on the surface is different from that of in the bulk if a real physical wall was set in the simulation cell. The application of periodic boundary conditions (PBC) helps in minimising the edge effects and enables us to treat only a relatively small system of around 100~10000 particles to obtain reasonable results. A schematic representation of periodic boundary conditions is presented in Fig. 2.3. Under this scheme, atoms are packed into a space-filling box, which is surrounded by translated copies of itself. This primary cell is surrounded by 8 and 26 image cells in two dimensions and three dimensions, respectively. The coordinates of the atoms in the image cell are equal to the coordinates of the corresponding particles in the primary cell plus a multiple of the grid length. The atoms in each cell move identically during the simulation. Therefore, if an atom hits a boundary, it reappears on the other side of the cell instead of bouncing back.

The minimum image convention was adopted to compute the potential energy or the force between particles. When two particles *i* and *j* are placed in a cubic box with length *L*. The convention dictates that it must adopt the minimum distance across the walls or between images in the neighbouring replicas. It can be expressed as:

$$x_{j,x}^{new} = \begin{cases} x_{j,x} - L, & r_{ij,x} > L/2 \\ x_{j,x} + L, & r_{ij,x} < -L/2 \end{cases} \tag{2.3}$$

If $r_{ij} > L/2$, then the particle *j* will be disregarded as an interaction partner of *i*, with its left image, having coordinate r_j - L in its place. The new coordinate r_j - L would be used to calculate the energy between particle *i* and *j*. An analogous rule holds for $r_{ij} < -L/2$ and for the other coordinates.

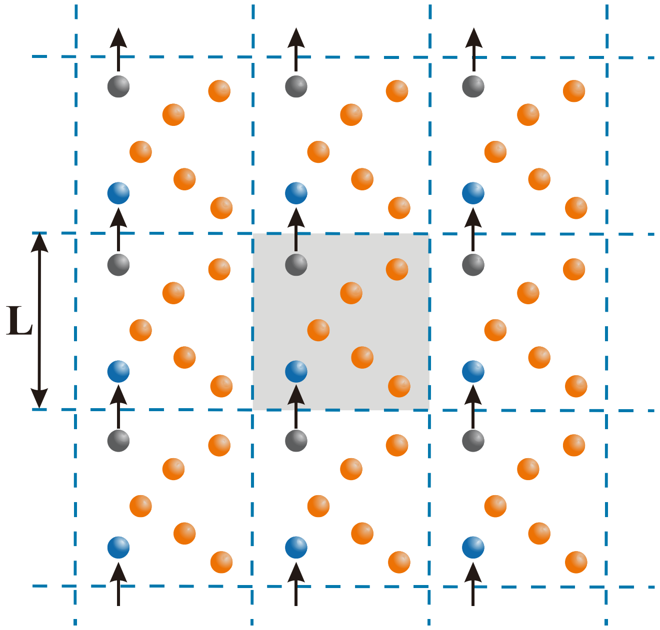

Fig. 2.3 A schematic representation of periodic boundary conditions in two dimensions. The box in the centre represents the original box with the particles of the system. The 8 boxes drawn around the centre box are the imaginary boxes, and they are filled with fictitious particles. Each box is the replica of the principal one. Whenever an atom moves away from the principal simulation box, the same happens with the fictitious atoms in the other boxes. The dashed line represents the boundary of the box, but this boundary is not a physical wall, and particles can freely pass through it. The gray atoms represent atoms crossing out of the box, while the blue atoms represent corresponding atoms entering the box from the opposite side. The orange atoms represent other atoms that have not crossed the boundary.

2.2.4 Ensembles

In MD simulations, an ensemble is a statistical representation of a system in thermodynamic equilibrium. The system is characterised by a set of variables, such as temperature, pressure, and energy, that are allowed to fluctuate within certain limits. The ensemble concept is used to describe the behaviour of the system over time and to predict its properties at equilibrium. Table 2.1 shows a comparison of the classical ensemble types used in this study and the corresponding macroscopic thermodynamic systems.

The microcanonical ensemble, also known as the NVE ensemble (for constant Number of particles, Volume, and Energy), is a statistical ensemble to study the energy distribution of a system at a given energy. In this ensemble, the system is isolated, and the total energy is fixed. This means that the system is not in exchange with a heat bath and the temperature is not allowed to fluctuate. The NVE ensemble is useful for studying the energy distribution of a system at a given energy, as well as for understanding the role of statistical fluctuations in the behaviour of a system. It is also useful for comparing results from different simulations and for understanding the effect of external perturbations on the system.

The canonical ensemble (NVT) is a statistical ensemble to study the thermodynamic properties of a system at a given temperature. The imposed variables in NVT ensemble are the volume V, the temperature T, and the number of particles N. In this ensemble, the system is in exchange with a heat bath at a fixed temperature, and the energy of the system is allowed to fluctuate. The NVT ensemble is useful for studying the thermodynamic properties of a system at a given temperature, such as the internal energy, the heat capacity, and the entropy. It is also useful for comparing results from different simulations and for understanding the effect of temperature on the behaviour of a system.

The imposed variables in the isothermal-isobaric ensemble (NPT), also known as the grand canonical ensemble, are pressure P, temperature T, and the number of particles N. It is used to study the thermodynamic properties of a system at a given temperature and chemical potential. In this ensemble, the system is in exchange with a heat bath and a particle reservoir at a fixed temperature and chemical potential, and the energy in the system are allowed to fluctuate. The NPT ensemble is useful for studying the thermodynamic properties of a system at a given temperature and chemical potential, such as the internal energy, the heat capacity, the entropy, and the chemical potential.

Table 2.1 Comparison of the classical ensemble types.

Ensembles	Imposed variables	Fluctuating properties (constraints)	Corresponding thermodynamic system
Microcanonical (NVE)	number of particles N volume V internal energy E	energy (quantum state) of each particle ε_i	isolated
Canonical (NVT)	number of particles N volume V temperature T	internal energy E	closed
Isothermal-isobaric (NPT)	number of particles N pressure P temperature T	volume V internal energy E	-

2.2.5 Temperature/pressure control

- Thermostats-simulations in NVT ensemble

In order to accurately compare the results of MD simulations to experimental data, it is important to conduct the simulations under conditions that closely match the experimental conditions. This often involves setting the temperature and pressure to constant values and allowing the system to reach equilibrium. The probability distribution of velocities within the system can be used to determine the temperature of the system using Equation (2.1), which relates the kinetic energy of the system to the temperature. Solving the equation for the instantaneous temperature τ gives:

$$\tau(t)=\frac{\sum_{i=1}^{N}\frac{m_i}{2}\mathbf{V}_i^2(t)}{N_f k_B} \tag{2.4}$$

where N_f represents the degrees of freedom of the system. One of the feasible methods for controlling the temperature is to scale the velocities by a factor λ so that the resultant kinetic energy of the system matches to the imposed temperature T, i.e.,

$$T=\frac{\sum_{i=1}^{N}\frac{m_i}{2}\left[\lambda(t)\mathbf{V}_i^2(t)\right]}{N_f k_B} \tag{2.5}$$

Hence, the required scaling factor is given by:

$$\lambda(t)=\sqrt{\frac{T}{\tau(t)}} \tag{2.6}$$

Although velocity scaling is the most straightforward method for adjusting the system's temperature. It does not provide a canonical distribution and cannot accurately disclose the energy fluctuation owning to the thermophysical process in the molecular system. Consequently, it is typically used during the equilibrium stage.

Berendsen et al. [97, 98] developed an approach for controlling temperature by coupling a constant-temperature external bath to the simulation system. The velocities of particles are adjusted through a time scale σ_T at each time step, similar to the velocity rescaling method. So that the scaling factor λ for updating the velocity is given by:

$$\lambda^2=1+\frac{\Delta t}{\sigma_T}\left(\frac{T}{\tau(t)}-1\right) \tag{2.7}$$

There are several methods that can be used to control the temperature in MD simulations, including the Berendsen thermostat [97, 98], Andersen thermostat [99], and Nosé-Hoover thermostat [100, 101]. The Berendsen thermostat is a simple method that suppresses variations in the kinetic energy of the system, but it does not strictly generate a canonical ensemble and cannot accurately reproduce the correct probabilities for the system [98]. The Andersen thermostat is a more sophisticated method that couples the system to a heat bath through the use of imaginary heat bath particles that interact with the system's particles through stochastic collisions. These collisions allow the system to visit all accessible energy levels according to their Boltzmann weight, resulting in a canonical probability distribution [102]. However, the stochastic nature of the collisions can disturb the dynamics in an unrealistic way, leading to an enhanced decay of the velocity autocorrelation function and a change in the diffusion constant [102]. As a result, the Andersen thermostat should not be used for investigations into time-independent properties. The Nosé-Hoover thermostat is another method that involves coupling the system to a heat bath, but it uses a different approach that avoids the unrealistic dynamics introduced by the Andersen thermostat.

The Nosé-Hoover thermostat was initially developed by Nosé [100] and was improved further by Hoover [101]. They extended the system Hamiltonian by introducing a heat reservoir and a friction parameter (ζ) into the equations of motion. The time evolution of the friction parameter is described by the difference between the instantaneous temperature of the system $\tau(t)$ and the imposed temperature T:

$$\frac{d\zeta}{dt} = \frac{N_f k_B}{Q_T}\left[\tau(t) - T\right] \tag{2.8}$$

where Q_T is the effect mass of the reservoir. In Hoover's formulation, $N_f = 3N$ based on the translational degrees of freedom of the N particles of the system. Q_T is an adjustable parameter in the simulation as the coupling strength of the heat bath is determined by Q_T. A high value of Q_T indicates a sluggish energy exchange between the system and the heat bath. The friction parameter evolution function is developed using explicit velocity functions such as leap frog and velocity-Verlet, described in Section 2.2.6. Nosé-Hoover is the most popular thermostat that preserves the canonical ensemble distribution in configuration and momentum space.

- Barostats-simulations in NPT ensemble

Experimental studies are often conducted under constant pressure, such as at atmospheric pressure. Therefore, in addition to imposed temperature, the pressure in MD simulation also needs to be restricted. A macroscopic system reacts on an imposed pressure (P) by changing its volume. Accordingly, pressure control in simulation studies involves volume fluctuations of the simulation box. Therefore, the straightforward method to control the pressure is to scale the simulation volume. A scaling factor χ for the volume changing is introduced in Berendsen barostat, which is given by:

$$\chi(t) = 1 - k_T \frac{\Delta t}{\alpha_P}\left[P - p(t)\right] \tag{2.9}$$

where α_p is the time scale of the volume scaling, $p(t)$ is the instantaneous pressure of the system, and k_T is the isothermal compressibility. The volume of the simulation box is then scaled by χ, whereas the centre-of-mass coordinates of the particles and the cell factors are scaled by $\chi^{1/3}$. Notably, the Berendsen barostat produces simulations with the proper average pressure, and it does not produce the identical NPT ensemble. Nosé-Hoover barostat or Parrinello-Rahman barostat should be used in simulations where the changes in pressure or volume are essential, such as for calculating thermodynamic properties.

2.2.6 Integrating equations of motion

In a system with N particles, the force acting on the particle is caused by the interaction with other N-1 particles. The force can be calculated using the gradient of the system's potential energy (U). Potential energy is a function of atom positions (**r**), which are traditionally categorised as intermolecular and intramolecular interactions. The total potential energy is summed for non-bonded potential (such as Lennard-Jones and Coulomb) and bonded terms. A detailed description of potential energy is introduced in the following Section of 2.3 and 2.4. The force on an atom can be calculated from the change in energy between its current position and its position a small distance away. This can be recognised as the derivative of the energy with respect to the change in the atom's position:

$$\mathbf{F}_i = -\frac{\partial U(\mathbf{r})}{\partial \mathbf{r}_i} \tag{2.10}$$

The atomic forces and masses can then be used to calculate the positions of each particle along a series of tiny time steps. The series of structural changes over time are called a trajectory. The positions of particles at each timestep are updated by integrating Newton's second law of motion expressed as:

$$\mathbf{F}_i = m_i \mathbf{a}_i = m_i \frac{d^2 \mathbf{r}_i}{dt^2} \tag{2.11}$$

where $\mathbf{F}_i$ is the force placed on the atom, and $\mathbf{a}_i$ is acceleration. The motions of all particles are coupled since each particle simultaneously interacts with all others in the system. It is impossible to solve the system's second-order differential equation's analytical integral with thousands of atoms. The slow solution of the equations of motion using a finite difference method is performed using an integration algorithm. A prevalent algorithm is the Verlet algorithm [103]. This is derived from a Taylor expansion of the positions about time *t*:

$$\mathbf{r}(t+\delta t) = \mathbf{r}(t) + \frac{\mathrm{d}\mathbf{r}}{\mathrm{d}t}\delta t + \frac{1}{2!}\frac{\mathrm{d}^2\mathbf{r}}{\mathrm{d}t^2}\delta t^2 + \ldots \tag{2.12}$$

$$\mathbf{r}(t-\delta t) = \mathbf{r}(t) - \frac{\mathrm{d}\mathbf{r}}{\mathrm{d}t}\delta t + \frac{1}{2!}\frac{\mathrm{d}^2\mathbf{r}}{\mathrm{d}t^2}\delta t^2 + \ldots \tag{2.13}$$

By adding the above equations, lead to:

$$\mathbf{r}(t+\delta t) = 2\mathbf{r}(t) - \mathbf{r}(t-\delta t) + \frac{\mathrm{d}^2\mathbf{r}}{\mathrm{d}t^2}\delta t^2 \tag{2.14}$$

Velocities can be calculated from:

$$\mathbf{v}(t) = \frac{1}{2\delta t}[\mathbf{r}(t+\delta t) - \mathbf{r}(t-\delta t)] \tag{2.15}$$

Numerous modifications have been made to the Verlet method in an effort to improve its accuracy and increase its efficiency, such as the leap frog algorithm [104] and Velocity-Verlet algorithm [105]. The formulas are summarised as follows:

Leap Frog

$$\mathbf{r}_i(t+\delta t)=\mathbf{r}_i(t)+\mathbf{v}_i(t+\frac{1}{2}\delta t)\delta t \tag{2.16}$$

$$\mathbf{v}_i(t+\frac{1}{2}\delta t)=\mathbf{v}_i(t-\frac{1}{2}\delta t)+\mathbf{a}_i(t)\delta t \tag{2.17}$$

$$\mathbf{v}_i(t)=\frac{1}{2}\left[\mathbf{v}_i(t+\frac{1}{2}\delta t)+\mathbf{v}_i(t-\frac{1}{2}\delta t)\right] \tag{2.18}$$

Velocity-Verlet

$$\mathbf{r}_i(t+\delta t)=\mathbf{r}_i(t)+\mathbf{v}_i(t)\delta t+\frac{1}{2}\mathbf{a}_i(t)\delta t^2 \tag{2.19}$$

$$\mathbf{v}_i(t+\frac{1}{2}\delta t)=\mathbf{v}_i(t)+\frac{1}{2}\mathbf{a}_i(t)\delta t \tag{2.20}$$

$$\mathbf{v}_i(t+\delta t)=\mathbf{v}_i(t+\frac{1}{2}\delta t)+\frac{1}{2}\mathbf{a}_i(t+\delta t)\delta t \tag{2.21}$$

2.3 Classical force field

A classical force field is a mathematical model that is used in MD to describe the interactions between atoms. It typically consists of a set of equations that define the forces between atoms as a function of their positions, and it is used to calculate the motion of the atoms over time. The force field can be based on various physical principles, such as electrostatic interactions, van der Waals forces, and covalent bonding. It is typically parameterised using experimental data or ab initio calculations. Classical force fields are an important tool in chemistry, biochemistry, and materials science, as they can provide insight into the structure, dynamics, and behaviour of molecules and materials. This class includes the Assisted Model Building with Energy Refinement (AMBER) [106], Optimised Potentials for Liquid Simulations (OPLS) [107], Chemistry at Harvard Macromolecular Mechanics (CHARMM) [108], Transferable Potentials for Phase Equilibria (TraPPE) [109] etc. OPLS force field is selected to introduce the potential energy in the MD system as it was used in this study.

The potential energy in the OPLS force field is divided into non-bonded and bonded interaction, as presented in Fig. 2.4. The energy of non-bonded interactions between atoms is described based on Coulomb potential and the vdW interactions by 12-6 Lennard-Jones (LJ) function:

$$U_{nb}(r_{ij})=\frac{q_i q_j}{4\pi\varepsilon_0 r_{ij}}+4\varepsilon_{ij}\left(\left(\frac{\sigma_{ij}}{r_{ij}}\right)^{12}-\left(\frac{\sigma_{ij}}{r_{ij}}\right)^{6}\right) \tag{2.22}$$

where r_{ij} is the distance between atoms i and j, q_i and q_j are the partial charges on the atoms, ε_0 is the permittivity of vacuum, σ_{ij} is the vdW radius, and ε_{ij} is the well-depth for this atom pair. The LJ function parameters σ and ε for interactions between different atoms can be calculated by using arithmetic average and geometric average: $\sigma_{ij} = (\sigma_{ij}+\sigma_{ij})/2$ and $\varepsilon_{ij} = (\varepsilon_{ij}\varepsilon_{ij})^{1/2}$.

The bonded interaction involves the bond stretching potential (U_b), angle bending potential (U_θ), and bond rotation potential (U_ϕ), the equations for calculating each potential are given as:

$$U_b = \frac{1}{2} k_{ij}^{b} (r_{ij} - b_0)^2 \tag{2.23}$$

$$U_\theta = \frac{1}{2} k_{ijk}^{\theta} (\theta_{ijk} - \theta_0)^2 \tag{2.24}$$

$$U_\phi = \frac{1}{2}\left(\sum_{n=1}^{4} k_{ijkl}^{\phi} \left(1 + (-1)^{n+1} \cos(n\phi)\right)\right) \tag{2.25}$$

where k^b, k^θ, and k^ϕ are bond, angle, and dihedral force constants, respectively. r represents the bond length between two atoms, θ is the angle of the bond, and ϕ is the dihedral angle. Subscript "eq" is the equilibrium value of bond and angle terms. The total potential energy is the sum of potential described above, i.e.:

$$U_{total} = U_{nb} + U_b + U_\theta + U_\phi \tag{2.26}$$

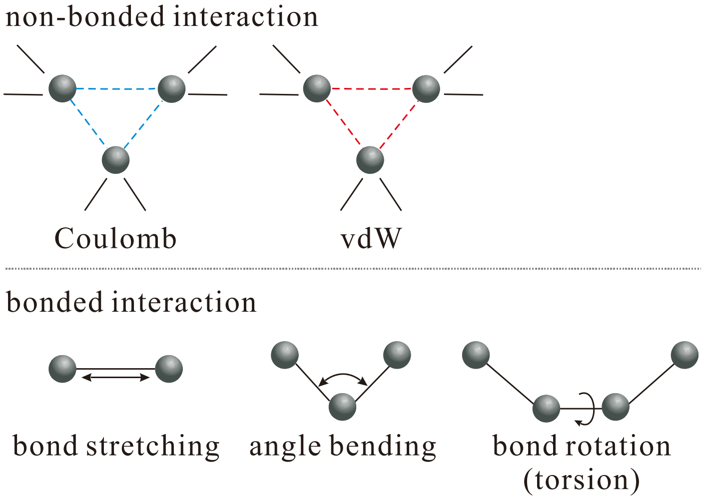

Fig. 2.4 A schematic representation of non-bonded and bonded interactions in MD.

2.4 Reactive force field

The classical force fields cannot model chemical reactions because of the requirement of breaking and forming bonds. The reactive force field (ReaxFF) developed by van Duin et al. [43] can be used to simulate the bonds breaking and forming. The description of connectivity-dependent interactions in the ReaxFF force field is based on bond order formalism. Bond order is determined by interatomic distance using an empirical formula, including contributions from σ, π and ππ bonds. The chemical reactions during the time intervals can be analysed based on the interatomic potential and the bond order. Nonbonded interactions, such as Coulomb and van der Waals interaction, are calculated independently. The charge equilibration (QEq) method [110] adjusts the partial charge on individual atoms. The following equation calculates the energy of each particle:

$$E_{system} = E_{bond} + E_{over} + E_{under} + E_{lp} + E_{val} + E_{tor} + E_{vdWaals} + E_{coulomb} \tag{2.27}$$

where E_{bond}, E_{over}, E_{under}, E_{lp}, E_{val}, E_{tor}, $E_{vdWaals}$, and $E_{coulomb}$ stand for bond energy, overcoordination energy penalty, undercoordination stability, lone pair energy, three-body valence angle energy, four-body torsional angle energy, van der Waals energy, and Coulomb energy, respectively.

A fundamental assumption of ReaxFF is that the bond order BO_{ij} between a pair of atoms can be obtained directly from the interatomic distance r_{ij} as given by:

$$\begin{aligned} BOij &= BO_{ij}^{\sigma} + BO_{ij}^{\pi} + BO_{ij}^{\pi\pi} \\ &= \exp\left[p_{bo1}\left(\frac{r_{ij}}{r_0^{\sigma}}\right)^{p_{bo2}}\right] + \exp\left[p_{bo3}\left(\frac{r_{ij}}{r_0^{\sigma}}\right)^{p_{bo4}}\right] + \exp\left[p_{bo5}\left(\frac{r_{ij}}{r_0^{\sigma}}\right)^{p_{bo6}}\right] \end{aligned} \tag{2.28}$$

where BO is the bond order between atoms i and j, r_{ij} is interatomic distance, r_0 terms are equilibrium bond lengths, and p_{bo} terms are empirical parameters. Interatomic distance dependency of the carbon-carbon bond order is presented in Fig. 2.5.

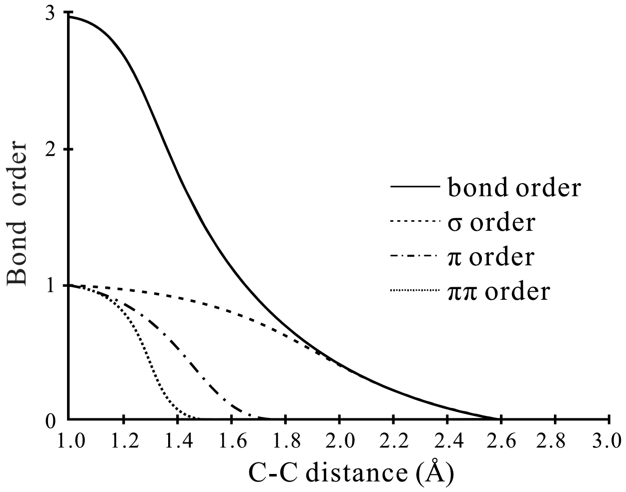

Fig. 2.5 Interatomic distance dependency of the carbon-carbon bond order [43].

2.5 Conclusions

This chapter has provided an overview of MD simulations, which is a widely used computational tool for investigating the behaviour of biological and chemical systems at the atomic scale. The simulation of molecular systems provides insights into their thermodynamic and kinetic properties, conformational changes, and reaction mechanisms. These insights are critical for understanding the fundamental aspects of various molecular systems and have applications in many aspects, including drug design, material science, and catalysis.

The fundamentals of MD simulations and the basic methodologies involved in carrying out these simulations were discussed. The simulation of molecular systems relies on a classical mechanics approach, and the accuracy and efficiency of MD simulations are highly dependent on the choice of force fields and simulation parameters. In the future, the development of more accurate force fields and efficient simulation techniques will improve the accuracy and applicability of MD simulations, enabling us to gain further insights into the behaviour of complex molecular systems. MD simulations have revolutionised the way we study molecular systems, and this chapter has provided a foundation for understanding the basics of this powerful computational tool.

Chapter 3

Nickel Catalysed Gasification of Cellulose in Supercritical Water

Biomass gasification is one of the promising approaches to producing H_2-riched syngas. The catalytic gasification mechanism of cellulose, the main structural component of lignocellulose biomass, still presents some knowledge gaps. In this Chapter, the ReaxFF molecular dynamics simulation of Ni catalysed gasification of cellulose in supercritical water is carried out. The effect of Ni on the depolymerisation and ring-opening process of cellulose is presented in Section 3.2.1. The influence of Ni and cellulose-to-water mass ratio (C/W) on the gaseous product yield is investigated in Section 3.2.2 and Section 3.2.3. In Section 3.2.4, the effect of temperature and C/W on carbon deposition rate on Ni catalyst is studied.

3.1 MD modelling methodology

3.1.1 Model construction

All MD simulations in this work were conducted using the ReaxFF force field [111]. The C/H/O/Ni parameter set [36, 112] developed for modelling hydrocarbon chemistry catalysed by Ni was adopted to study the cellulose SCWG catalysed by Ni nanocatalysts. The verification of the adopted force field was carried out in our previous work [113].

Cellulose $(C_6H_{10}O_5)_n$ is a polysaccharide consisting of a linear chain of several hundred to many thousands of β-1,4 linked D-glucopyranose units. Fig. 3.1 shows the model used in the MD simulations. The model construction starts with a monomer, and the unimolecular D-glucopyranose was built and optimised using the Materials Studio [114] Forcite module. Ten D-glucopyranose monomers were connected to form a polymer, as shown in Fig. 3.1(c). Face-centred cubic lattice of NiNP was created on a web-based crystallographic tool [115]. The minimum surface energy of corresponding Miller indices of (111), (100) and (110) was adopted from the work of Chen et al. [113]. The melting temperature of NiNP depends on its size, and the melting temperature decreases with decreasing radius of NiNP. The melting temperature of 3 nm NiNP simulated with the ReaxFF force field is around 1700 K [113], which is lower than the simulation temperature (1800 K~2200 K) in this study. NiNP with a diameter of 4.0 nm was adopted to maintain the integrity of NiNP during the simulation in this study.

Eight reaction systems S1~S8 were built to investigate the Ni catalytic SCWG of cellulose, as listed in Table 3.1. Different cellulose molecule numbers have been tested to eliminate the effect of atom number on the simulation results. The yields of H_2, CO, and CO_2 in the systems with varying numbers of cellulose molecules (8, 10, 15, 20, and 30) are presented in Fig. 3.1. The results show that when the number of cellulose molecules in the system reaches 10 under the same temperature, pressure, and C/W conditions, the gas production per unit mass of cellulose was found to be approximately similar. Therefore, 10 cellulose molecules were adopted to ensure the validity of simulation results and minimise computational costs. To observe the reactions that occur on the Ni surface, the catalyst to biomass ratio considered is relatively high. Cases S1~S6 are used to study the effects of temperature and catalyst on the SCWG of cellulose. Cases S5, S7, and S8 are used to study the effect of cellulose-to-water mass ratio (C/W) on the catalytic SCWG of cellulose. The system pressure would affect the yield of gaseous products. An increase in pressure will shift the methanation reactions ($CO+3H_2 \leftrightarrow CH_4+H_2O$, $CO_2+4H_2 \leftrightarrow CH_4+2H_2O$) to the right, thereby enhancing the formation of CH_4 [13]. Therefore, the simulation box dimensions were adjusted to keep the same pressure in systems S7 and S8 with varying water molecules.

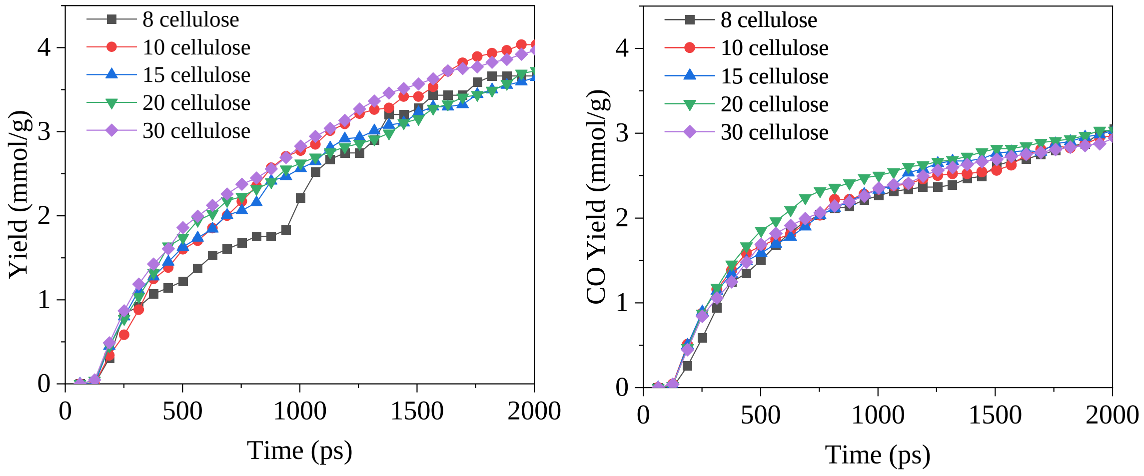

(a) (b)

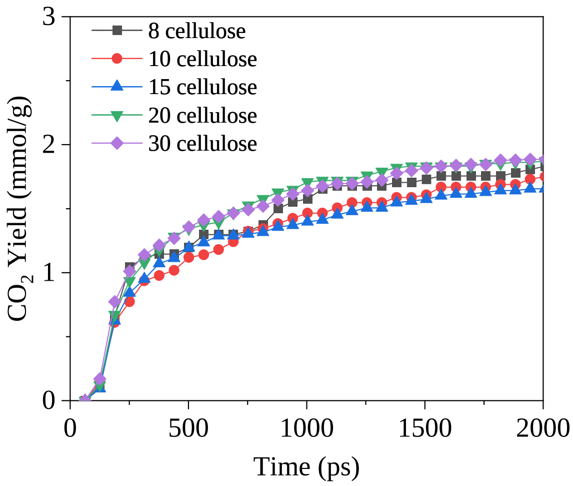

(c)

Fig. 3.1 The yields of H_2, CO, and CO_2 in systems with varying numbers of cellulose molecules.

Table 3.1 Detailed simulation cases for the studied systems of Ni catalytic SCWG of cellulose

Cases	Cellulose molecules	Water molecules	C/W	Catalyst	Temperature	Box dimensions (Å)
S1	10	600	3:2	-	1800 K	90×90×90
S2	10	600	3:2	-	2000 K	90×90×90
S3	10	600	3:2	-	2200 K	90×90×90
S4	10	600	3:2	NiNP	1800 K	90×90×90
S5	10	600	3:2	NiNP	2000 K	90×90×90
S6	10	600	3:2	NiNP	2200 K	90×90×90
S7	10	900	3:3	NiNP	2000 K	98×98×98
S8	10	300	3:1	NiNP	2000 K	85×85×85

Sorensen and Voter [116] pointed out that an elevated temperature could accelerate the reaction process and thus significantly extend the simulation time scale, which has become a familiar and effective strategy in ReaxFF MD simulation [33, 117]. For reaction rates described by the Arrhenius equation, increasing the temperature would increase the reaction rates but not the activation energy barrier. Salmon et al. [118] studied coal pyrolysis using ReaxFF simulation at an elevated temperature. They compared the simulated product distribution with experimental results and concluded that elevated temperature did not influence the reaction pathways during coal pyrolysis. Accordingly, elevated reaction temperatures were chosen in this work to study the catalytic mechanism of Ni during the SCWG of cellulose.

3.1.2 Simulation setup procedures and details

Initial configurations of all models were built by using Packmol programme [119]. Cellulose and water molecules are distributed randomly into the cubic box, and the box dimensions are listed in Table 3.1. In catalytic SCWG (e.g., cases S4~S8), NiNP was fixed in the centre of the unit cell and water and cellulose molecules are distributed around, as shown in Fig. 3.1(e). After system energy minimisation, the simulation cell was relaxed at 300 K for 20 ps. Subsequently, the equilibrated system was heated to the final reaction temperature with a heating rate of 15 K/ps. Then, the simulations would last at the target temperature for 2 ns. All simulations were performed using an NVT ensemble. A time step of 0.25 fs was assigned. The trajectories and species information were outputted every 100 steps. The linear and angular momentum of NiNP was zeroed every 10 timesteps.

The periodic boundary condition was applied in all directions. The initial velocities for all atoms were generated randomly following the Maxwell-Boltzmann distribution. Nosé-Hoover thermostat and barostat were adopted to control the system temperature and pressure with a temperature and pressure damping constant equal to 100 times and 1000 times of the time step, respectively. A bond order of 0.3 was employed to identify chemical bonds between pairs of atoms. All simulations were repeated three times with different initial configurations and velocity distributions. The ReaxFF MD simulations were performed with the REAXC package [120] in the Large-scale Atomic/Molecular Massively Parallel Simulation (LAMMPS) [121].

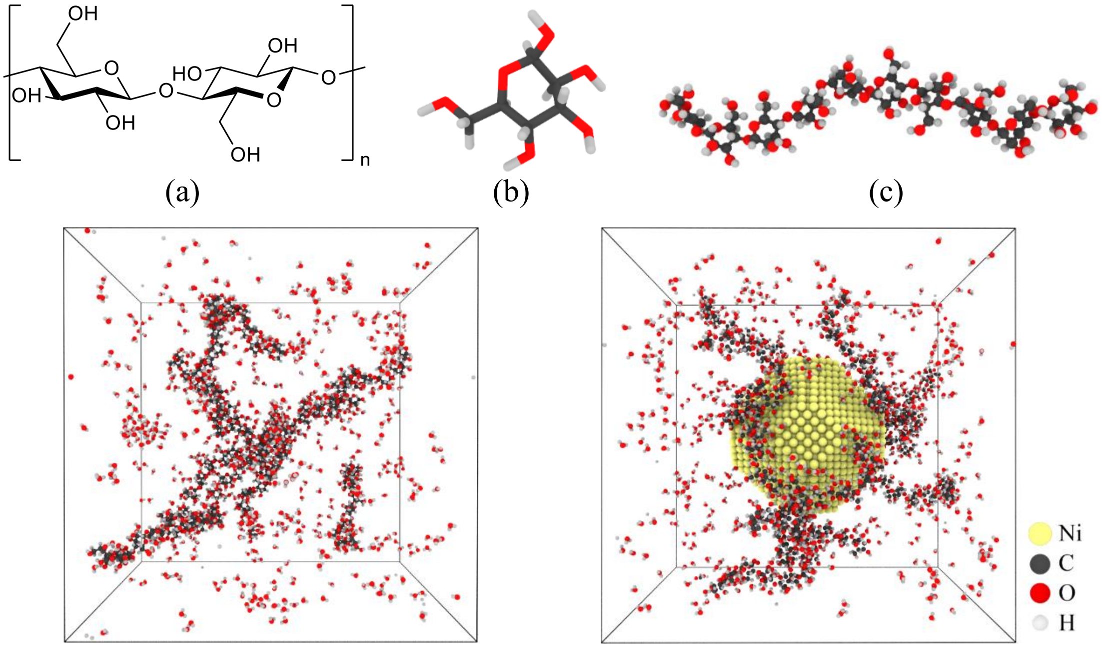

(a) (b) (c)

(d) (e)

Fig. 3.2 MD simulation model: (a) Structural formula of cellulose; (b) D-glucopyranose molecule; (c) Constructed cellulose structure with ten β-1,4 linked D-glucopyranose units; (d) Noncatalytic SCWG of cellulose; (e) Ni catalytic SCWG of cellulose, where NiNP was fixed in the centre with water and cellulose molecules distributed around.

3.2 Results and discussion

3.2.1 The effect of Ni on the depolymerisation and ring-opening process of cellulose

The first step in cellulose conversion involves its depolymerisation to oligomers or D-glucopyranose [14], which undergoes hydrolysis to form liquid-phase organic intermediates via scission of C-C and C-O bonds. Guo et al. [20] established the mechanism of Ru catalytic gasification of D-glucopyranose. Hydroxyl groups are adsorbed to the catalytic Ru surface predominantly through oxygen atoms. The reactant undergoes dehydrogenation on the catalyst surface, followed by subsequent cleavage of C-C or C-O bonds, which results in syngas production. However, the detailed adsorption and degradation process on catalyst surfaces are not readily accessible by experiments.

The depolymerisation and ring-opening percentage of cellulose during the heating period in cases S2 and S5 are shown in Fig. 3.2(a) and (b). The depolymerisation and ring-opening percentage are computed by the following equations:

$$\text{Depolymerisation percentage} = \frac{\text{Cleavage of } \beta\text{-1,4 linkage}}{\text{Initial number of } \beta\text{-1,4 linkage}} \times 100\ (\%) \tag{3.1}$$

$$\text{Ring-opening percentage} = \frac{\text{Number of opened ring}}{\text{Initial number of ring}} \times 100\ (\%) \tag{3.2}$$

It can be seen that Ni could accelerate the depolymerisation and ring-opening process of cellulose. The depolymerisation and ring-opening occur at around 75 ps in the absence of Ni catalyst, and almost all β-1,4 linkages are cracked after 125 ps. While the start points of β-1,4 linkage cleavage and ring-opening are around at 50 ps in the presence of Ni catalyst, these processes were completed after 100 ps. The results show that decomposition of cellulose can occur at a lower temperature, which helps reduce the cost of biomass SCWG. The two cases show a similar onset time and evolution trend in depolymerisation and ring-opening processes, demonstrating that the ring-opening takes place immediately after cellulose is depolymerised into monomers. This is because the cleavage of β-1,4 linkage would lead to the structural instability of the corresponding monomer, resulting in the ring-opening of D-glucopyranose.

The ring-opening of the D-glucopyranose monomer can be achieved by the cleavage of the C-C or C-O bond. Fig. 3.2(c) shows the cleavage percentage of different types of bonds. Around 64% of rings were opened by the cleavage of the C-O bond in the absence of Ni, while this figure increases to 70% when Ni was added. This result suggests that more rings of D-glucopyranose tend to be opened via the cleavage of the C-O bond under the effect of Ni catalyst.

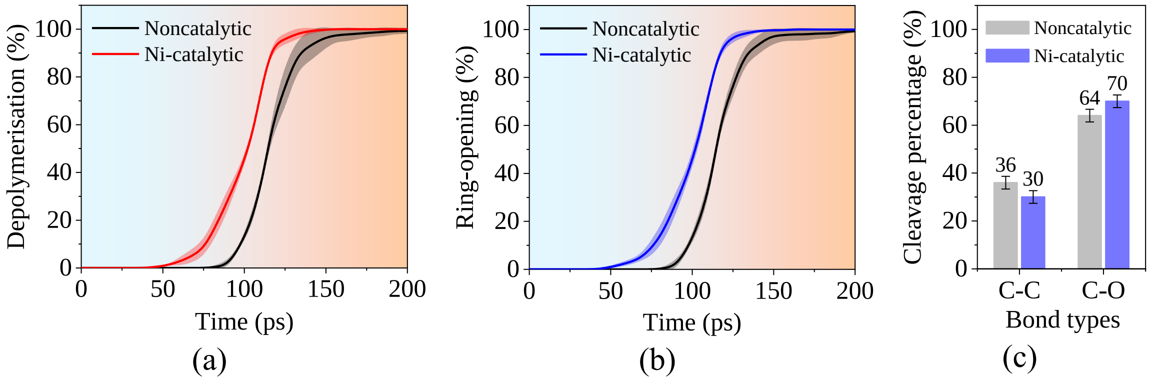

Fig. 3.3 (a) The depolymerisation and (b) ring-opening percentage of cellulose during the heating period in cases S2 and S5, the colour gradient (from blue to red) in the background represents increasing temperature; (c) Cleavage percentage of C-C and C-O bonds during the ring-opening process in cases S2 and S5.

Both high temperature and catalyst would promote bond breaking. The energy of atoms increases with increasing temperature, and the bonds between the atoms become more unstable and eventually break. Catalysts make this process more efficient by lowering the activation energy. If an atom forms a chemical bond with Ni atoms, the cleavage of other chemical bonds connected to this atom will take place. The cracking of such bonds is considered as catalytic cleavage and the others are considered as thermal cleavage. The thermal cleavage and catalytic cleavage of bonds during depolymerisation and ring-opening process in catalytic SCWG (case S5) are shown in Fig. 3.3. It can be seen that 87% and 88% of bond breakings take place via thermal cleavage during depolymerisation and ring-opening process, respectively. Thermal cleavage of bond plays a dominant role in the bond-breaking process. Therefore, depolymerisation and ring-opening rate in noncatalytic and catalytic SCWG are similar after 100 ps, when the temperature of the system reaches a certain value, as shown in Fig. 3.2.

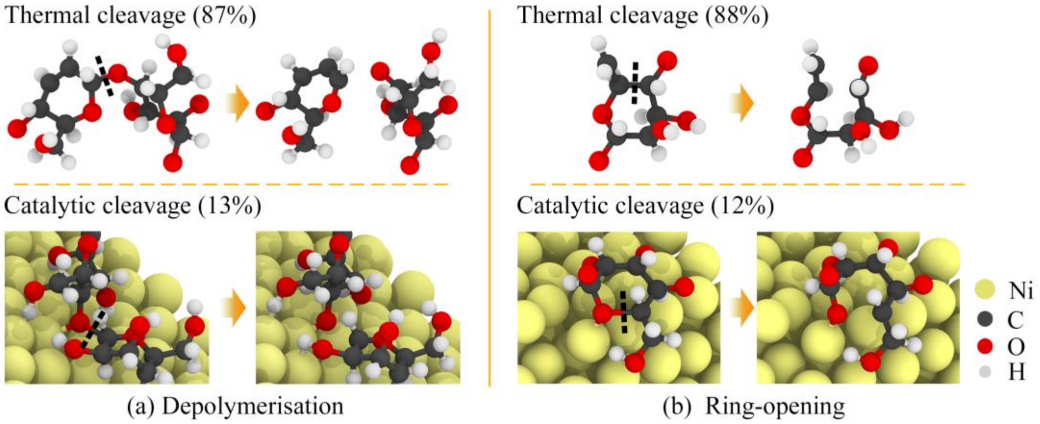

Fig. 3.4 Thermal bond cleavage and catalytic bond cleavage during (a) depolymerisation and (b) ring-opening process in case S5. The percentage represents the proportion of two types of cleavage. Black dash lines represent the bond cleavage sites.

As the skeleton of organic matters, the dissociation kinetics of C-C and C-O bonds play a vital role in cellulose decomposition. The decomposition reactions of D-glucopyranose were considered to be first-order reactions [122]. Initial and equilibrium numbers of C-C and C-O bonds can be used to calculate the activation energy of the corresponding bond [123, 124]. The reaction rate constant, *K*, is determined by the following equation [123]:

$$\ln N_0 - \ln N_{teq} = Kt_{eq} \tag{3.3}$$

where N_0 and N_{teq} are the numbers of C-C or C-O bonds at initial and equilibrium stages. The reaction rates are analysed by the Arrhenius equation:

$$K = A\exp\left(-\frac{E_a}{RT}\right) \tag{3.4}$$

where R is the universal gas constant. The activation energy (Ea) and the pre-exponential factor (A) in Eq. (5) are calculated by linear fitting. Fig. 3.4 shows the change in the activation energy of C-C and C-O bonds in the absence and presence of a catalyst. The activation energy of the C-C bond is 25.33 kJ/mol without catalyst, and this figure decreases to 24.02 kJ/mol when Ni catalyst is added. Activation energies for C-O bonds without and with Ni are calculated as 24.95 and 22.97 kJ/mol, respectively. It can be seen that the activation energy of C-O bonds is lower than that of C-C bonds. Thereby, the ring-opening of D-glucopyranose monomers is prone to take place via the cleavage of C-O bonds. Moreover, the activation energy reduction of C-O bonds (1.98 kJ/mol) under the effect of catalyst is more significant than that of C-C bonds (1.31 kJ/mol), demonstrating Ni is more efficient in the cleavage of the C-O bond than the C-C bond. Consequently, the proportion of C-O cleavage increases when Ni is added during the ring-opening process, as shown in Fig. 3.2(c). It has been reported that cellulose is easier to gasify than lignin in the presence of Ni catalyst [125], which can be explained by the structural differences between cellulose and lignin because there are more C-O bonds in cellulose molecules than in lignin.

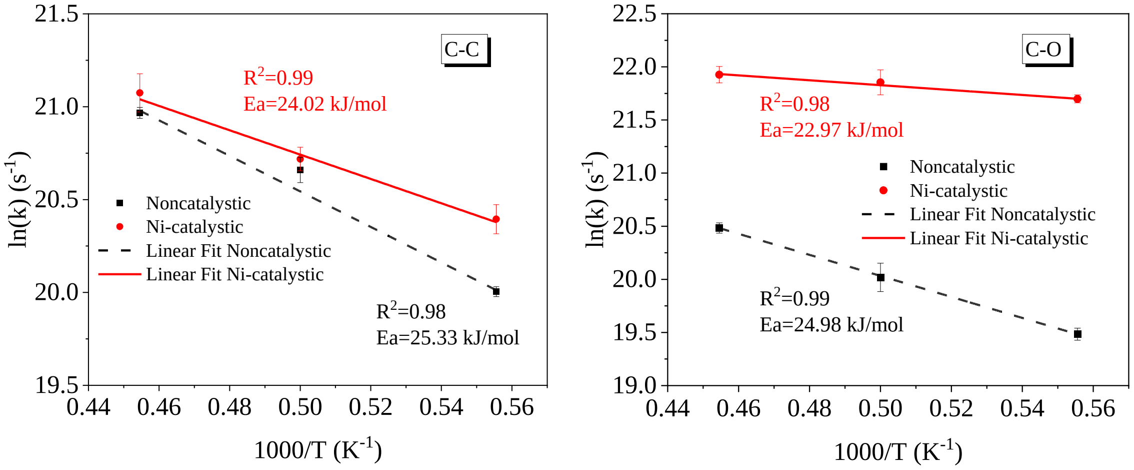

(a) (b)

Fig. 3.5 Temperature-dependent dissociation rates *k* of (a) C-C and (b) C-O bonds during the SCWG processes of cellulose (R^2 is the coefficient of determination).

3.2.2 The effect of Ni on the gaseous product yield

Fig. 3.5 shows the time evolution of the total number of H_2, CO, and CO_2 molecules at different temperatures during SCWG of cellulose in the absence and presence of Ni catalyst. Temperature is one of the most dominant parameters that affect the gaseous product yield, especially when the reaction occurs without a catalyst [13]. Generally, the gaseous produce yield increases with an increase in reaction temperature as high temperatures favour the scission of C-C and C-O bonds. The simulation results show that H_2 yield increases with increasing temperature, which is consistent with the experimental results [126]. The free radical reactions in water are believed to be temperature-dependent. When the conditions are above the critical point of water, free radical reactions dominate over ionic reactions [16]. Therefore, water splitting at higher temperature generates more H free radicals. In addition to water splitting reaction, biomass dehydrogenation reaction would also be enhanced at high temperatures [127]. The increase of H free radical number leads to the increase in H_2 yield, which will be discussed subsequently.

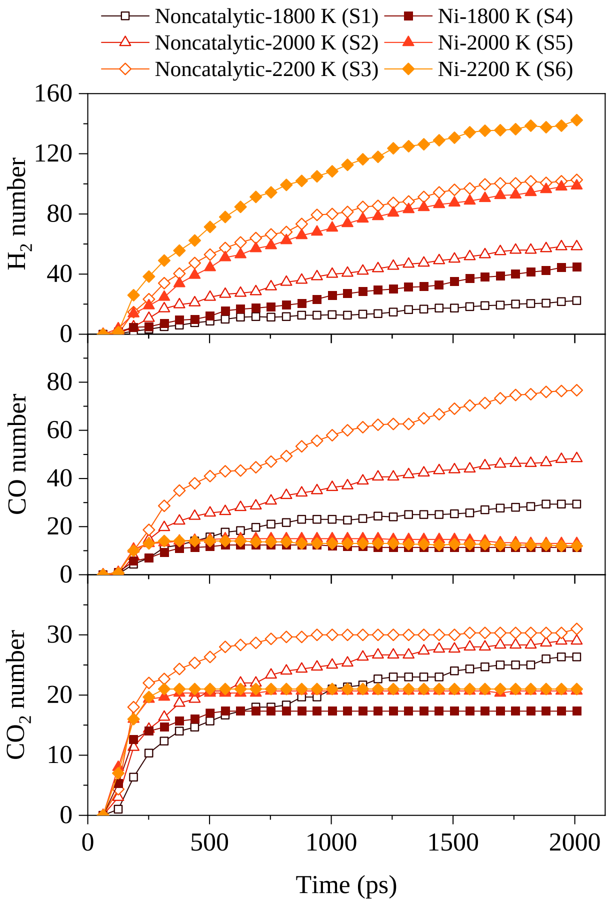

Fig. 3.6 Time evolution of the total number of H_2, CO, and CO_2 molecules at different temperatures during SCWG of cellulose with and without Ni catalyst.

Ni catalyst will significantly increase the yield of H_2, as shown in Fig. 3.5. The H_2 generation pathways were analysed to explore the effect of Ni on the H_2 production mechanism. The generation of H_2 is mainly through the following three pathways:

① $R\text{-}H + H^{\bullet} \rightarrow R^{\bullet} + H_2$

② $H_2O + H^{\bullet} \rightarrow H_2 + {}^{\bullet}OH$

③ $H^{\bullet} + H^{\bullet} \rightarrow H_2$

where pathway ①: hydrogen transfer reactions, where H radical interacts with the H atoms in cellulose to produce H_2 [27, 128]; pathway ②: H radical interacts with water to produce H_2 and ${}^{\bullet}OH$ at elevated temperature [27, 129]; pathway ③: H radical termination reaction, where two H radicals interact with each to produce H_2 [27, 128]. R is the abbreviation for any other groups.

The occurrence frequency and proportion of pathways ①~③ during SCWG of cellulose in the absence and presence of Ni catalyst are presented in Fig. 3.6(a) and Fig. 3.6(b), respectively. The results suggest that pathway ① plays a dominant role in the H_2 generation in the absence of Ni catalyst, especially at relatively low temperatures. It can be seen that around 68% of H_2 was produced via pathway ① in 1800 K. Only a few H_2 molecules were generated through pathway ③ without Ni catalyst. However, pathway ③ becomes the main H_2 generation path with the addition of Ni catalyst. More than 70% of H_2 molecules were generated via pathway ③, and this figure reached 82% in 1800 K. This is because a large number of H free radicals would be generated by the water splitting and cellulose dehydrogenation reactions on the Ni surface. Increasing the concentration of H free radical enhances the occurrence frequency of pathway ③. Meanwhile, the frequency of all three pathways increases with increasing temperature, and the increase of pathway ② is the most significant. Therefore, the proportion of pathway ② increases with increasing reaction temperature, as shown in Fig. 3.6(b).

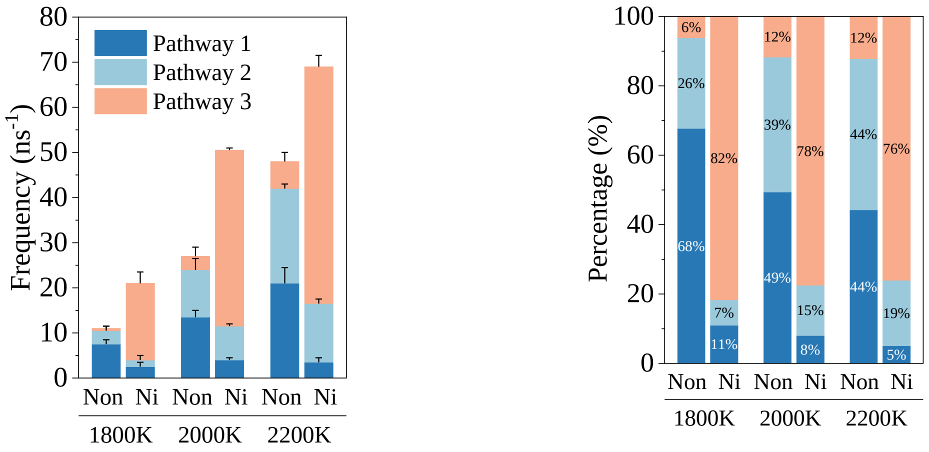

Fig. 3.7 The (a) frequency and (b) proportion of H_2 generation pathways ①~③ in the

absence and presence of Ni catalyst (cases S2 and S5).

The yield of H_2 is closely related to the number of H free radicals. The generation paths of H free radicals were analysed to investigate the effect of Ni on H_2 yield. The H radicals could be produced from the water splitting and cellulose dehydrogenation reactions, as listed in the following pathways:

④ $H_2O \leftrightarrow {}^{\bullet}OH + H^{\bullet}$

⑤ $R\text{-}O\text{-}H \leftrightarrow R\text{-}O^{\bullet} + H^{\bullet}$

⑥ $R\text{-}C\text{-}H \leftrightarrow R\text{-}C^{\bullet} + H^{\bullet}$

where pathway ④: free radical reaction of water, where H_2O splits into $H^{\bullet}$ and ${}^{\bullet}OH$ or the radicals recombine into H_2O at elevated temperature [16]; pathway ⑤ and pathway ⑥: dehydrogenation reaction of cellulose, where the H atom connects to or disconnects from oxygen and carbon atoms, respectively [124]. Due to the high activity of free radicals, the reaction pathways ④~⑥ are reversible.

Fig. 3.7(a) shows the frequency differences of forward and reverse reaction of pathway ④~⑥ in cases S2 and S5. It should be noted that the frequency of reverse reaction could be higher than that of the forward reaction, which is because the reactants involved in the reverse reaction could be produced from other reactions. For example, ${}^{\bullet}OH$ could be generated from pathway ④, while it can also be produced from the cleavage of the C-O bond in cellulose (e.g., $R\text{-}OH \rightarrow R^{\bullet} + {}^{\bullet}OH$). The cleavage of β-1,4 linkage and C-O bond in D-glucopyranose would produce $R\text{-}O^{\bullet}$ that involved in the reverse reaction of pathway ⑤. The increase in these reactant concentrations would shift the reactions into the reverse direction. The results show that the H free radicals mainly come from the dehydrogenation reaction of H atoms connected to C atoms, e.g., pathway ⑥. The H radicals generated from pathway ⑥ increase with the addition of Ni, which can be attributed to the promotion effect of Ni on C-H bond cleavage [130].

Although the water splitting reaction would produce H radicals, the ${}^{\bullet}OH$ generated from water and cellulose would consume H radicals to form water simultaneously. The frequency of pathway ④ reverse reaction is higher than that of the forward reaction, leading to an increase in water molecule number. This is due to the structural features of cellulose, which has a large number of hydroxy groups. The increase in ${}^{\bullet}OH$ concentration shifts the reaction of pathway ④ to the reverse direction, especially with the addition of Ni catalyst, since Ni could promote the scission of C-O bonds to produce more ${}^{\bullet}OH$.

Experimental results suggested that one of the roles of water in SCWG is being a source of hydrogen and free radicals [16]. However, quantitative information on such effect is difficult to obtain through experimental approaches. In ReaxFF MD simulation, the role of water in producing hydrogen and free radicals can be identified by tracing the evolution of the original water (the water that was added to the system in the initial stage). Fig. 3.7(b) indicates the total water molecule number and the source of O atom in water in cases S2 and S5. Although it was observed that the frequencies of forward and reverse reaction of pathway ④ are high, especially on Ni surface, only a small part of the original water split into H• and •OH in the end, as indicated by the red line in Fig. 3.7(b). The results indicate that only a limited number of H radicals produced from pathway ④ forward reaction could be the source of H_2 generation. Moreover, Ni could promote the splitting reaction of water, and the reduction of original water in the presence of Ni is more significant. The increased water in two cases is ascribed to the combination of H radicals and hydroxy groups dissociated from cellulose since the oxygen atom in increased water mainly comes from cellulose, as indicated by the violet line in Fig. 3.7(b). The increase of total water molecule number in Ni catalytic SCWG is more significant than in noncatalytic SCWG as Ni could promote the cleavage of C-O bond to produce more hydroxy groups. It can be deduced that water plays a limited role in providing H free radicals to produce H_2, while the hydrogen atoms in cellulose are the primary source of H_2 generation.

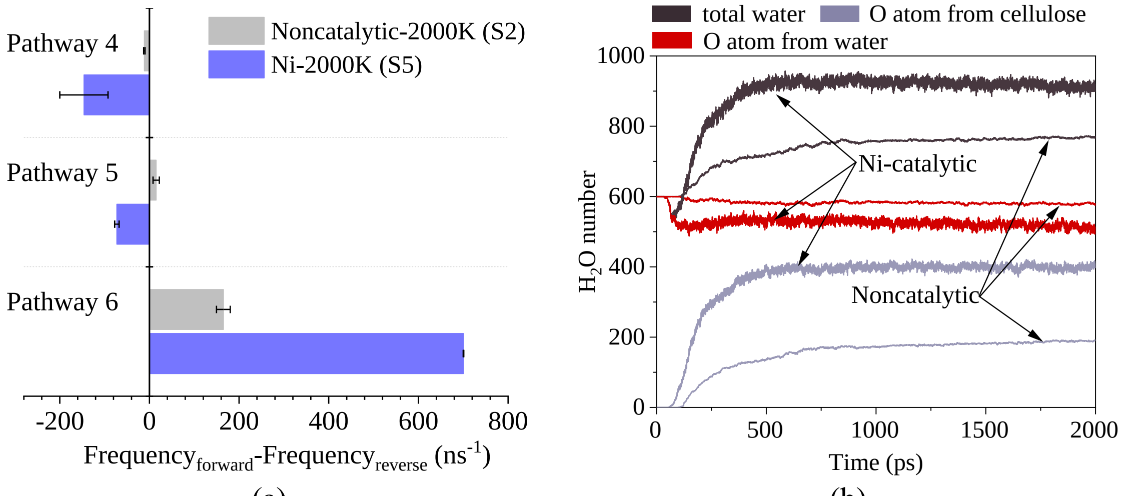

(a) (b)

Fig. 3.8 (a) The frequency difference of the forward and reverse reaction of pathways ④~⑥ in cases S2 and S5; (b) The total water molecule number and the source of O atom in water in cases S2 and S5.

A schematic diagram of H_2 generation pathways during the noncatalytic and Ni-catalytic SCWG of cellulose is shown in Fig. 3.8. In the absence of a catalyst, H free radicals would be generated via dehydrogenation of cellulose, and a small amount of water would also be split into H free radicals and •OH. H radicals generate H_2 through pathways ①~③, where pathway ① plays a leading role, followed by pathway ②. In the presence of Ni catalyst, the decomposed molecular fragments and water would be adsorbed on the Ni surface, where the scission of the C-H and O-H bonds is enhanced to produce a large number of H radicals. H radicals undergo radical termination reactions to produce H_2 (pathway ③), which dominates the H_2 generation. Meanwhile, the generated $^{\bullet}OH$ would consume H radicals to form water. In the absence of catalyst, $^{\bullet}OH$ mainly comes from pathway ②. Nevertheless, cellulose also produces some $^{\bullet}OH$ on the Ni surface via the cleavage of C-O bonds when Ni is added. The $^{\bullet}OH$ generated through serval pathways would consume a relatively large amount of H radicals, leading to an increase in H_2O molecule number. It can be found that the generation of H_2O is an H radical consumption process. The concentration of H radicals would increase if the number of $^{\bullet}OH$ in the reacting system can be suppressed, thereby increasing the yield of H_2.

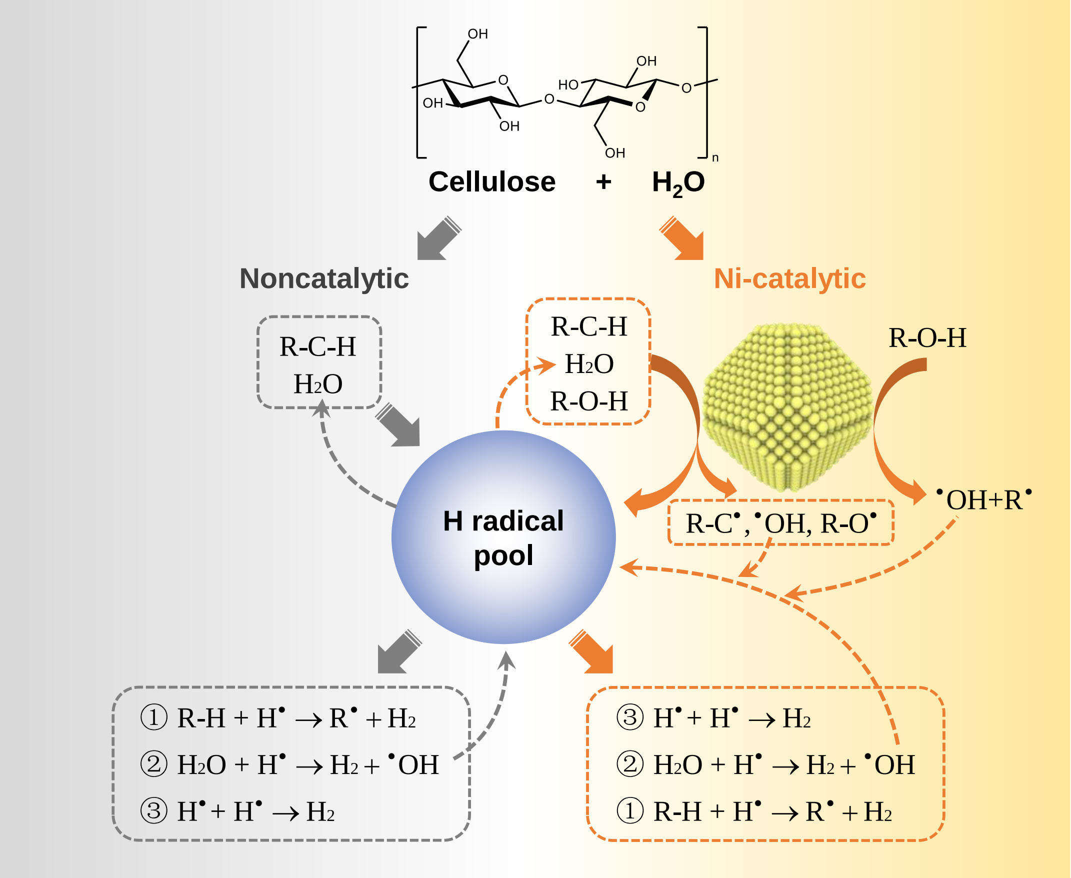

Fig. 3.9 Schematic diagram of H_2 generation pathways during noncatalytic and Ni-catalytic SCWG of cellulose.

It can be seen in Fig. 3.5 that the yield of CO is enhanced at elevated temperature in the absence of a catalyst, which is consistent with the experimental results [131]. The elevated temperature would promote the cleavage of C-C bonds, thereby enhancing the yield of gaseous products. CO yield decreased significantly when the catalyst was added. Yoshida et al. [125] attributed the reduction of CO to the enhancement of water-gas shift reaction ($CO+H_2O \rightarrow CO_2+H_2$), and the disproportionation of carbon monoxide adsorbed on the catalyst surface ($2CO \rightarrow CO_2+C$). However, this study found that the molecular fragments produced by cellulose dissociation would be adsorbed on the catalyst surface [113]. The C-O bonds would be cracked under the catalytic effect of Ni, as shown in Fig. 3.9(a). Oxygen atoms that might be used to generate CO are prone to be detached from organic fragments to produce water by interacting with H radicals. It is demonstrated that the deoxygenation and dehydroxylation of organic fragments on Ni surface are the main reason for CO reduction.

There was a slight change in the yield of CO_2 when the temperature increased, as shown in Fig. 3.5, which is ascribed to the structural features of cellulose. The carbon atom connected with two oxygen atoms is the primary source of CO_2, as illustrated in Fig. 3.9(b). There are a small number of β-1,4 linkage in cellulose; thus, the yield of CO_2 is lower than H_2 and CO [132]. Consequently, the effects of temperature and catalyst on CO_2 production are weaker than those on H_2 and CO.

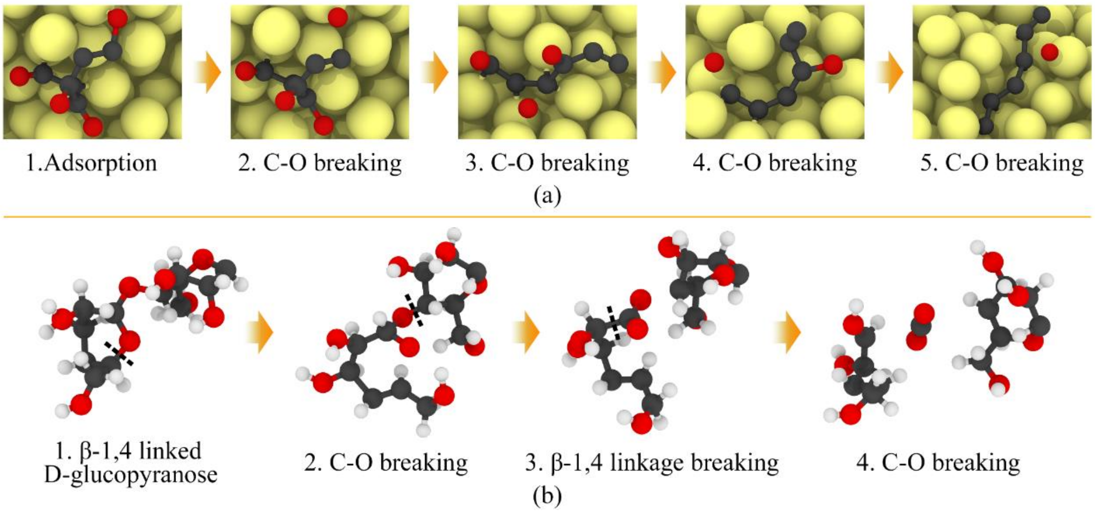

Fig. 3.10 (a) The cleavage of C-O bonds on the Ni surface; (b) The primary generation process of CO_2. Dash lines represent the bond cleavage sites.

3.2.3 The effect of C/W on gaseous product yield

Fig. 3.10 presents the yields of H_2, CO, and CO_2 under different C/W at 2000 K. The H_2 yield increases slightly with the increasing number of water molecules, which is consistent with experimental results [23]. Increasing the water molecule number favours the forward reaction of pathway ④, leading to an increase in H radical number, as shown in Fig. 3.11(a). In the presence of Ni catalyst, a large number of H radicals would be generated via water splitting and cellulose dehydrogenation reactions on the Ni surface. Then H radicals are continuously consumed to produce H_2 and H_2O. A high concentration of H radicals contributes to the formation of H_2.

Typically, water and small organic fragments would be adsorbed on metal catalyst [133], as shown in Fig. 3.11(b). It was observed that the addition of water occupies a part of the active sites on the catalyst surface, which weakens the adsorption capacity of the catalyst to organic fragments [32]. When most of the active sites of the Ni catalyst are occupied by water or hydroxyl group, the small dissociative fragments outside Ni surface will generate CO via the cleavage of C-C bonds. Therefore, the yield of CO increases with the addition of water, as shown in Fig. 3.10. The influence of C/W on CO_2 production is negligible since CO_2 mainly comes from the carbon that is connected to the two oxygen atoms, and the production of CO_2 is relatively low as stated before.

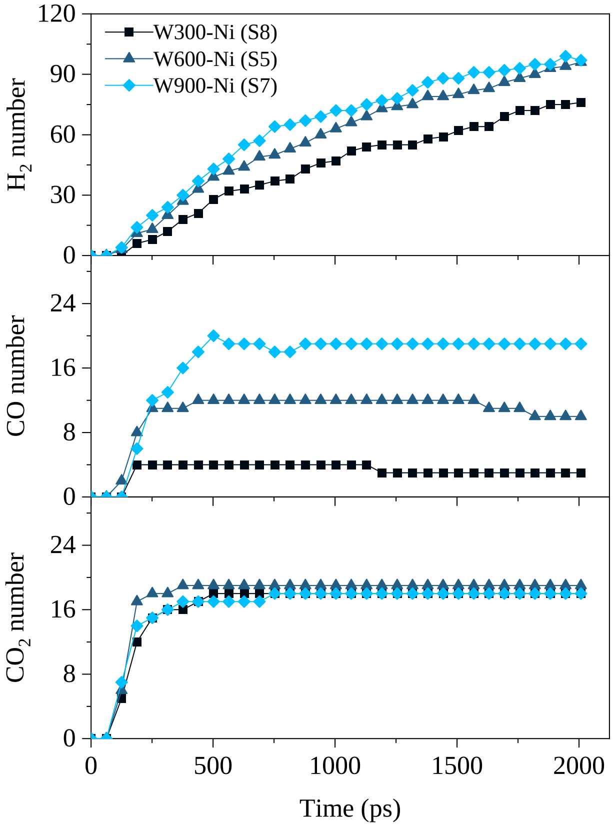

Fig. 3.11 Time evolution of H_2, CO, and CO_2 yields under different C/W conditions during Ni-catalytic SCWG of cellulose (cases S8, S5, and S7).

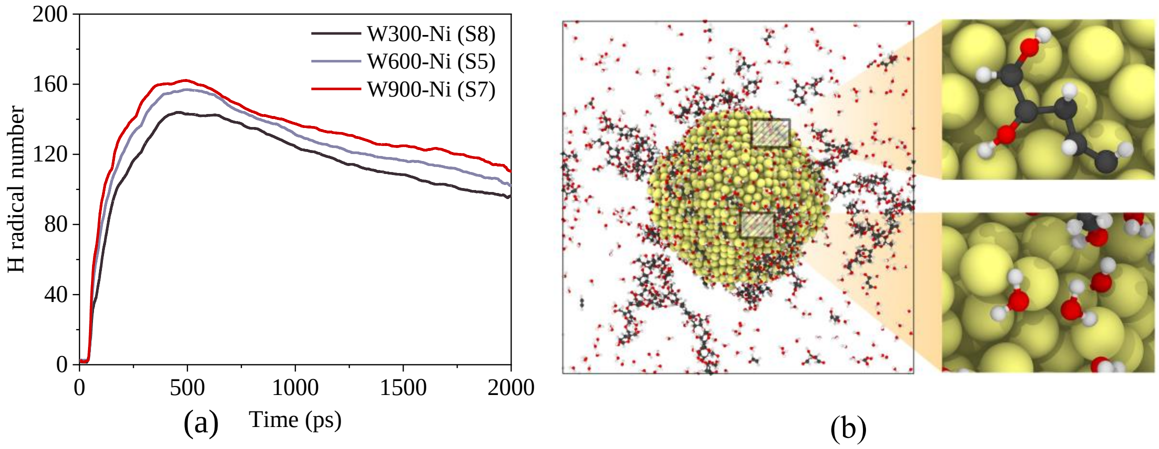

(a) (b)

Fig. 3.12 (a) Time evolution of H radical number under different C/W conditions; (b)

Snapshots of surface conditions of Ni catalyst, where the adsorption of small organic fragments and water on Ni active sites are highlighted on the right.

3.2.4 Carbon deposition on Ni catalyst

Deactivation of catalysts is unavoidable in the catalytic SCWG reaction process. Carbon/coke deposition on catalyst surface is regarded as one main problem for the deactivation of Ni-based catalysts [134]. To investigate the carbon deposition and permeation behaviour in SCWG of cellulose, the carbon deposition and permeation on Ni surface under different temperatures and C/W were analysed. The block of NiNP was divided into three zones (inside the spherical shell) according to different radii, as illustrated in Fig. 3.12(a). Carbon deposition rate is determined by the number of carbon atoms in different zones. Fig. 3.12(b) shows carbon migration on the catalytic surface and in catalyst pores. There are a small number of carbon atoms in Zone 3 at 100 ps, and then the carbon atoms permeate into the inside of NiNP at 250 ps. The evolution of carbon number in different zones under varying temperatures is presented in Fig. 3.12(d). The results show that carbon atoms infiltrate into Ni over time, and there is no noticeable difference in the total number of carbon when reaching an equilibrium state. However, the difference in the deposition rates under varying temperatures is appreciable. A small number of carbon atoms can be detected in Zone 2 at 250 ps when the temperature is 1800 K. With the increase in temperature, carbon would reach Zone 2 at an earlier time, at around 150 ps. The time instants at which carbon reaching Zone 1 at 1800 K, 2000 K, and 2200 K are around 375 ps, 180 ps, and 130 ps, respectively. The results indicate that the permeation rate of carbon increases with increasing temperature. Nevertheless, the number of carbon molecules at the equilibrium state in different zones is roughly the same, which suggests that temperature has a negligible impact on the degree of carbon permeation.

To uncover the carbon permeation mechanism on NiNP at different temperatures, the atomic order of Ni atoms was analysed. Steinhardt's bond orientational order parameters Q_l (where l can take an integer value between 0 and infinity) [135] were used to explore the local atomic environment. These order parameters are mathematically defined based on certain rotationally invariant combinations of spherical harmonics calculated between atoms and their nearest neighbours, providing information about local atom environments. Q_l has been used for various purposes, such as the structure identification of solid and liquid systems [136]. Commonly Q_6 is used in the identification of cubic lattice structure. All the particles in a perfect ordered structure have the same value of Q_6. As a results, Q_6 values can be used to determine whether an ordered structure is beginning to turn into a disordered structure. Therefore, Q_6 was adopted to characterise the atomic order of NiNP, which was built as a face-centred cubic lattice structure in this study. The magnitude of Q_6 is large when the Ni atoms are ordered and small when the Ni atoms are disordered.

Fig. 3.12(c) shows the sectional view of NiNP atomic Q_6 values at different times. The internal atoms of NiNP are in an ordered state in the initial stage and then in transition to a disordered state over time. The evolution of averaged atomic Q_6 of Ni atoms in different zones is presented in Fig. 3.12(e). The equilibrium Q_6 values decrease with increasing temperature. The position of atoms in the outermost shell (e.g., Zone 3) shifted first, and then the order degree of internal atoms decreased over time as heat was transferred to the interior region. The Q_6 values in Zone 2 and Zone 1 decreased more slowly under lower temperatures. For example, the Q_6 value in Zone 1 at 2200 K decreases significantly at around 125 ps, while the time instant for Q_6 dramatical reduction at 1800 K is about 310 ps. The decrease in Q_6 value represents that the crystal structure of NiNP is destroyed, and there is a relatively large displacement between Ni atoms. It is easier for carbon atoms to infiltrate into the NiNP when the displacement between Ni atoms becomes larger.

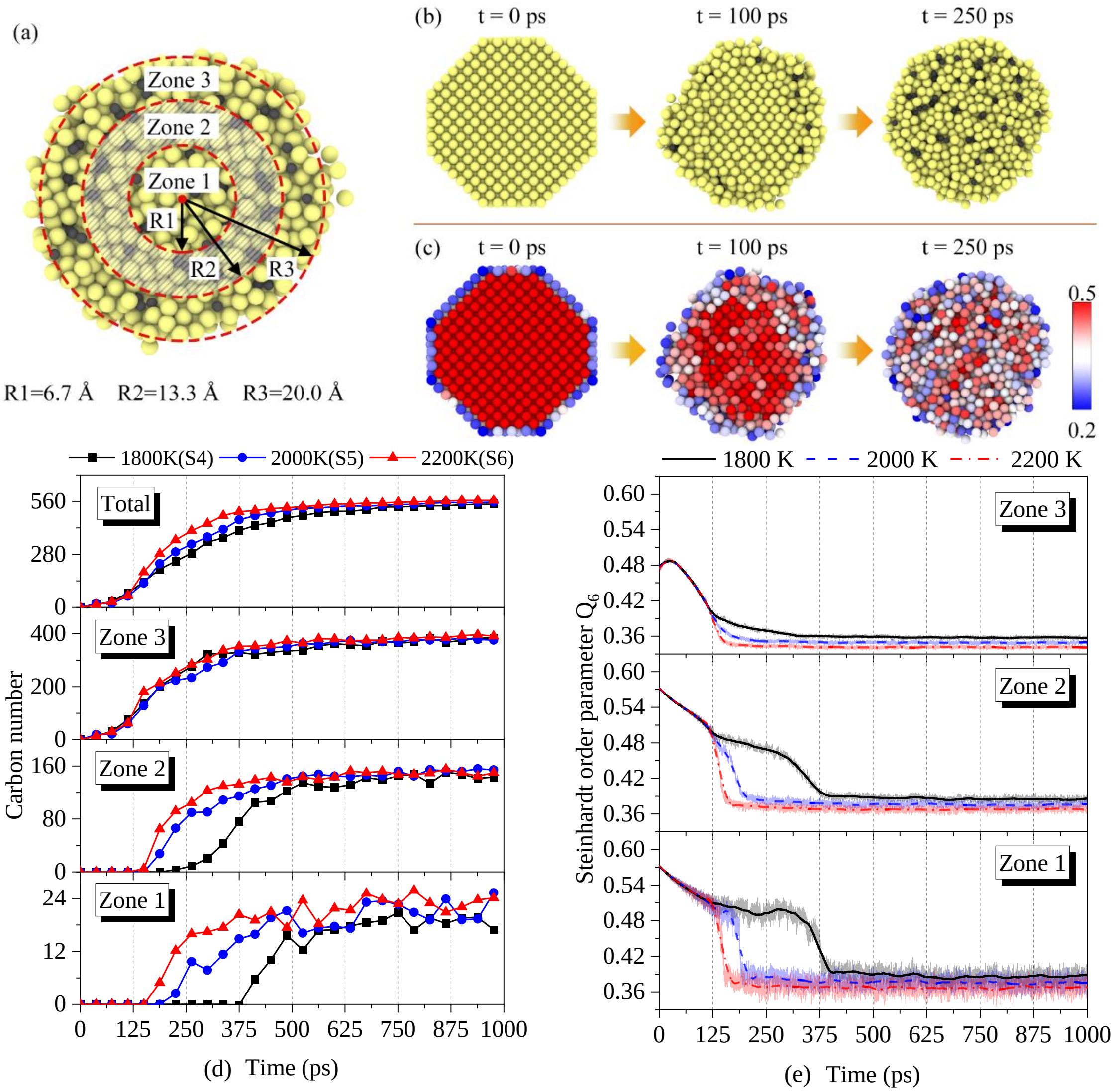

Fig. 3.13 (a) The division method of NiNP in different zones; (b) The sectional view of the carbon migration process in NiNP; (c) The sectional view of atomic Q_6 values of NiNP; (d) The evolution of carbon number in different zones under varying temperatures; (e) The

evolution of averaged atomic Q_6 values in different zones.

Fig. 3.13 shows the evolution of carbon numbers in different zones under varying C/W. The time that carbon reaches Zone 2 and Zone 1 is roughly the same under different C/W conditions, demonstrating that C/W has a negligible influence on carbon permeation on NiNP surface and in NiNP pores. Nevertheless, high C/W would inhibit the carbon deposition number on NiNP. The equilibrium carbon numbers in total and in different zones decrease with the increase in water molecule number. Wu and Liu [134] also reported that the increase of the steam to carbon ratio could favour carbon elimination during bio-oil gasification. The carbon elimination from the catalyst surface can be ascribed to the addition of water occupying the active sites on the catalyst surface, preventing the dissociative carbon atoms from attaching to NiNP.

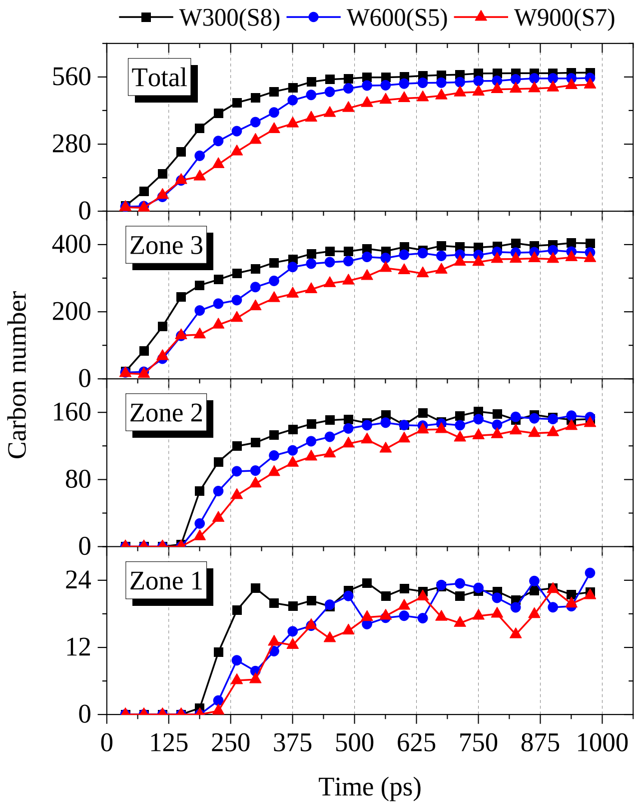

Fig. 3.14 The evolution of carbon number in different zones under varying C/W.

3.3 Conclusions

In this Chapter, Ni catalysed gasification of cellulose in supercritical water is investigated by using reactive MD simulation. The depolymerisation and ring-opening process of cellulose, effects of Ni and C/W on gaseous product yield, and carbon deposition behaviour on Ni catalyst were investigated. This study provides detailed information on Ni-catalysed cellulose SCWG at an atomic level.

Calculated activation energies show that Ni can decrease the activation energy of C-C and C-O bond cleavage, promoting cellulose depolymerisation and ring-opening process. Cellulose could be gasified at a lower temperature with the addition of Ni. The activation energy reduction of C-O is more significant than that of C-C bonds under the effect of Ni.

The H_2, CO, and CO_2 yields increase with increasing temperature. H_2 yield increases significantly in the presence of Ni due to the large number of hydrogen free radicals generated by the cleavage of C-H and O-H bonds on the surface of NiNP. H radicals can not only interact with each other to produce H_2 but also interact with H atoms on water and cellulose to generate H_2. The •OH generated would consume H radicals, leading to an increase in H_2O number. The concentration of H radicals would increase if the number of •OH in the reacting system can be suppressed, thereby increasing the yield of H_2. Simulation results show that water plays a limited role in providing H free radicals to produce H_2, the hydrogen atoms in cellulose are the primary source of H_2 generation. The cellulose cracking fragments would be adsorbed on the NiNP surface, where these fragments undergo deoxygenation and dehydroxylation reactions, leading to a reduction of CO and CO_2 yields. The addition of water will occupy the active sites on Ni surface, reducing the probability of molecular fragments attaching to the Ni surface. The small dissociative fragments outside Ni surface tend to generate more CO.

The carbon deposition on the NiNP surface results in the deactivation of the catalyst. Due to the movement of Ni atoms at high temperature, the adsorbed carbon would infiltrate into the NiNP. Results suggest that carbon permeation rate increases with increasing temperature as the relative displacement of Ni atoms would be increased under higher temperatures. The increase in water mass fraction can favour carbon elimination from the catalyst surface because water would occupy the active sites on the NiNP surface, resulting in the failure of carbon adsorption. This study elucidated the detailed mechanism of Ni-catalysed cellulose SCWG from the molecular point of view, providing a basis for further biomass utilisation and cost reduction.

Chapter 4

Nitrogen Transformation in Coal/Ammonia Co-Pyrolysis

Coal and ammonia (NH_3) co-firing technology is a promising solution allowing the retrofitting of coal power and contributing to global decarbonisation goals. However, using NH_3 for power generation still presents some knowledge gaps. In this Chapter, the impact of NH_3 on coal pyrolysis rate was investigated. The decomposition of NH_3 was revealed by using ReaxFF force field in Section 4.2.2. The nitrogen transformation process and the morphological evolution of the nitrogen functionalities in char and tar was presented in Section 4.2.3 and Section 4.2.4, respectively.

4.1 Experiment and MD modelling methodology

4.1.1 Experiment

Sub-bituminous coal was selected as raw material to study the impact of NH_3 on coal pyrolysis. A self-designed TG analysis was employed to gain the weight loss of coal under different atmospheres and temperatures. TG analysis is a technique used to study the thermal stability and composition of a material by measuring the change in its weight as a function of temperature or time under controlled temperature and atmosphere conditions. The experimental temperature was set ranging from 800 °C to 1000 °C. The coal pyrolysis was conducted under high-purity Ar and Ar/NH_3 (20% NH_3 + 80% Ar) atmospheres at each temperature. The schematic diagram of the experiment is shown in Fig. 4.1. The specific experimental process was presented in Ref. [137].

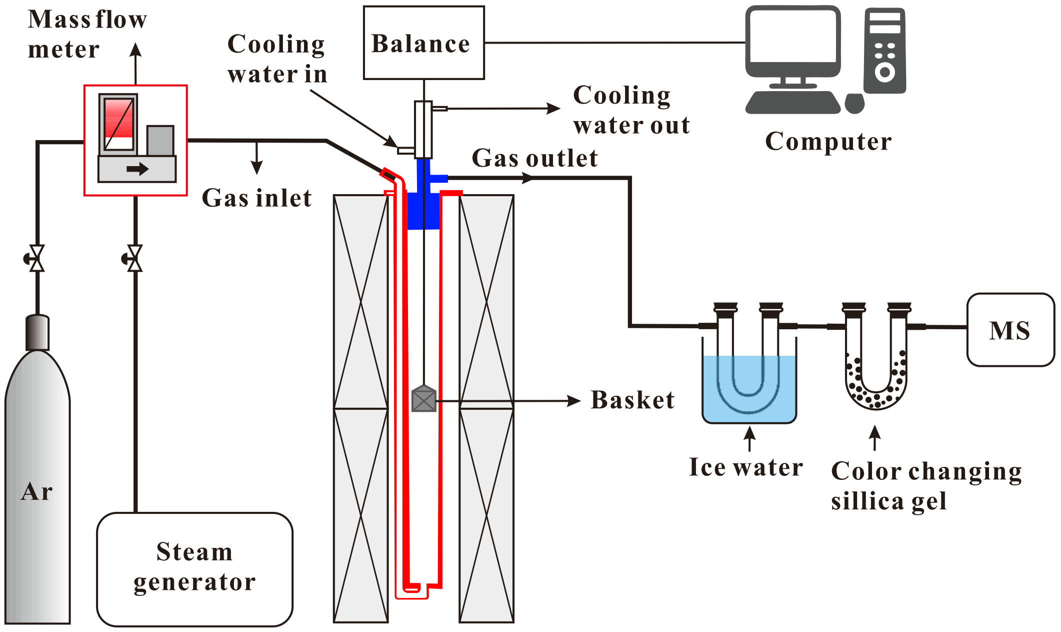

Fig. 4.1 The schematic diagram of the experiment [137].

4.1.2 Model construction

Coal is a cross-linked macromolecular structure comprising polycyclic aromatics with covalent linkages. The coal model ($C_{227}H_{189}O_{36}N_5$) developed by Liang et al. [138] was adapted for the MD simulations in this work. It has been used to investigate the nitrogen transfer mechanism in the oxidation and hydropyrolysis of coal [63, 139]. The coal model is presented in Fig. 4.2(a). N atoms exist as hydroxylamine, amide, N5, and N6 in this coal model, as shown in Fig. 4.2(b). Eight reaction systems S1~S8 were built to investigate the impact of NH_3 on coal pyrolysis and nitrogen transformation during co-pyrolysis, as listed in Table 4.1. A total of 20 coal molecules, consisting of 9140 atoms, were introduced into the simulation box. This number of atoms is higher than what is typically used for studying coal pyrolysis or oxidation [63, 139, 140]. Wang et al. [49] recommended using 20~30 wt% NH_3 during NH_3/coal co-firing, taking into account both economic considerations and the need to control NO emissions. However, due to computational cost limitations and the negligible impact of reducing NH_3 on the study of N atom migration mechanism. The NH_3 mass fraction was reduced to 16%, and 800 NH_3 molecules were added to the co-pyrolysis system in this study. The mass ratio of NH_3 addition was fixed since this study focuses on the interaction between NH_3 and coal. The pyrolysis of NH_3 was tested under different temperatures. It was found that the pyrolysis of NH_3 was too slow to be observed when the temperature was under 2200 K. The temperature was set between 2200 K and 2800 K with an interval of 200 K. It should be noted that all the ReaxFF MD simulations were performed at higher temperatures than laboratory experiments, allowing chemical reactions to occur within an acceptable computational time [116]. Salmon et al. [118] studied coal pyrolysis using ReaxFF simulation at an elevated temperature. They compared the simulated product distribution with experimental results and concluded that elevated temperature did not influence the reaction pathways during coal pyrolysis. Accordingly, elevated reaction temperatures were chosen in this work to study the coal/NH_3 co-pyrolysis. Using high temperatures to speed up chemical reactions (so that reactions can take place within the affordable simulation time) is a common strategy in ReaxFF MD simulations. The value of ReaxFF MD simulations is to reveal the pathways of chemical reactions based on the detailed information at the atomic level.

Table 4.1 Detailed simulation cases for the studied systems of coal/NH_3 co-pyrolysis

Cases	Coal molecules	NH_3 molecules	Temperature
S1	20	-	2200 K
S2	20	-	2400 K
S3	20	-	2600 K
S4	20	-	2800 K
S5	20	800	2200 K
S6	20	800	2400 K
S7	20	800	2600 K
S8	20	800	2800 K

4.1.3 Simulation setup procedures and details

All MD simulations in this work were conducted using the ReaxFF force field [111]. The parameters of ReaxFF force field used were developed by Kowalik et al. [141], which was adopted to study the impact of NH_3 addition on the formation of soot [61] and the pyrolysis/combustion of nitrogen-containing fuels [142]. The effects of NH_3 addition on the concentration of PAHs evaluated from MD simulation results were consistent with the laser-induced fluorescence (LIF) findings, which confirms the effectiveness of the force field in simulating the combustion of NH_3 and organic compounds [61]. Initial configurations of all models were built by using the Packmol programme [119]. Coal and NH_3 were distributed randomly into the cubic box with a dimension of 112×112×112 Å, as shown in Fig. 4.2(c) and Fig. 4.2(d). After system energy minimisation, the simulation cell was relaxed at 300 K for 20 ps. Subsequently, the equilibrated system was heated to the final reaction temperature with a heating rate of 30 K/ps. Then, the simulations would last at the target temperature for 2 ns. All simulations were performed using an NVT ensemble. A time step of 0.1 fs was assigned. The trajectories and species information were outputted every 100 steps.

The periodic boundary condition was applied in all directions. The initial velocities for all atoms were generated randomly following the Maxwell-Boltzmann distribution. The system temperature and pressure were controlled by using Nosé-Hoover thermostat and barostat [143]. A bond order of 0.3 was employed to identify chemical bonds between pairs of atoms [112, 113]. All simulations were repeated three times with different initial configurations and velocity distributions. The ReaxFF MD simulations were performed with the REAXC package [120] in the Large-scale Atomic/Molecular Massively Parallel Simulation (LAMMPS) [121].

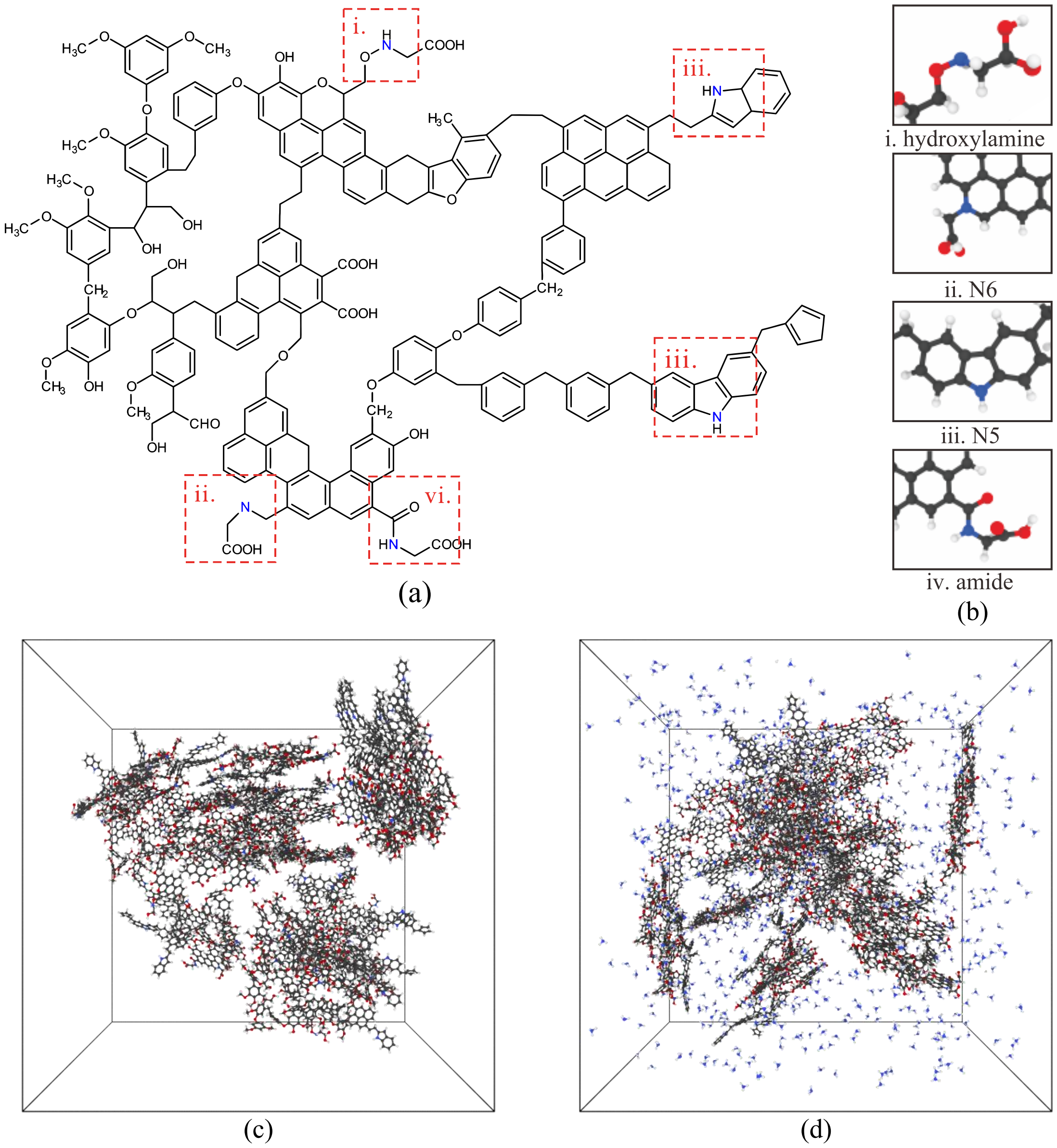

Fig. 4.2 (a) Structural formula of coal model ($C_{227}H_{189}O_{36}N_{5}$); (b) different forms of N in coal; (c)~(d) snapshots of coal-only pyrolysis and coal/NH_3 co-pyrolysis MD model.

4.2 Results and discussion

4.2.1 The impact of NH_3 on coal pyrolysis

The TG experiment was carried out to study the impact of NH_3 on coal pyrolysis. The weight loss of coal under different atmospheres and temperatures is presented in Fig. 4.3(a). It can be seen that there are two stages during coal pyrolysis, i.e., fast pyrolysis (devolatilisation stage, around 0~250 s) and slow pyrolysis (around 250~1000 s) stages. At the fast pyrolysis stage, the heating causes chemical bonds to rupture. The organic and inorganic compounds decompose to form volatile products, resulting in a sharp decrease in coal weight. During this stage, the weight loss rate of coal sample increases with increasing temperature, and NH_3 has a negligible effect on coal pyrolysis rate. At the slow pyrolysis stage, the weight loss rate of coal decreased, and the impact of NH_3 on coal pyrolysis was more significant, especially under high temperatures. For example, there is a considerable difference between the weight loss of coal sample at NH_3 (blue solid line) and at Ar (blue dash line) atmosphere under 1000 °C after 250 s. The experimental results indicated that the addition of NH_3 could accelerate coal pyrolysis. MD simulation was carried out to study the mechanism behind this phenomenon.

In MD simulation, the pyrolysis productions can be classified into three categories based on the number of carbon atoms in products: gas (molecules containing less than 4 carbon atoms and inorganic molecules such as H_2O, N_2, H_2 etc.), tar (molecules containing 4~39 carbon atoms), and char (molecules containing more than 39 carbon atoms) [139]. Since the weight loss of coal is dominated by the release of volatile hydrocarbons. In MD simulation, the carbon number distributed in tar and char ($C_{tar/char}$) products was used to evaluate the impact of NH_3 on coal pyrolysis. $C_{tar/char}$ is computed by the following equation:

$$C_{tar/char} = \frac{\text{carbon number in tar and char species}}{\text{total carbon number}} \times 100\% \tag{4.1}$$

As indicated in Fig. 4.3 , the simulation temperatures are obviously higher than the experimental temperatures, while the MD simulation time scale is smaller than the TG experiment time scale by 12 orders of magnitude. A similar trend in $C_{tar/char}$ was found in the MD simulation results compared with experimental TG results, as shown in Fig. 4.3(b). This similarity also demonstrates that MD can effectively simulate the changes in pyrolysis products during co-pyrolysis of coal and NH_3. It may be difficult to make direct comparisons of experimental and simulation results. However, experimental measurements and MD simulations are complementary approaches that can be used together to gain a more complete understanding of nitrogen transformation in coal/ammonia co-pyrolysis. Although there might be a mapping between the parameters in ReaxFF simulations and those in pyrolysis tests, the exact correspondence needs to be further investigated. Fig. 4.3 shows that the pyrolysis process would have some similarities when the chemical reactions are triggered, whether the conditions correspond to the real experimental environments or those values associated with the “temperature-accelerated reaction kinetics” in the ReaxFF MD simulations.

In Fig. 4.3(b), a quick release of volatile hydrocarbons can be found before 500 ps (fast pyrolysis stage), followed by a slow pyrolysis stage (500~2000 ps). The impact of NH_3 on $C_{tar/char}$ during fast pyrolysis is small, and this impact becomes obvious at the following stage. Meanwhile, the $C_{tar/char}$ gap between coal-only pyrolysis and coal/NH_3 co-pyrolysis increases with increasing temperature. For example, at a temperature of 2200 K, the final value of $C_{tar/char}$ (at 2 ns) for coal-only pyrolysis and coal/NH_3 co-pyrolysis is 87.6% and 85.9%, respectively, representing a difference of 1.7%. While this gap increases to 5.1% under 2800 K. It should be noted that the conditions in TG experiment and MD simulation are different, so it is inappropriate to compare the experiment and MD results directly. However, the complementary results obtained by these two methods could help to gain an in-depth understanding of the problem at both the atomic and macroscopic scales. The consistent results indicate that MD simulation is a promising approach for investigating NH_3/coal co-pyrolysis.

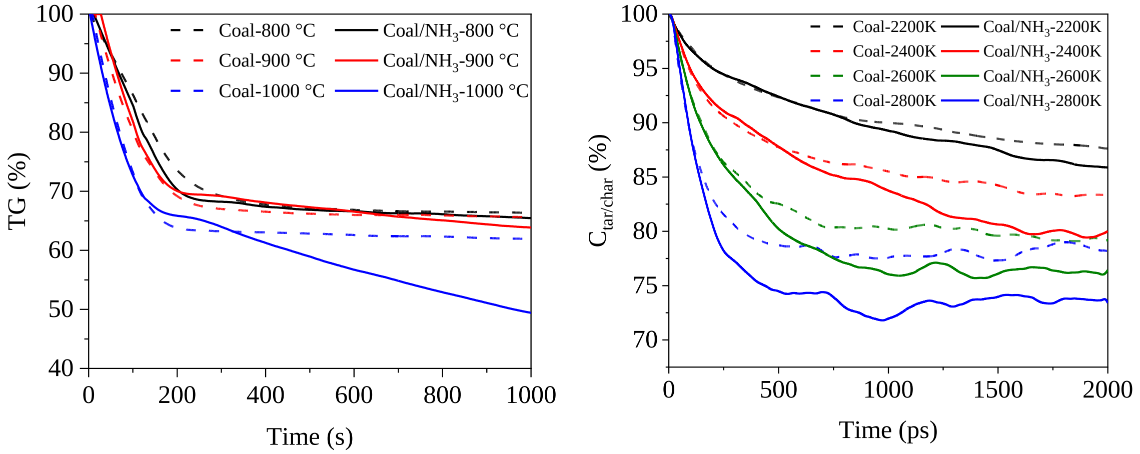

(a) (b)

Fig. 4.3 (a) The TG experiments of coal-only pyrolysis and coal/NH_3 co-pyrolysis; (b) MD simulation results of the proportion of carbon distributed in tar and char species at different temperatures.

It was reported that the addition of NH_3 could inhibit soot formation by constraining PAHs growth [61]. In order to reveal the influence of NH_3 on PAHs growth. The primary intermediates and products that contain 1~3 carbon atoms in coal-only and coal/NH_3 co-pyrolysis under 2800 K were obtained, as presented in Fig. 4.3. The numbers of PAH precursors (such as CH_3, CH_2O, C_2H_2) increase rapidly at the fast pyrolysis stage, and then decrease gradually. PAH precursors have high reactivity, which makes them tend to combine with other fragments to form tar or char. Nevertheless, these PAH precursors would react with NH_3 decomposition products to form carbon-nitrogen species when NH_3 is added, leading to a decrease in the number of PAH precursors during the fast pyrolysis stage, as presented in Fig. 4.3(a). The time evolution of primary carbon-nitrogen species is shown in Fig. 4.3(b). A larger number of C atoms would be captured by N atoms to form HCN and other carbon-nitrogen species. Their number remains stable after 500 ps because these carbon-nitrogen species are less reactive in the subsequent formation of tar and char. It can be deduced that the gap in weight loss rate between coal-only pyrolysis and coal/NH_3 co-pyrolysis is due to the reaction between PAH precursors and NH_3 decomposition, leading to a generation of relevant stable carbon-nitrogen species. Moreover, the concentration of NH_3 decomposition products increases with increasing temperature (discussed in Section 3.2), which consumes more PAH precursors. Thereby, the impact of NH_3 on weight loss in Fig. 4.2 becomes more significant under higher temperatures.

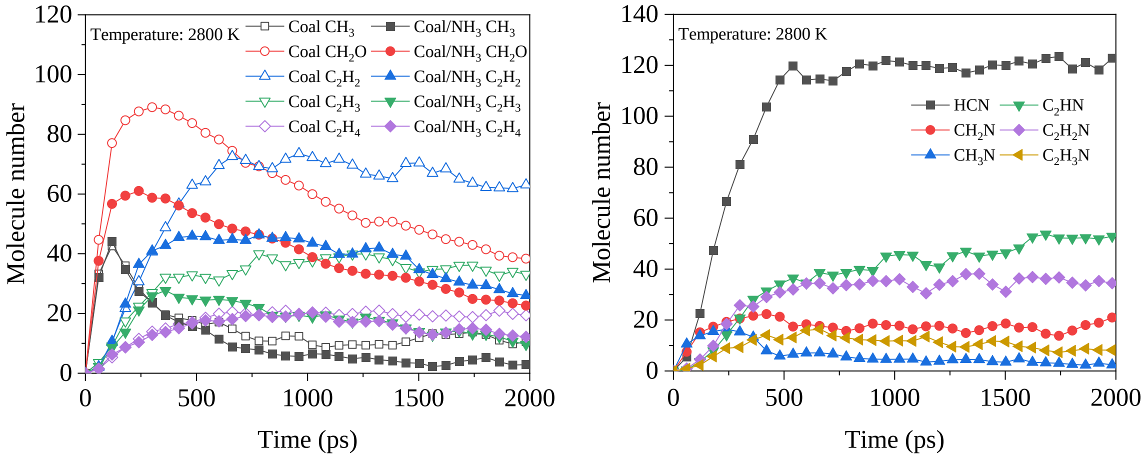

(a) (b)

Fig. 4.4 Time evolutions of major (a) N-free PAH precursors in coal-only pyrolysis and coal/NH_3 co-pyrolysis and (b) carbon-nitrogen gaseous species in coal/NH_3 co-pyrolysis under 2800K.

4.2.2 The decomposition of NH_3

The transformation of N from NH_3 to coal decomposition products can be divided into three steps: (1) the decomposition of NH_3 to form highly reactive radicals; (2) the reaction between NH_3 (include relevant radicals) and coal decomposition fragments (hereinafter called coal fragments), in which N migrate into coal fragments; and (3) the evolution of N structure in coal fragments, i.e., the formation of stable N-functionalities.

Before studying the reactions between NH_3 and coal, the decomposition of NH_3 under different temperatures needs to be investigated. Under high temperatures, NH_3 would split into amino radical ($NH_2^{\bullet}$) and azanylidene ($NH^{2\bullet}$) [144], which are highly reactive and consequently short-lived. The reactions involving the conversion of NH_3, $NH_2^{\bullet}$, and $NH^{2\bullet}$ are listed in Fig. 4.4. R1~R5 are reactions that involve the conversion between NH_3 and $NH_2^{\bullet}$; R6~R9 are reactions that involve the conversion between $NH_2^{\bullet}$ and $NH^{2\bullet}$; R10 is the reaction of NH_3 and $NH^{2\bullet}$ conversion. The reactions are reversible as the radicals are highly reactive. Since nitrogen (N_2) hardly reacts with other molecules, the reactions that involve the generation of N_2 have not been discussed here.

The forward and reverse reaction frequencies of R1~R10 under different temperatures are presented in Fig. 4.5. It can be seen that most of NH_3 would be converted into $NH_2^{\bullet}$ via reaction R2, which has the highest frequency among them. Most of the reactions have a positive frequency, which means NH_3 and $NH_2^{\bullet}$ tend to be converted into $NH_2^{\bullet}$ and $NH^{2\bullet}$ by losing one hydrogen atom. This result indicates that NH_3 is a hydrogen provider during co-pyrolysis. In addition, the frequency of R1, R2, R3, and R7 increases with increasing temperature because NH_3 would become more reactive under high temperatures. Coal would be gasified to produce $H^\bullet$ by dehydrogenation reaction under high temperatures [145], which is the main reason that R5 proceeds towards the reverse direction when temperature increases. The increase of $H^\bullet$ concentration enables reactions R2 and R7 to proceed forward. The number of $H^\bullet$ generated from coal dehydrogenation is significantly influenced by the reaction environment (e.g., temperature, pressure, catalyst etc.). Therefore, it can be deduced that the concentration of $NH_2^\bullet$ during coal/NH_3 co-pyrolysis would increase if coal could provide more $H^\bullet$ radicals.

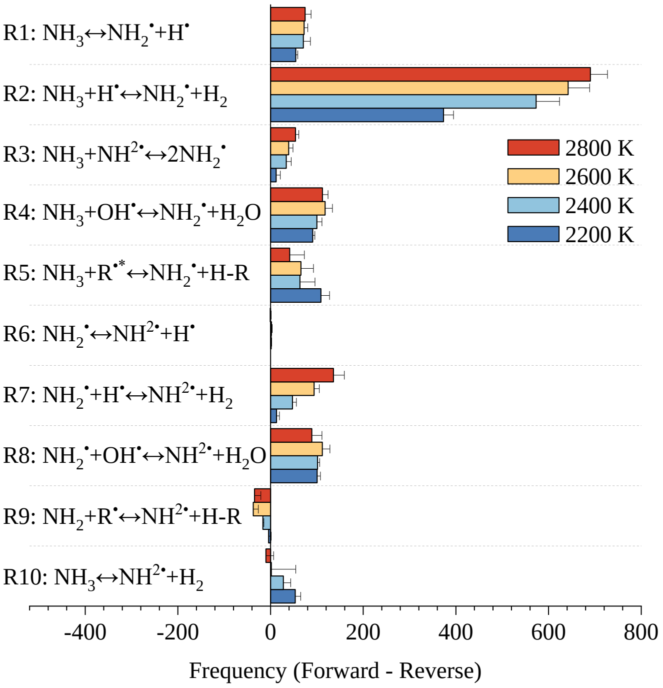

Fig. 4.5 The frequency of reactions R1~R10 under different temperatures (*R group: An abbreviation for any group that contains carbon atom).

4.2.3 The reaction between NH_3 and coal decomposition product

In addition to NH_3, there are two other NH_3 decomposition radicals in the system, namely $NH_2^\bullet$ and $NH^{2\bullet}$. Which type of radicals are prone to combining with coal fragments and the detailed transfer mechanism is still unknown. To uncover the mechanism of N migration and transformation, the reactions between NH_3 and coal were investigated. The frequency of reactions between NH_3, $NH_2^\bullet$, $NH^{2\bullet}$ radicals with carbon, oxygen, and nitrogen atoms in coal fragments under 2800 K is presented in Fig. 4.5. It can be seen that the reaction between $NH_2^\bullet$ and C (N-C) is the primary path for N transformation, which has the highest frequency. Part of NH_3 molecules would connect to the C atom directly and then undergo a dehydrogenation reaction to form H_2 and amine (R-N). The frequency of reaction between $NH^{2\bullet}$ and C atom is low. This is because the reactivity of $NH^{2\bullet}$ is too high, leading to a relatively low concentration of $NH^{2\bullet}$. Only a small part of $NH^{2\bullet}$, $NH_2^\bullet$, and NH_3 would react with O atom to form the N-O bond because oxygen usually exists in the form of hydroxyl, and the mass fraction of oxygen is lower than carbon in coal. The frequency of reactions between NH_3, $NH_2^{\bullet}$, $NH^{2\bullet}$ and carbon under different temperatures was analysed, as shown in Fig. 4.5(b). More N atoms would be attached to coal fragments in the form of $NH^{2\bullet}$ and $NH_2^{\bullet}$ with increasing temperature, which is primarily ascribed to the increasing concentration of $NH^{2\bullet}$ and $NH_2^{\bullet}$ under high temperatures. Besides, it was observed that N_2 seldom react with coal fragments due to its chemical stability. The NO_x emission might decrease if more N atoms could evolve into N_2.

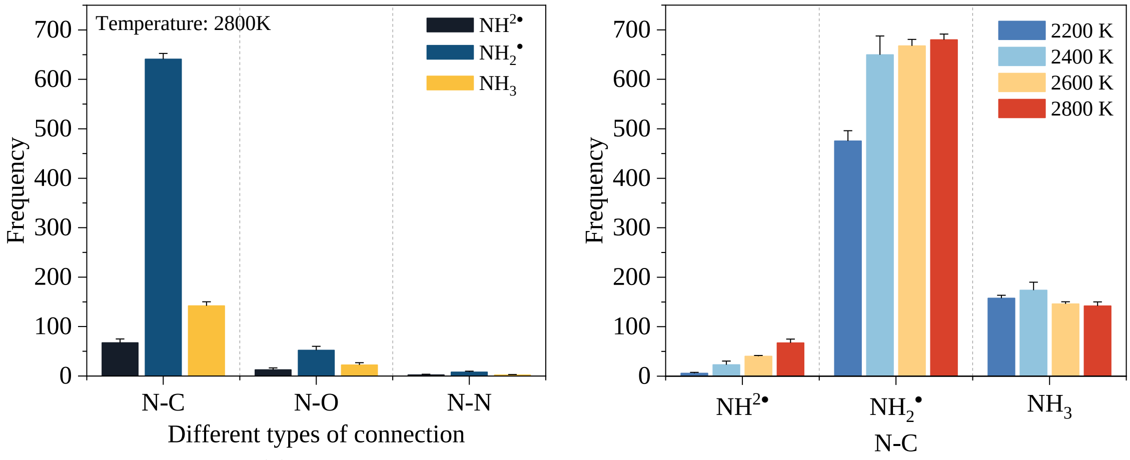

(a) (b)

Fig. 4.6 (a) The frequency of reactions between NH_3, $NH_2^{\bullet}$, $NH^{2\bullet}$ with carbon, oxygen, and nitrogen atoms in coal fragments under 2800 K. The reactions are represented as N-C, N-O, and N-N, respectively; (b) The frequency of reactions between NH_3, $NH_2^{\bullet}$, $NH^{2\bullet}$ with carbon under different temperatures.

The C atom in coal fragments can be divided into three types based on its position: (1) C atom located at the end of the carbon chain (C_{end}); (2) C atom located in the middle of the carbon chain (C_{middle}); and (3) C atom located in the aromatic ring (C_{ring}). NH_3 and its decomposition products could be connected to any of these C atoms. Since the connection position of N atoms would have an impact on the structural evolution of the N-functionalities in subsequent reactions (discussed in Section 3.4). The reactions between NH_3 and different types of C atom was studied quantitatively. The migration of N atoms from NH_3 to coal fragments could be realised by the three pathways presented in Fig. 4.7. In addition, the frequencies of pathways 1~3 under different temperatures were analysed, as shown in Fig. 4.8. Pathways 1~3 represent NH_3 and its decomposition products connected to the C atom at the end of carbon chain, in the middle of carbon chain, and in aromatic ring, respectively. It can be seen that pathway 3 has the highest proportion among them, especially under relatively low temperatures. This is because around 80% of coal atoms existed in the form of aromatic C before pyrolysis. More aromatic rings would be opened when temperature increases, which makes the frequencies of pathways 1 and 2 increase and pathway 3 decreases accordingly. The frequency of pathway 1 is higher than that of pathway 2, while the number of C_{end} is smaller than that of C_{middle}. The results indicate that compared with C_{middle}, NH_3 and its composition products tend to connect to the C_{end} in coal fragments.

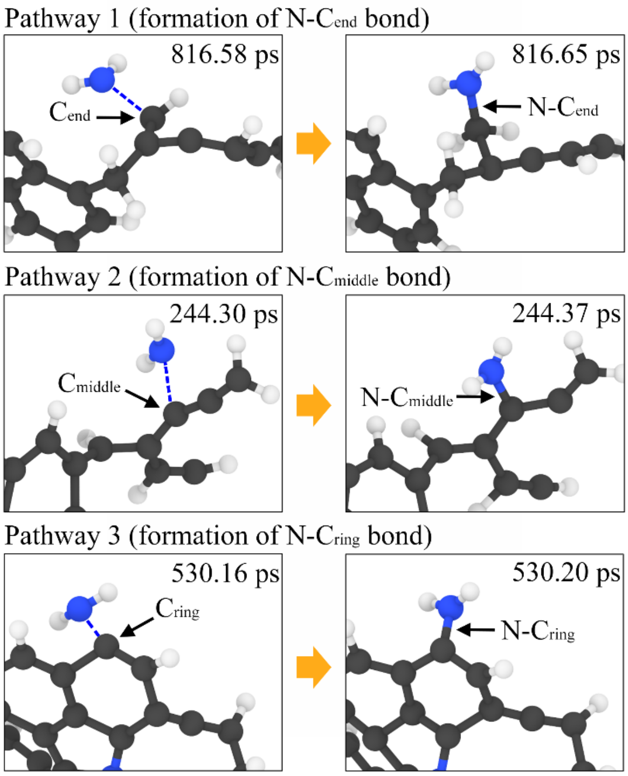

Fig. 4.7 Examples of $NH_2^{\bullet}$ connected to different types of C atom under 2400 K. Pathway 1: $NH_2^{\bullet}$ connected to C_{end}; Pathway 2: $NH_2^{\bullet}$ connect to C_{middle}; and Pathway 3: $NH_2^{\bullet}$ connected to C_{ring}. (Blue dash lines represent the N-C bond that would be formed in the following steps).

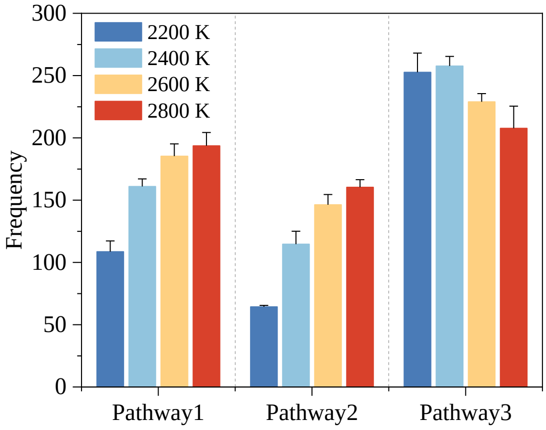

Fig. 4.8 The frequency of pathways 1~3 under different temperatures.

It was reported that the hydrogen content has an influence on the reactivity and growth of PAHs. Radical sites on coal fragments, depending on the C-H bond types, temperature and concentration of hydrogen-abstracting radicals (H, OH, O radicals) in the pyrolysis environment, have been considered responsible for the reactivity of coal decomposition fragments [146]. The number of radical sites on coal fragments can be evaluated by the number of H atom connections. The number of H atoms connected to C atom in the occurrence of N-C bond formation was analysed, as presented in Fig. 4.8. C(0H), C(1H), and C(2H) represent C connected with zero, one, and two hydrogen atoms when NH_3 or its decomposition product is attached to C atom, respectively. The frequency of different types of N-C bond formation in Fig. 4.8 is affected by the cleavage of C-C and C-H bonds (dehydrogenation reaction). The former would promote the generation of C_{end} and C_{middle} via a ring-opening reaction. Both cleavages would provide more reactive sites, so that NH_3 decomposition products would be more likely to react with coal fragments. The frequency of N-C(1H) formation in pathway 1 and N-C(0H) formation in pathway 2 increase with increasing temperature due to the promoted cleavage of C-C and C-H. The frequency of N-C(2H) in pathway 1 and N-C(1H) in pathway 2 should have increased with the increasing number of C_{end} and C_{middle}, but it showed an opposite trend, as presented in Fig. 4.8(a) and (b). This result indicates that the dehydrogenation reaction plays a significant role in promoting the formation of N-C bond. The ring-opening process causes the reduction of C_{ring}. Under the combined effect of ring-opening and dehydrogenation reaction, the frequency of N-C(0H) formation in pathway 3 (Fig. 4.8(c)) decreased slightly. Overall, it can be deduced that the cleavage of C-C bond and C-H bond caused by high temperature would generate more reactive sites in C atoms, resulting in more NH_3 decomposition products connected to coal fragments.

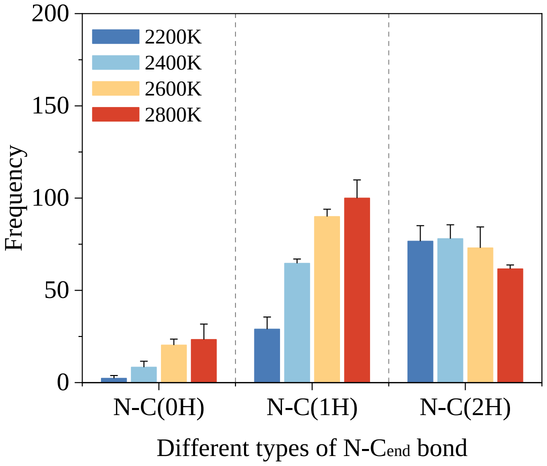

(a)

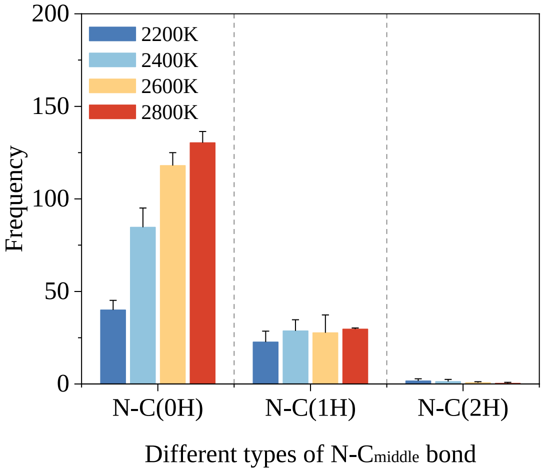

(b)

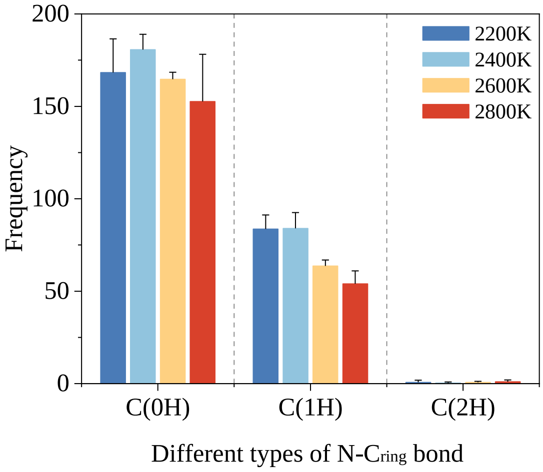

(c)

Fig. 4.9 (a)~(c) Statistics of the formation of different types of N-C bonds in pathways 1~3. C(0H), C(1H), and C(2H) represent C connected with zero, one, and two H atoms when NH_3 or its decomposition product is attached to C atom, respectively.

4.2.4 The morphological evolution of the N-functionalities

After NH_3 and its decomposition products attached to coal fragments, the N-functionalities would evolve to form relatively stable N5 and N6 groups eventually. A schematic representation for the formation of the N5 and N6 group is provided in Fig. 4.9. When NH_3 and its decomposition products attached to coal fragments, N atoms could connect to the side chain to form N6 group directly (pathway 4). Meanwhile, the N-containing side chains could be linked to form a large ring (pathway 5, a large N-containing ring represents the carbon number in this ring greater than 7). Then the condensation of the large ring started through the internal cross-linking or the bridged bond formation at the radical sites, resulting in the formation of a smaller N-containing ring. After that, the small ring finally evolves into N5 or N6 by forming internal bonds (pathway 7). It should be noted that these four reaction types are not necessary for all the N5 or N6 group formation. For example, the 7-membered N-containing heterocycle (N7) group could be initiated by linking side chains (pathway 8), and the large ring also could evolve into N5 or N6 directly (pathway 9). Since most of the N-functionalities, except for N5 and N6, are unstable, the reactions are reversible under simulated temperatures. The N7 was emphasised here because it was observed that N7 could be converted into a 3-membered N-containing heterocycle (N3) and benzene ring (C6) via the formation of a bridge bond. Then the cleavage of the C-N bond in N3 results in the formation of R-N and C6 (pathway 10), which is a typical process occurred during the graphitisation of char.

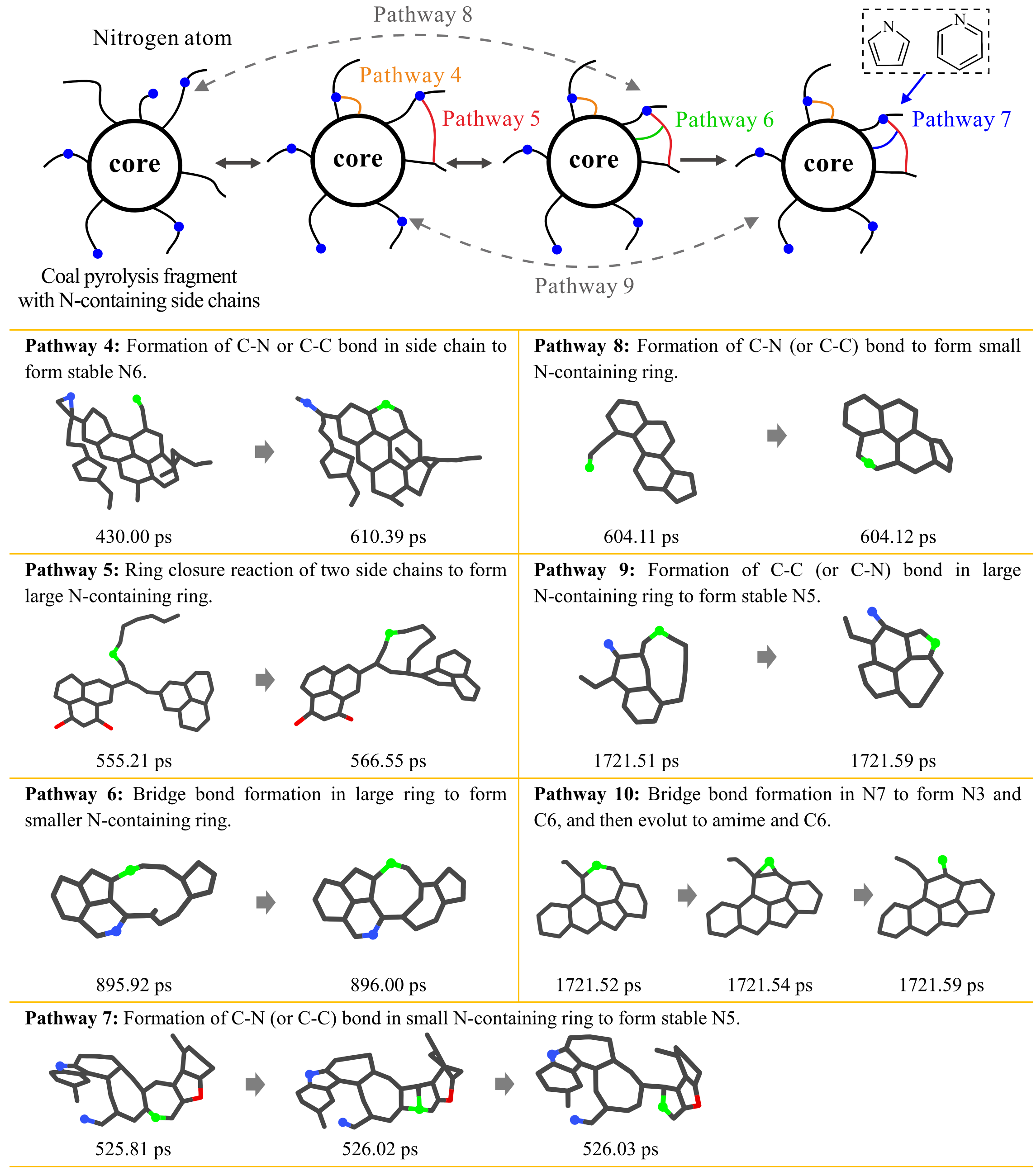

Pathway 4: Formation of C-N or C-C bond in side chain to form stable N6.

Pathway 8: Formation of C-N (or C-C) bond to form small N-containing ring.

Pathway 5: Ring closure reaction of two side chains to form large N-containing ring.

Pathway 9: Formation of C-C (or C-N) bond in large N-containing ring to form stable N5.

Pathway 6: Bridge bond formation in large ring to form smaller N-containing ring.

Pathway 10: Bridge bond formation in N7 to form N3 and C6, and then evolut to amime and C6.

Pathway 7: Formation of C-N (or C-C) bond in small N-containing ring to form stable N5.

Fig. 4.10 Schematic representation of morphological evolution of N-functionalities in coal decomposition fragments. The PAH-like molecules are simplified as "cores" with side chains. The blue dots represent N atoms. Snapshots of seven types of reaction involved in the N evolution process. The black stick is the carbon skeleton; oxygen atoms are marked as red, the key N atoms are marked as green, and H atoms are hidden for better visualisation.

The morphological transformation of the N-functionalities was significantly affected by temperature. X-ray photoelectron spectroscopy analysis results imply that N6 and N5 are the dominant nitrogen functionalities in coal [147]. Therefore, the time evolutions of N5 and N6 groups during MD simulation were analysed, as presented in Fig. 4.10. At the initial pyrolysis stage, the ring-opening process led to a rapid decrease in the number of N5 and N6 groups (before 400 ps), followed by a slow increase during the subsequent stage (400~2000 ps). The number of N5 group increased with increasing temperature in the range of 2200~2600 K. Nevertheless, the number of N5 group decreased as the temperature continuously rise to 2800 K. This is due to the fact that the structure of N5 is less stable than that of N6, and parts of the N5 would be converted to N6 under higher pyrolysis temperatures [54]. Therefore, N6 is the predominant form of organically bound nitrogen under high temperatures, and the number of N6 continuously increases with increasing temperature, as shown in Fig. 4.10(b). The primary reaction pathways of conversion of N5 to N6 are depicted in Fig. 4.11. High temperature led to the cleavage of the C-N bond in N5 group, resulting in a generation of the new radical site on N atom. Then N atom connected to adjacent C atoms to form N6 group. It should be noted that the N-functionalities generated by the cleavage of the C-N bond has the potential to transform into other structures via pathways 4~10. Besides, N atom in N5 could connect to adjacent C atom to form N3 structure, and then the breaking of original C-N bond leads to the formation of N6 structure as illustrated by pathway 12 in Fig. 4.11.

It was observed that the connection position of NH_3 decomposition products on coal fragments has an impact on the evolution pathway. The N atoms connected to C_{end} and C_{middle} tend to form N-containing rings by the linkage of the side chain and then evolve into N6. In comparison, the N atoms connected to C_{ring} are inclined to form stable N6 directly since the adjacent C is already part of the aromatic ring. Therefore, the formation rate of N6 presented in Fig. 4.10(b) increased during the char graphitisation stage (after 1000 ps), where a large number of aromatic rings were formed.

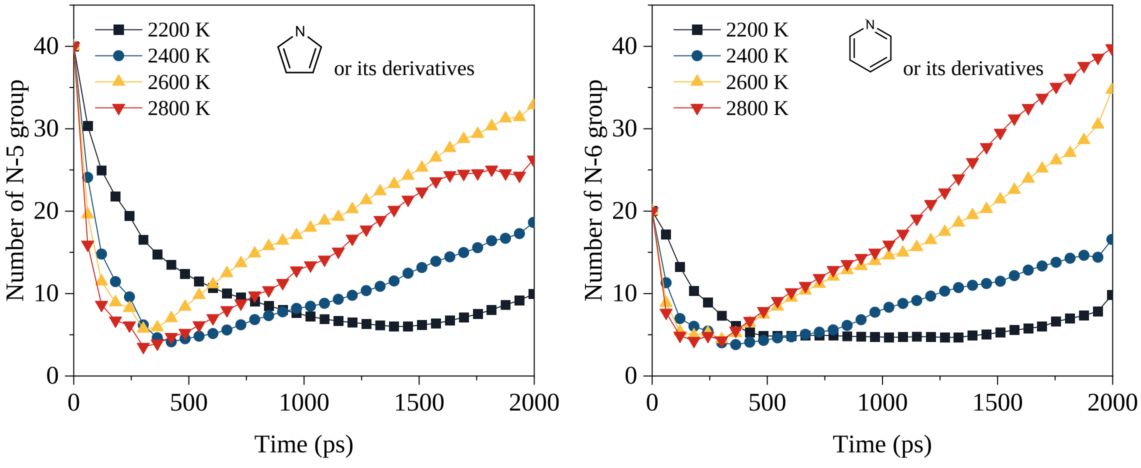

(a) (b)

Fig. 4.11 Time evolutions of (a) N5 group and (b) N6 group in coal/NH_3 co-pyrolysis system.

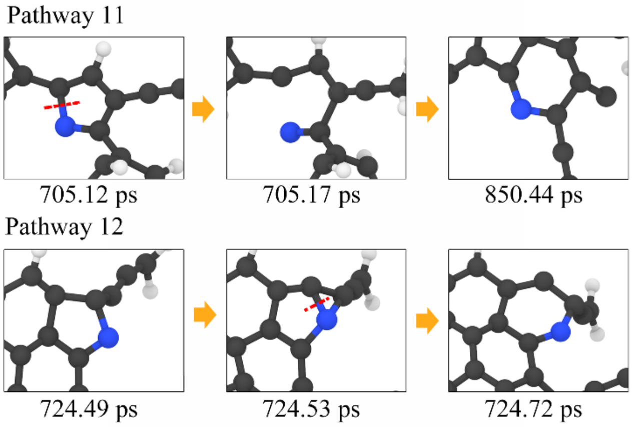

Fig. 4.12 Snapshots of conversion process of N5 to N6 under high temperatures. Dash red lines represent the bond cleavage sites.

4.3 Conclusions

The impact of NH_3 on coal pyrolysis and nitrogen transformation during NH_3/coal co-pyrolysis was studied in this work by ReaxFF MD simulation and supported by a self-designed TG experiment. The interaction between NH_3 and coal during co-pyrolysis can be roughly divided into three stages: (1) the decomposition of NH_3 and coal; (2) the reaction between NH_3 decomposition products and coal fragments; (3) the morphological evolution of the N-functionalities in coal fragments. The detailed reactions involved in each stage were studied.

The validity of MD was verified by comparing the time evolution of $C_{tar/char}$ (carbon number distributed in tar and char products) in MD simulation and coal weight loss data obtained through the TG experiment. The trends shown by the ReaxFF MD simulation results are consistent with the experimental data, indicating that MD simulation is a promising approach for investigating NH_3/coal co-pyrolysis. NH_3 decomposition products could react with PAH precursors to form carbon-nitrogen species, which is less reactive in the subsequent formation of tar and char. Carbon would be captured by nitrogen to form gaseous products, resulting in a faster decrease in coal weight loss.

The reaction between $NH_2^\bullet$ and C atoms in coal is the primary pathway that realises the transformation of N from NH_3 to coal fragments, and high temperature would promote this process. This is because $NH_2^\bullet$ is mainly generated from reaction $NH_3+H \leftrightarrow NH_2^\bullet+H_2$. High temperature promotes the splitting reaction of NH_3 and dehydrogenation reaction of coal, leading to an increase in $NH_2^\bullet$ concentration. Meanwhile, the dehydrogenation reaction of coal enables C atoms provide more reactive sites for $NH_2^\bullet$ adsorption. The ring-opening reactions were promoted with increasing temperature, making more $NH_2^\bullet$ radicals connect to the C_{end} and C_{middle} atoms.

The morphological evolution of the N-functionalities was investigated by analysing atom trajectories. There are several pathways for N-functionalities evolution after $NH_2^\bullet$ attached to coal fragments. N atoms could connect to the side chain to form N6 group directly, or the N-containing side chains could be linked to form a large ring and then evolve into the smaller ring by the formation of internal C-C or C-N bonds. These N-functionalities would turn into N5 or N6 eventually. The structure of N6 is more stable than that of N5, and part of N5 would evolve into N6 group with N3 rings as intermediates under high temperatures. The structure of N-C_{ring} would evolve into N5 or N6 group faster than N-C_{end} and N-C_{middle} since the latter structure tends to form large N-containing rings. This study elucidated the detailed mechanism of N transformation pathways from the molecular point of view, providing a basis for further development of NH_3/coal co-pyrolysis technology.

Chapter 5

The Miscibility of Polyoxymethylene Dimethyl Ethers and Diesel Blend

Polyoxymethylene dimethyl ethers (OME_n) as an alternative fuel have attracted considerable interest in recent years, owing to their much reduced environmental impact. Since OME_n is often blended with diesel, the miscibility and stability of OME_n/diesel mixtures are important for engine operation. In this Chapter, the miscibility of OME_{1-6}/diesel blends is studied. The intermolecular interactions between different types of diesel components and OME_{1-6} are investigated in Section 5.3.2 and Section 5.3.3. Besides, the molecular arrangement of diesel around OME_{1-6} is presented in Section 5.3.4.

5.1 MD modelling methodology

5.1.1 Model construction

The diesel surrogate model adopted in this work was built by Oliveira et al. [94], which contains *n*-paraffins, *iso*-paraffins, naphthenes, aromatics, and heteroatomic molecules. The number of molecules was modified to maintain the same mass fraction of OME_n in the OME_n/diesel mixtures. There are 6 sets of blends, B1~B6. The mass fraction of OME_n is 20% for all the cases considered because the European Stationary Cycle test was conducted using 20% OME_n/diesel blends in heavy-duty engines as the reference for future applications [148]. The structures of diesel and OME_n are shown in Fig. 5.1, and the details of OME_n and diesel molecule number are listed in Table 5.1.

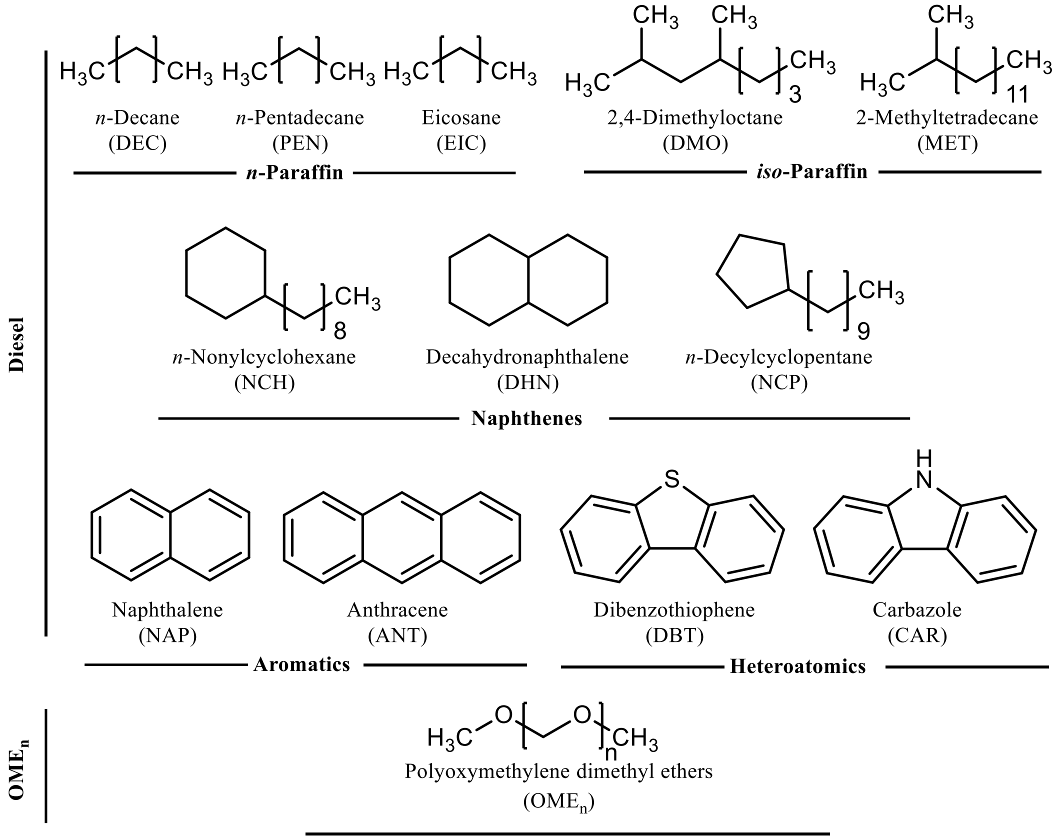

Fig. 5.1 Molecular structures of diesel and OME_n used in the simulations.

Table 5.1 Diesel and OME_n molecules used in the MD simulations.

Class	Molecule name	Code ID	Molecules blend					
			B1	B2	B3	B4	B5	B6
n-Paraffins	*n*-Decane	DEC	150	150	150	150	150	150
	n-Pentadecane	PEN	60	60	60	60	60	60
	Eicosane	EIC	40	40	40	40	40	40
iso-Paraffins	2,4-Dimethyloctane	DMO	150	150	150	150	150	150
	2-Methyltetradecane	MET	60	60	60	60	60	60
Naphthenes	Decahydronaphthalene	DHN	140	140	140	140	140	140
	n-Nonylcyclohexane	NCH	90	90	90	90	90	90
	n-Decylcyclopentane	DCP	90	90	90	90	90	90
Aromatics	Naphthalene	NAP	90	90	90	90	90	90
	Anthracene	ANT	90	90	90	90	90	90
Heteroatomics	Dibenzothiophene	DBT	30	30	30	30	30	30
	Carbazole	CAR	30	30	30	30	30	30
			n=1	n=2	n=3	n=4	n=5	n=6
	Polyoxymethylene dimethyl ethers	OME_n	580	420	330	275	230	200

5.1.2 Simulation setup procedures and details

The MD simulations were performed by using Gromacs 2020 [149], which is an open-source package to perform molecular dynamics simulations. Gromacs is computationally effective at calculating the nonbonded interactions (that usually dominate simulations), and it has been widely used to investigate the solubility of blends [150-152]. The potential energy of aromatics, heteroatomic molecules, and OME$_n$ were described by optimised potentials for liquid simulations all-atom (OPLS-AA) force field, which has been widely used in organic liquids simulations [153-155]. The detailed description of OPLS force filed was discussed in Section 2.3. It should be noted that the acquisition of OPLS force field parameters for OME$_n$ was based on OME$_1$. The molecular simulation accuracy of OME$_{2-6}$ by using OPLS force field will be discussed subsequently.

Initial configurations of OME$_{1-6}$/diesel blends were built by using Packmol [119]. Diesel and OME$_n$ molecules were constructed into a 100×100×100 Å cubic box with a lower initial density to avoid overlapping of atoms. The initial velocities for all atoms were generated randomly following the Maxwell-Boltzmann distribution. Energy minimisation was carried out by using the steepest descent method first, followed by a 200 ps simulation in NVT ensemble to remove the possible overlap between atoms. Finally, the simulation was run in the NPT ensemble for 50 ns to obtain a reasonable density of the system. The size of the final simulation box is around 75×75×75 Å, which is dependent on the atom number and density of each system. The temperature and pressure for all simulations were 300 K and 1 bar.

The periodic boundary conditions were employed in all directions. Fast smooth Particle-Mesh Ewald summation [156] was used for the electrostatic interactions, and a cut off of 1.0 nm was used for the calculation of the van der Waals (vdW) interactions. All bonds associated with hydrogen atoms were constrained by using the linear constraint solver algorithm [157]. Velocity rescaling (v-rescale) method [158] was used to control the temperature, and Berendsen method [159] was applied for pressure coupling. A 2.0 fs time step was used, and output coordinates were obtained every 0.1 ps. The snapshots of trajectories were visualised by Visual Molecular Dynamics (VMD) [160]. Fig. 5.2 shows a snapshot of simulation system.

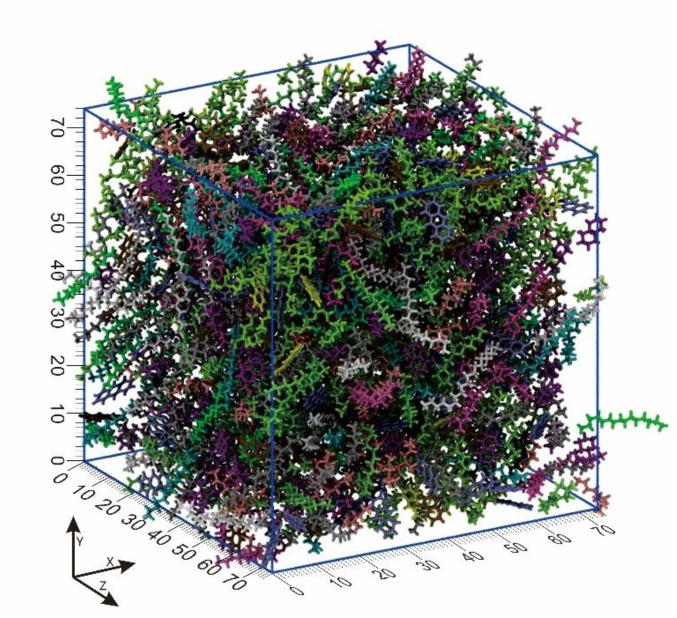

Fig. 5.2. Snapshot of simulation system. Molecules are coloured for visual clarity.

5.1.3 Validation of simulation methods

The LOPLS force field parameters adopted in this work come from Shirley et al. [161]. Atomic partial charges for DBT and CAR were computed based on the 1.14*CM1A-LBCC charge model [162]. Liquid properties, including density, heat of vaporisation, and molecular volumes, are often used as yardsticks to verify the validity of the force fields [107, 163]. In this work, the liquid densities (ρ^{liq}) of pure components at each temperature were calculated to verify the validity of the OPLS and LOPLS force fields. Fig. 5.3(a) and Fig. 5.3(b) show the simulation density results for pure OME_{1-6} and their comparison to experimental data. The density results obtained with the OPLS force field show good agreement with the experimental data for OME_1 to OME_6, with average deviations less than 4% at 1 bar. Although the simulation slightly overestimated the densities especially for OME_{4-6} since the OPLS parameters for ethers were developed using OME_1. The deviation ranges are relatively small, and the trends are consistent with experimental data. Fig. 5.3(c) and Fig. 5.3(d) represent the simulation results of densities of diesel components and corresponding deviations between the experimental and the simulation results. The densities of paraffins (paraffins in this paper refer to *n*-paraffins and *iso*-paraffins) and naphthenes calculated by the LOPLS force field show good agreement with the experimental data, with average deviations less than 2.5% at 1 bar. The deviations for the density of DBT and CAR are ~3.5% and ~5.5%, respectively, which fall within the acceptable range. The results show that the OPLS and LOPLS force fields have the ability to describe the potential energy of diesel and OME_n.

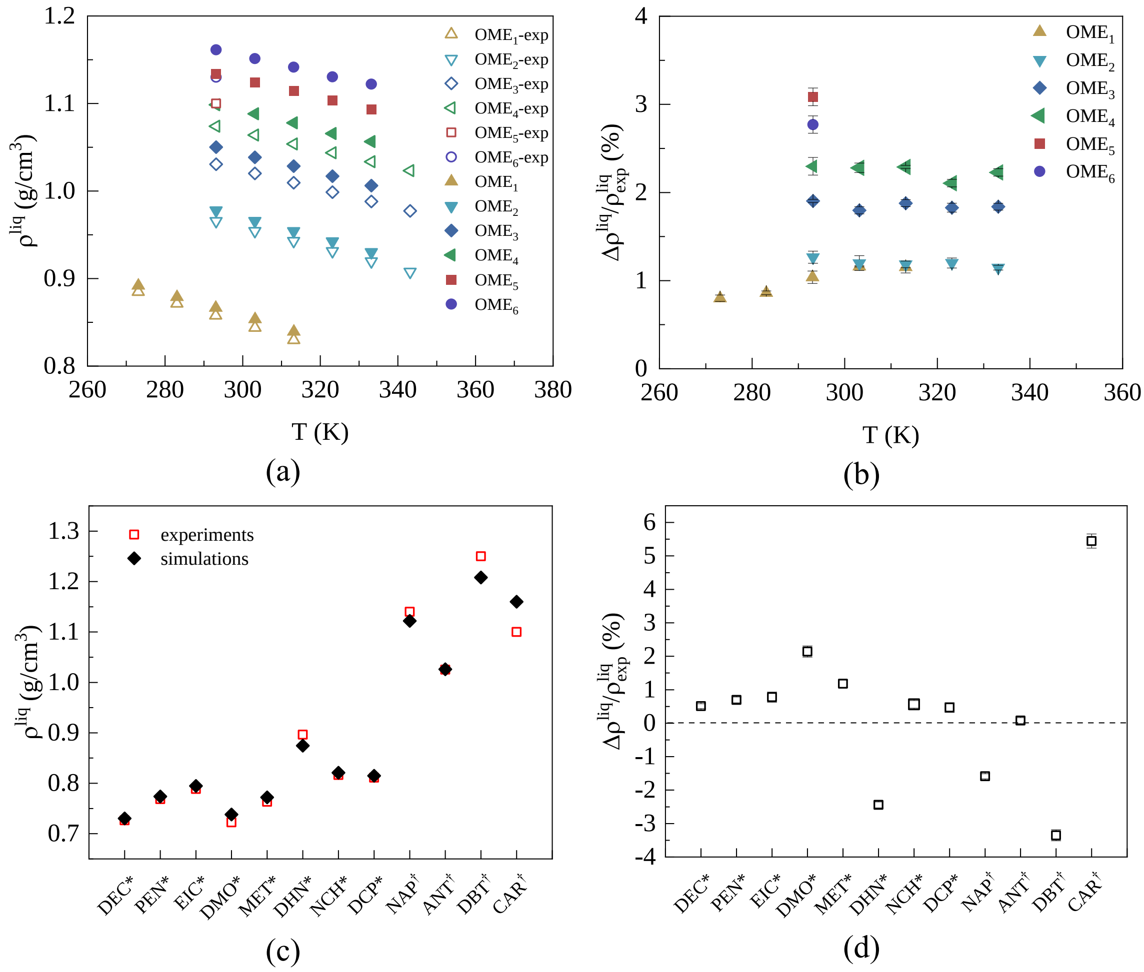

(a) (b)

(c) (d)

Fig. 5.3 Liquid densities for OME$_{1\text{-}6}$ and diesel: (a) Densities of OME$_{1\text{-}6}$ as a function of temperature; (b) Corresponding deviations between the experimental data and the MD results for OME$_{1\text{-}6}$; (c) Experimental and simulation results for densities of diesel components; (d) Corresponding deviations between the experimental data and the MD results for diesel components. Experimental values are taken from the literature [66, 164-168]. Superscripts * and † represent molecules described by LOPLS and OPLS force field, respectively.

5.2 Results and discussion

5.2.1 Miscibility of OME$_{1\text{-}6}$/diesel blends

The composition of diesel is complex, including various paraffins, naphthenes, aromatics, and heteroatomic molecules, which makes the interactions between diesel and OME$_n$ rather complicated. The snapshots of OME$_{1\text{-}6}$ molecules in B1~B6 blends at 0 ns, 10 ns, 20 ns, 30 ns, and 50 ns are presented in Fig. 5.4. It can be observed that OME$_{1\text{-}6}$ molecules were evenly distributed over the whole simulation box at the initial stage. However, the distribution of OME$_{1\text{-}6}$ evolved differently over time. The molecules of OME$_1$

and OME_2 were distributed evenly in the box at 50 ns. Although OME_3 molecules aggregated with each other to a certain degree, they were distributed in the entire space. The OME_{4-6} started aggregate with each other at 10 ns, and the degree of aggregation of OME_{5-6} is higher than that of OME_4. The molecular aggregation of OME_{4-6} in these blends is obvious after 20 ns. Most of the OME_{4-6} molecules were concentrated in specific areas, and only a small part of the molecules was scattered in other spaces after 30 ns. Although OME_{4-6} molecules were mingled with some diesel molecules, the distribution shows that the miscibility of OME_{4-6}/diesel blends is lower than that of OME_{1-3}/diesel blends. In previous experimental studies [83, 84], the OME_n can be blended with diesel well at room temperature when the mass fraction of OME_{1-3} in OME_n reaches 80~90%. The blends of OME_n/diesel blends have a relatively poor solubility when the mass fraction of OME_{4-6} is increased to 55% as reported in an early study [85]. The aggregation of long-chain OME_n would also affect the cloud point, as clusters of long-chain molecules tend to produce flocculent material. Therefore, the cloud point of OME_n and diesel blends increases with increasing OME_n chain length [87, 88]. The simulation results are consistent with experimental observations.

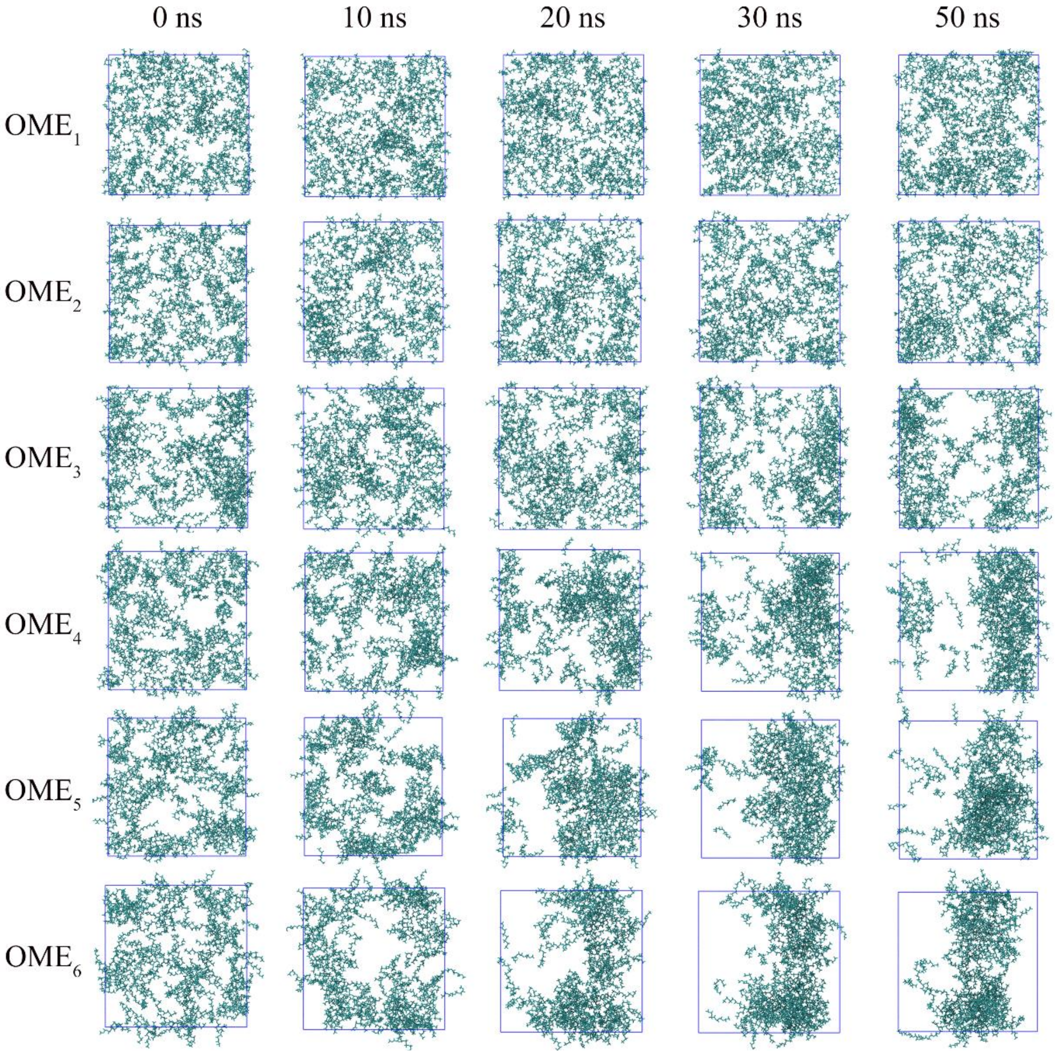

Fig. 5.4 Snapshots of $OME_{1\text{-}6}$ molecule distributions at different times. Diesel molecules have been hidden for clarity.

The phase separation as a function of time was described by the "demixing index" χ_{demix}, which was proposed by Muzet et al. [169] to study the phase separation of binary water-chloroform mixtures. It has been widely used to describe the phase separation of binary mixtures [170, 171]. The blend of diesel and OME_n can be regarded as a binary mixture, where χ_{demix} was calculated from the coordinates of all atoms. The whole simulation box was divided into n cubic boxes with a length of 10 Å. The density of every single box (ρ_i) was computed using $1/\rho_i=1/\rho_{d,i}+1/\rho_{o,i}$ based on the densities of diesel ($\rho_{d,i}$) and OME_n ($\rho_{o,i}$). The "demixing index" was obtained from the average over all boxes ($\chi_{demix}=<\rho_i>$) and normalised in such a way that χ_{demix} ranges from 1.0 (homogeneous system) to 0.0 (two nonoverlapping separated phases).

The demixing index χ_{demix} of B1~B6 blends over time is reported in Fig. 5.5. The χ_{demix} for OME_1/diesel and OME_2/diesel fluctuated between 0.95 and 1, which suggests that the

OME_1 and OME_2 molecules were distributed evenly throughout the box during the whole simulation process. It was shown that OME_1 and OME_2 can be blended with diesel very well. The χ_{demix} for OME_3/diesel blend decreased slightly during 0 to 20 ns and then fluctuated around 0.90. OME_3 molecules aggregate with each other to a certain degree when OME_3 is evenly distributed in the blends by molecular interactions. Such aggregation would not lead to phase separation of OME_3/diesel blend as shown in Fig. 5.4. This means that OME_3 also has good solubility with diesel. Similar trends were found in OME_4/diesel, OME_5/diesel, and OME_6/diesel blends. The significant decrease in χ_{demix} for OME_4/diesel, OME_5/diesel, and OME_6/diesel blends is a reflection of the phase separation. The rate and degree of decrease are faster and greater with the increase of oxymethylene units, which demonstrates that the miscibility of OME_n/diesel blends decreases with the increase of oxymethylene units.

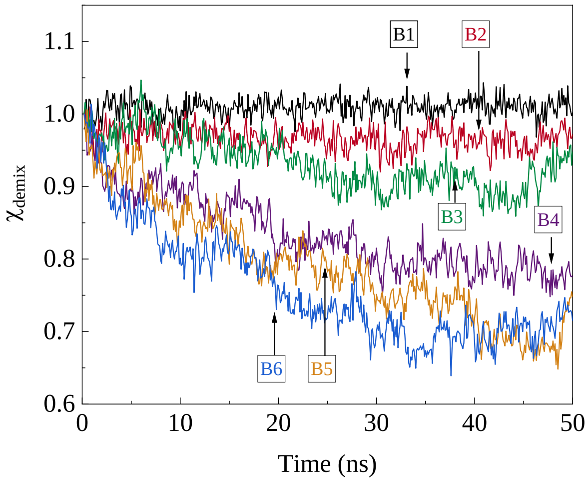

Fig. 5.5 Evolution of the demixing index of B1~B6 systems.

In order to investigate the molecular distribution of OME_n and diesel when phase separation occurred, the snapshots of OME_6 and diesel components at 50 ns are presented in Fig. 5.6. OME_6/diesel blend was chosen to study the molecule distribution due to its high degree of phase separation. It can be seen that the regions with higher local density of OME_6 showed a low density of *n*-paraffins, *iso*-paraffins, and naphthenes, indicating that these molecules are separated from OME_6 molecules. The molecules of aromatics were relatively uniform in the blend, suggesting that the distribution of aromatics is independent of other molecules. The distribution of heteroatomic molecules, i.e., DBT and CAR are closely related to OME_6. These molecules were accumulated around OME_6, especially for CAR. Although the distribution of DBT is related to OME_6, there were some DBT molecules scattered in the simulation box. The OME_6 has good miscibility with aromatic and heteroatomics molecules. Therefore, the miscibility of OME_n and diesel increases with the fraction of aromatic and heteroatomics components. This observation can explain the experimental results reported by Omari et al. [88] that the miscibility of OME_n and paraffin diesel blends is worse than OME_n and fossil diesel mixtures.

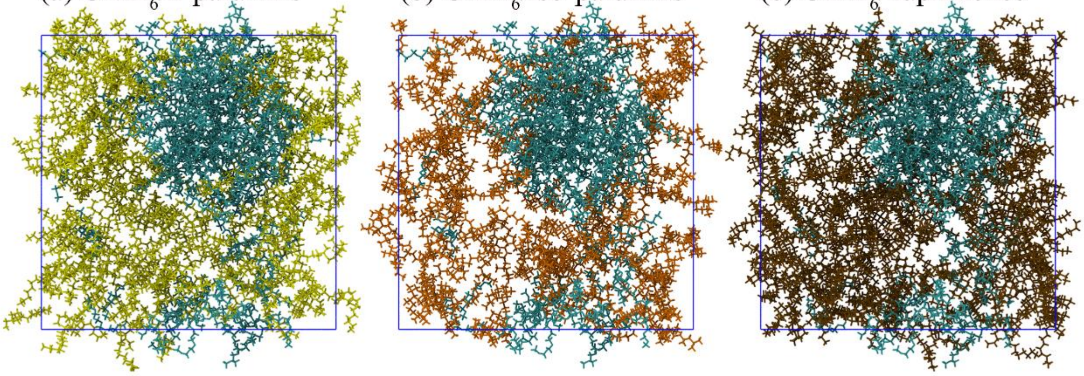
(a) OME_6/*n*-paraffins (b) OME_6/*iso*-paraffins (c) OME_6/naphthenes

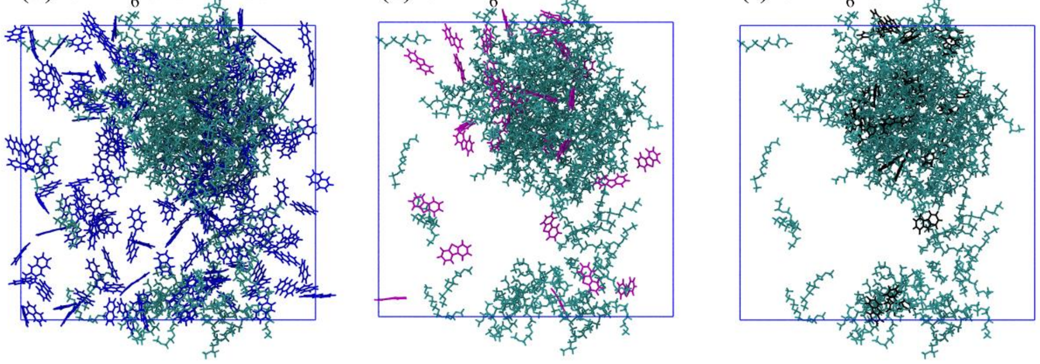
(d) OME_6/aromatics (e) OME_6/DBT (f) OME_6/CAR

Fig. 5.6. Snapshots of OME_6 and diesel components at 50 ns, OME_6 is coloured cyan: (a) OME_6/*n*-paraffins, *n*-paraffins are coloured yellow, containing DEC, PEN, and EIC; (b) OME_6/*iso*-paraffins, *iso*-paraffins are coloured orange, containing DMO and MET; (c) OME_6/naphthenes, naphthenes are coloured ochre, containing DHN, NCH, and DCP; (d) OME_6/aromatics, aromatics are coloured blue, containing NAP and ANT; (e) OME_6/DBT, DBT is coloured magenta; (f) OME_6/CAR, CAR is coloured black.

5.2.2 OME_n intermolecular interactions

Intermolecular interactions are the interactions between two or more molecules. The interactions determine the physical and chemical properties of substances and the stability of chemical complexes [172]. The stability of OME_n/diesel blends would be good if the intermolecular interactions between these molecules in the fuel blends are strong. The investigation of intermolecular interactions between different molecules can offer a clear picture of why the miscibility of OME_n/diesel blend becomes worse with the increase of oxymethylene units. The intermolecular interactions are described by the non-bonded interactions between molecules, which is a combination of vdW and electrostatic potential energy. It should be noted that non-bonded interactions also exist between the atoms that belong to the same molecule. This part should be removed when we calculate the intermolecular interactions by using the total non-bonded interactions in Gromacs.

In order to gain a deeper insight into the reasons that lead to the increase of intermolecular interactions, the potential energy between molecules needs to be studied.

Given that the intermolecular interactions measured in Gromacs depend on the molecule number, while the number of OME_n is varying in B1~B6 blends to ensure the same mass fraction of OME_n. The potential energy was averaged by molecule number for comparison. The vdW (U_{vdW}) and electrostatic ($U_{electrostatic}$) potential energy of single OME_n molecules are shown in Fig. 5.7(a) and Fig. 5.7(b), respectively. Fig. 5.7(c) represents the proportion of $U_{electrostatic}$ in total intermolecular interaction (U_{total}). It should be noted that the potential energy mentioned here only contains the intermolecular potential energy between OME_n molecules, which excludes the energy between OME_n and diesel molecules.

It can be observed that the U_{vdW} and $U_{electrostatic}$ between OME_n decrease with the increase of oxymethylene unit, and the negative values imply that there is an attractive interaction between OME_n molecules, as shown in Fig. 5.7(a) and Fig. 5.7(b). The decrease in potential energy represents the increase of intermolecular forces. The phase separation would occur when such attractive force grows to a certain extent. $OME_{4\text{-}6}$ molecules aggregate to each under the combined effect of vdW and electrostatic interactions. The intermolecular forces between $OME_{1\text{-}2}$ are too weak to maintain a stable cluster. The U_{vdW} and $U_{electrostatic}$ for $OME_{4\text{-}6}$ all experienced varying degrees of decrease over 50 ns, which is because the distance between atoms decreases during the aggregation process. The proportion of the $U_{electrostatic}$ increases with the oxymethylene units as shown in Fig. 5.7(c). For instance, the proportion increases from 22.7% to 30.0% when the oxymethylene unit increases from 1 to 6. It can be deducted that the phase separation of OME_n/diesel is governed by vdW and electrostatic interactions, and the importance of electrostatic interaction grows with the increase of oxymethylene units.

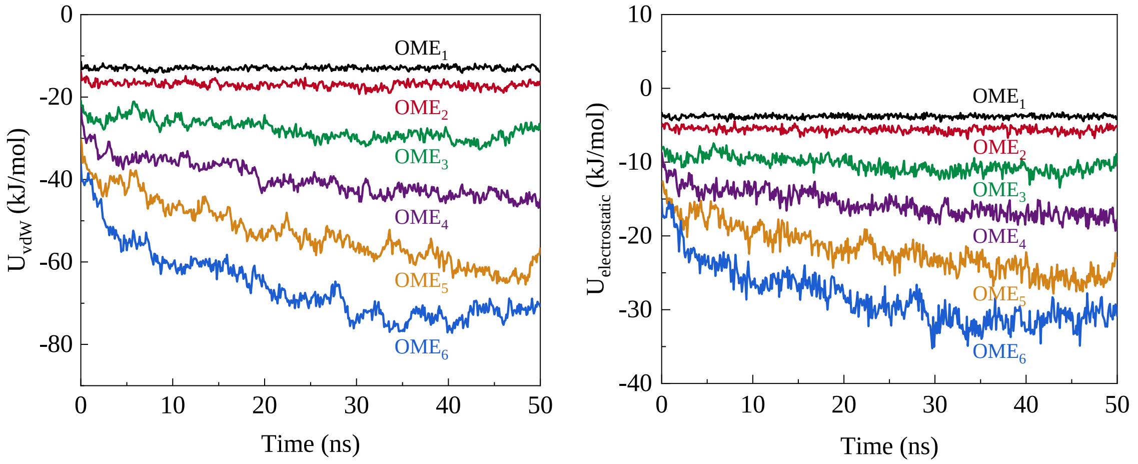

(a) (b)

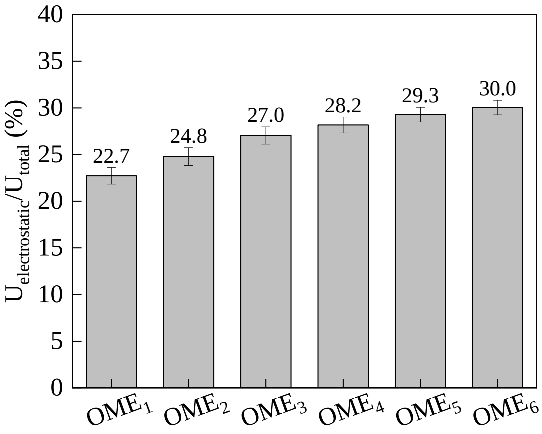

(c)

Fig. 5.7 The potential energy of OME_n molecules in B1~B6 blends over time: (a) VdW potential energy of OME_{1-6} over time; (b) Electrostatic potential energy of OME_{1-6} over time; (c) The proportion of electrostatic potential energy in total intermolecular potential energy.

The electrostatic interaction plays an important role in the aggregation process of OME_n. The impact of ether and methylene groups on the $U_{electrostatic}$ is examined through the analysis of the contribution of each atom to the $U_{electrostatic}$, as shown in Fig. 5.8. The oscillation of the atoms in the equilibrium position would affect the magnitude of the $U_{electrostatic}$. The $U_{electrostatic}$ is positive for oxygen atoms, and negative for carbon and hydrogen atoms most of the time. This is because the electronegativity of oxygen is larger than carbon. The charges for oxygen, carbon, and hydrogen in the oxymethylene unit are -0.4e, +0.2e, +0.1e, respectively. The attractive interaction between ether and methylene groups is stronger than the repulsive interaction between methylene groups and the repulsive interaction between ether groups. Therefore, the attractive interaction between ether and methylene groups would promote the aggregation of OME_n molecules. Meanwhile, the $U_{electrostatic}$ of oxygen would increase with oxymethylene units, but such increment is smaller than the decrement in the $U_{electrostatic}$ of methylene groups. It can be deduced that the increase of electrostatic interactions between OME_n molecules is mainly from the attractive force between ether and methylene groups. The electrostatic force between the ether groups will have a repulsive effect, but such force is less than the overall attractive force.

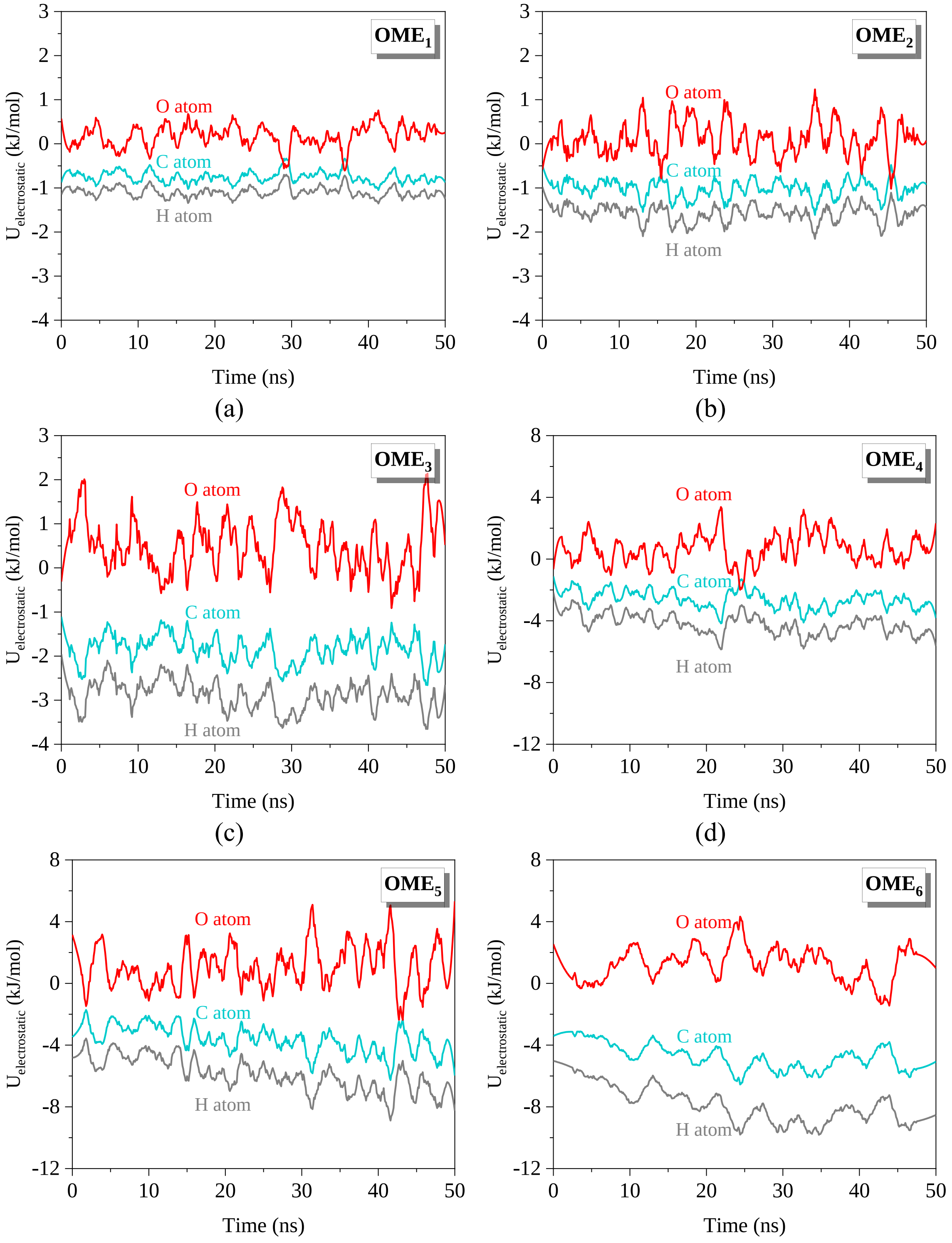

(a) (b) (c) (d) (e) (f)

Fig. 5.8 The contribution of each atom to the $U_{electrostatic}$ between OME_{1-6} molecules. Carbon, oxygen, and hydrogen atoms are represented by C, O, and H, respectively. The red, cyan, and grey line represent the $U_{electrostatic}$ evolution of carbon, oxygen, and hydrogen atoms.

5.2.3 OME$_n$/diesel intermolecular interactions

The intermolecular potential energy between OME$_6$ and diesel molecules is presented in Fig. 5.9. The potential energy is averaged by the molecule number of corresponding component. It can be seen that the U_{vdW} for those molecules aggregated with each other decreases over time, such as OME$_6$/DBT and OME$_6$/CAR. The separation leads to increased vdW interactions, such as OME$_6$/DEC. The U_{vdW} for OME$_6$/CAR is smaller than that of OME$_6$/DBT, which indicates that there is a relatively strong vdW interaction between OME$_6$ and CAR molecules. Electrostatic interaction also plays a significant role in the miscibility of diesel and OME$_n$ mixture. Among all the diesel components, OME$_6$/CAR exhibits the lowest $U_{electrostatic}$. Meanwhile, the proportion of $U_{electrostatic}$ in total potential energy for OME$_6$/CAR is also the highest (41%) as shown in Fig. 5.9 (c). The $U_{electrostatic}$ of OME$_6$/DBT (-10 kJ/mol) is higher compared to OME$_6$/CAR, accounting for 22.4 % of the total intermolecular potential energy. Although the U_{vdW} difference for OME$_6$/CAR and OME$_6$/DBT is small as shown in Fig. 5.9 (a), the difference in $U_{electrostatic}$ makes the miscibility of OME$_6$/CAR better than that of OME$_6$/DBT. The same trend can be found between OME$_6$/DEC and OME$_6$/NAP. The U_{vdW} for OME$_6$/DEC and OME$_6$/NAP are both around -20 kJ/mol at initial stage. Lower $U_{electrostatic}$ enables NAP distributing uniformly in the blend, while DEC is separated from OME$_6$ as presented in Fig. 5.6. It can be deduced that the distribution of OME$_n$ and diesel molecules are determined by the vdW and electrostatic interactions. The $U_{electrostatic}$ differences of OME$_n$ and other diesel components are huge. Diesel components that can form high electrostatic interaction with OME$_n$ tend to have good miscibility with OME$_n$. Therefore, OME$_n$ has good miscibility with the diesel that has a high fraction of aromatic components [89].

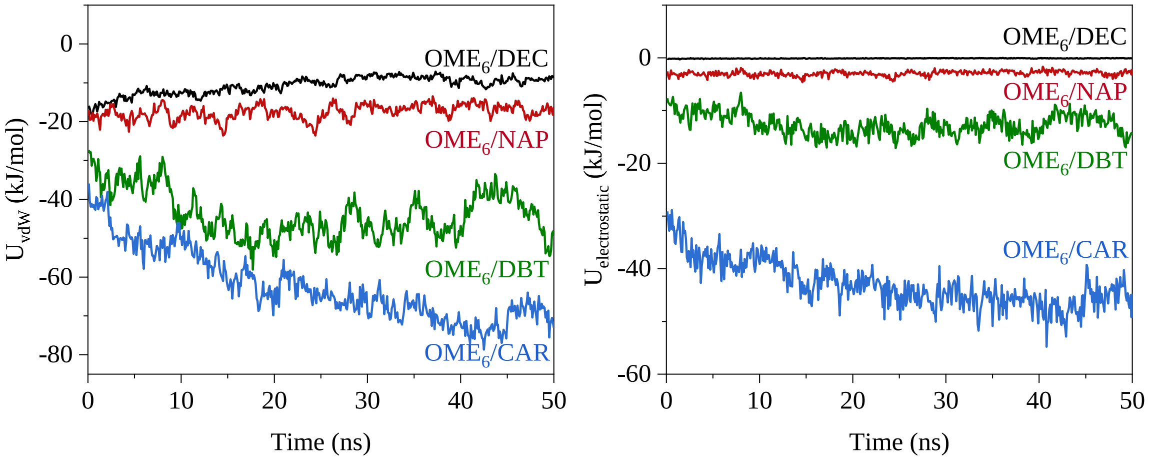

(a) (b)

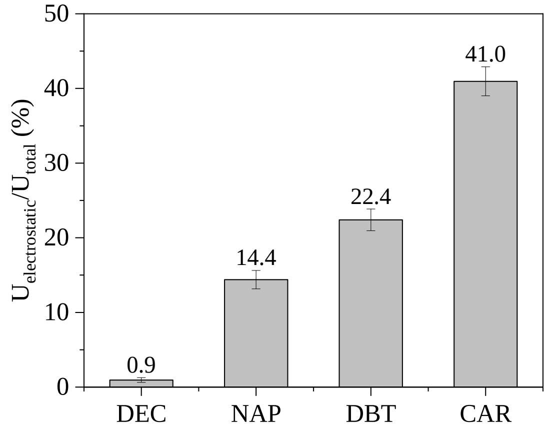

(c)

Fig. 5.9 The potential energy between OME_6 and diesel molecules : (a) The vdW potential energy between OME_6 and diesel molecules over time; (b) Electrostatic potential energy between OME_6 and diesel molecules over time; (c) The proportion of electrostatic potential energy in total intermolecular potential energy.

The atomic contributions of diesel molecules to the $U_{electrostatic}$ between OME_6 and diesel are presented in Fig. 5.10. The $U_{electrostatic}$ for carbons are highly correlated with hydrogen atoms. This is because almost all the hydrogen atoms are bonded with carbon, except for the hydrogen atoms bonded with nitrogen (HN) in CAR, the movement of carbon and hydrogen atoms are consistent. The attractive interaction of hydrogen atoms is counteracted by the repulsive interaction of carbon in OME_6/DEC, which leads to the low electrostatic interaction of OME_6/DEC. It was found that the $U_{electrostatic}$ for methyl or methylene units nearly approach zero, which indicates the structure of the methyl or methylene group is detrimental to the formation of electrostatic interaction with other molecules. The attractive interaction of hydrogen in NAP, DBT, and CAR is higher than the repulsive interaction of carbon, which is due to the planar structure of these molecules.

The electrostatic interaction between diesel and OME_6 molecules does not depend on the molecular structure only, but also relies on the electronegativity difference of atoms in diesel molecules. The diesel molecules will have a strong electrostatic interaction with OME_6 if the former have atoms with a relatively large positive charge. For example, the average charge for hydrogen in NAP and DBT is +0.115e and +0.14e, respectively, which leads to the electrostatic interaction of OME_6/DBT being larger than that of OME_6/NAP. Due to the high electronegativity of nitrogen, the charge for the hydrogen atom bonded with nitrogen atom is +0.45 e, which has the lowest $U_{electrostatic}$ as shown in Fig. 5.10. HN will form hydrogen bonds with the oxygen atoms in OME_n. Meanwhile, the nitrogen also captures the electrons of carbons, resulting in the positive charge of adjacent carbon. The strong electrostatic interaction between OME_n molecules also can be attributed to the electronegativity difference of oxygen and carbon atoms. It can be concluded that the electrostatic interaction between diesel and OME_n molecules depends on the molecular structure of diesel molecules and the electronegativity differences of atoms in diesel molecules.

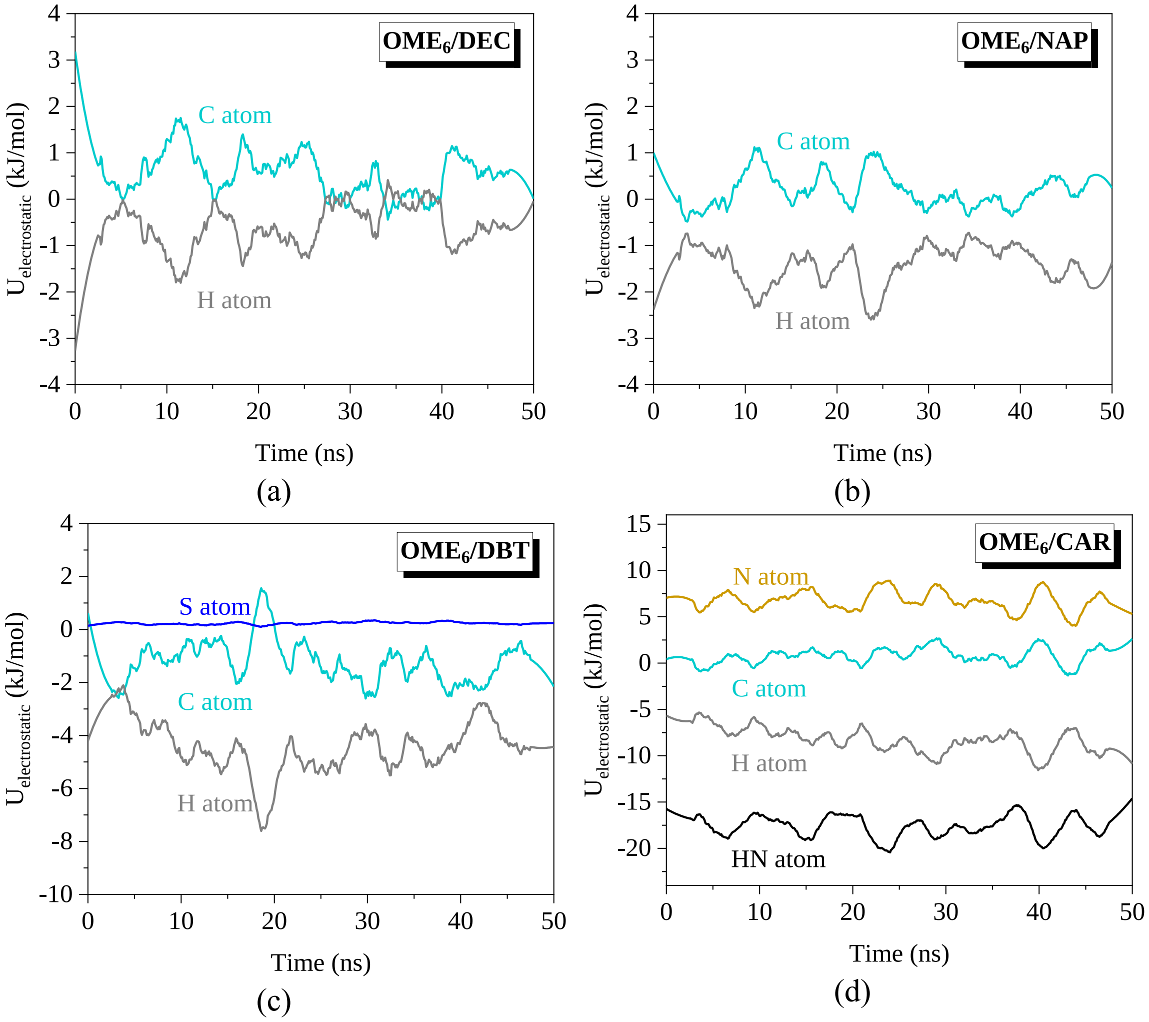

(a) (b) (c) (d)

Fig. 5.10 (a)~(d) The atomic contribution of diesel molecules to the $U_{electrostatic}$ between OME_6 and diesel molecules. Carbon, nitrogen, sulfur, hydrogen atoms bonded with carbon, and hydrogen atom bonded with nitrogen are represented by C, N, S, H, HN, respectively. The cyan, yellow, blue, grey, and black line represent the $U_{electrostatic}$ evolution of carbon, nitrogen, sulfur, hydrogen atoms bonded with carbon, and hydrogen atom bonded with nitrogen, respectively.

5.2.4 The molecular arrangement of diesel around OME_n

The minimum-distance distribution function $g^{md}(r)$ was adopted in this work to study the molecular arrangement of diesel around OME_n. This function was proposed by Martínez and Shimizu [173] to study the solute-solvent interactions. It has been used to study diesel and biodiesel systems [93, 94]. Standard radial distribution functions g(r) cannot be directly used in the study of the solvation of complex, nonspherical solutes. The difference between g(r) and $g^{md}(r)$ is that the former considers the distance between the centre mass of the molecules, while the latter considers the minimum distance between solute-solvent. The minimum-distance distribution function $g^{md}(r)$ can be obtained using the method of Martínez and Shimizu [173], which was computed by using ComplexMixtures [174] in this study.

Fig. 5.11 shows the distribution of the DEC, DMO, and DHN molecules around the OME_{1-6} molecules at 50 ns. The DEC, DMO, and DHN presented a similar profile of distribution around the OME_{1-6} molecules because of their molecular similarities. The maximum $g^{md}(r)$ decreased with the increase of oxymethylene units. For example, the $g^{md}(r)$ for OME_1/DEC is ~4.24, and this value decreased to ~2.38 for OME_6/DEC. This is due to the separation between OME_n and DEC when the number of oxymethylene units is more than 3. The peak of $g^{md}(r)$ was observed at ~2.36 Å to ~2.37 Å for all cases, which is because the equilibrium distance between atoms depends on the value of σ in L-J potential [175]. The outermost layers of paraffins and naphthenes are hydrogen atoms, and the values of σ are the same. Therefore, the distributions of DEC, DMO, and DHN molecules around the OME_{1-6} molecules at the separation interface are similar. Consequently, the present findings show that the chain length and structures (straight, branched, and ring) of alkanes have little impact on the molecular distribution around OME_n.

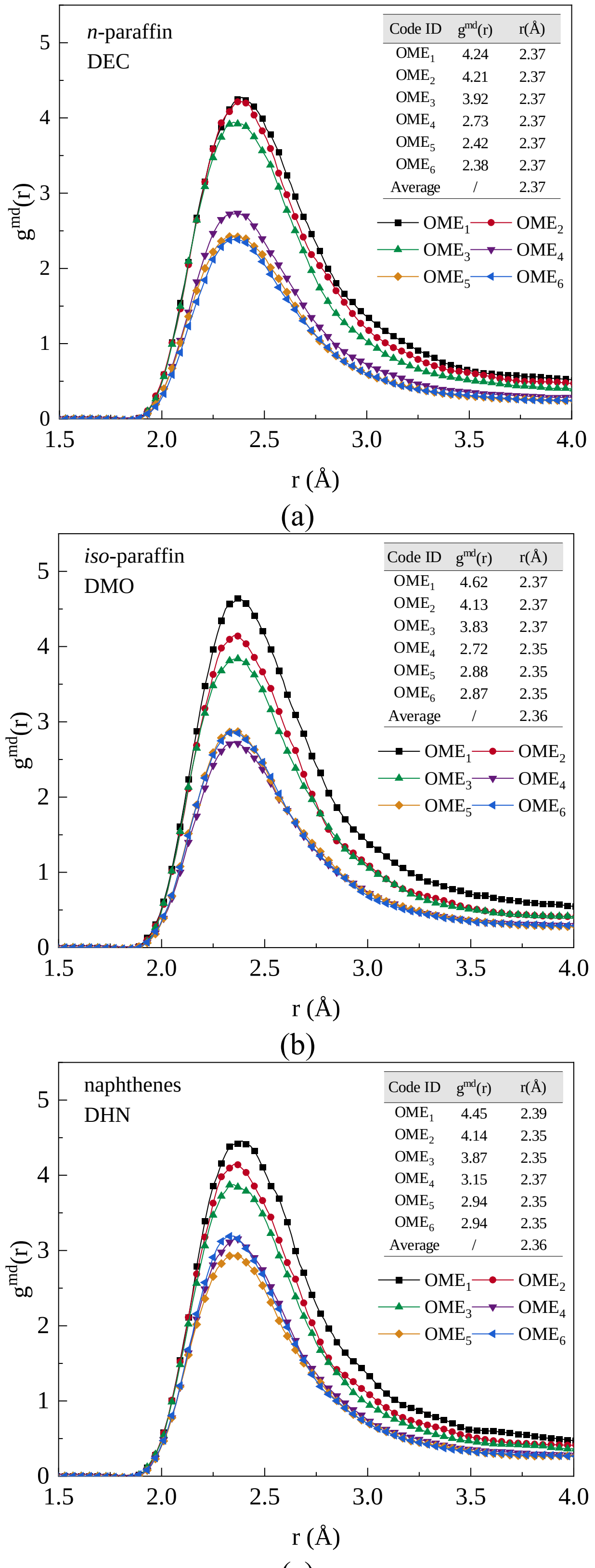

(c)

Fig. 5.11 The distribution of the diesel molecules (solvent) around the OME_{1-6} molecules (solute) at 50 ns for the: (a) DEC, (b) DMO, and (c) DHN. The values of $g^{md}(r)$ and *r* listed in the tables are the maximum $g^{md}(r)$ and corresponding distance.

The distribution of the NAP, DBT, and CAR molecules around the $OME_{1\text{-}6}$ molecules at 50 ns is presented in Fig. 5.12. There is no clear dependence of oxymethylene units on the accumulation of NAP around the $OME_{1\text{-}6}$ since the NAP molecules were distributed evenly in B1~B6 blends as discussed before. The maximum $g^{md}(r)$ for OME_n/CAR increased with oxymethylene units, which is due to the increasing local density of CAR around OME_n. A maximum concentration at ~2.47 Å, ~2.54 Å, and ~2.53 Å was observed for NAP, DBT, and CAR, respectively, which is higher than that of OME_n/paraffins and OME_n/naphthenes. This is due to the fact that the structures of aromatics and heteroatomic molecules are planar, and the closest atoms near OME_n could be hydrogen atoms or other atoms. Thus, it can be suggested that the molecular arrangement of diesel around OME_n depends on the molecular structure.

The atomic contribution of NAP, DBT, and CAR to $g^{md}(r)$ of OME_6 including hydrogen (H), carbon (C), sulfur (S), and nitrogen (N) atoms, are presented in Fig. 5.13. A high concentration of hydrogen atoms at ~2.4 Å was observed. Carbon, sulfur, and nitrogen atoms peaked at ~2.8 Å. The values of σ in L-J potential for carbon, sulfur, and nitrogen atoms are higher than that of hydrogen atoms. Therefore, the equilibrium distances between OME_n and these atoms are larger. In addition, the maximum $g^{md}(r)$ for hydrogen atoms are higher than other atoms, which reveals that the OME_n molecules tend to combine with the hydrogen atoms in aromatics and heteroatomic molecules. It is interesting to note that a peak at ~1.8 Å was observed for CAR, which is related to the orientation of hydrogen bonds.

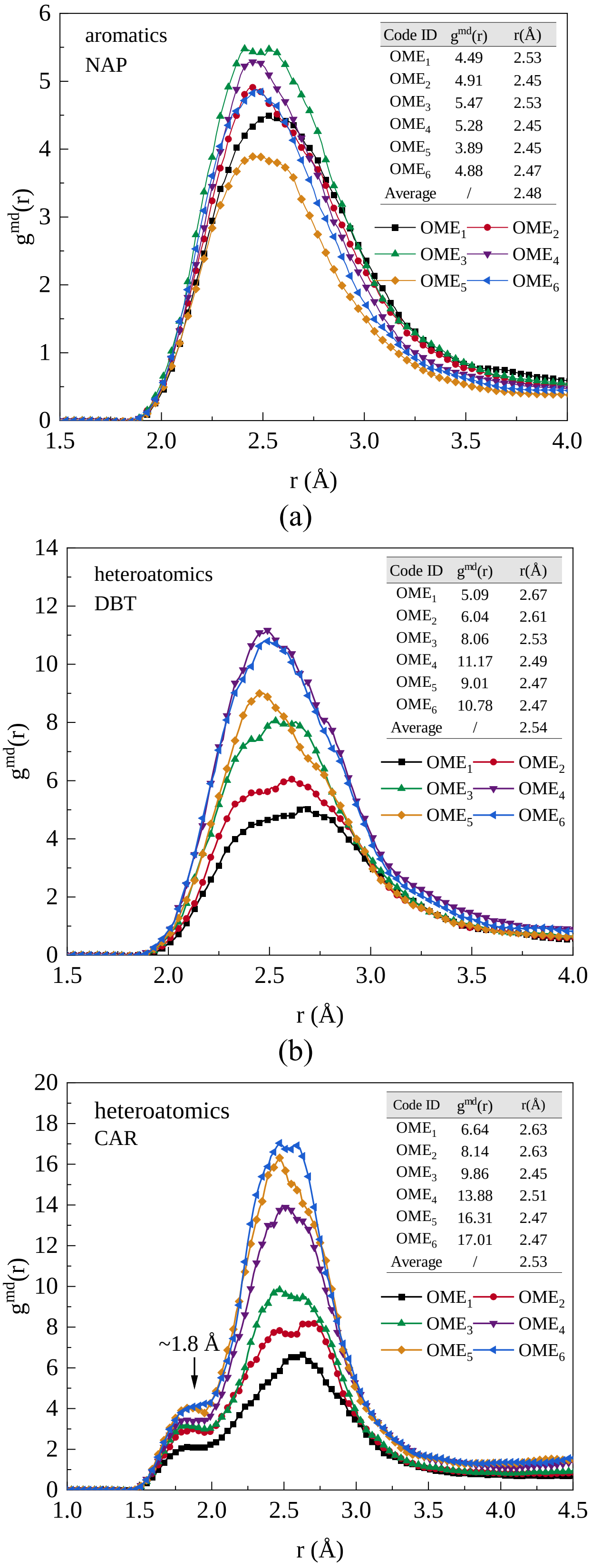

(a)

Code ID	$g^{md}(r)$	r(Å)
OME$_1$	4.49	2.53
OME$_2$	4.91	2.45
OME$_3$	5.47	2.53
OME$_4$	5.28	2.45
OME$_5$	3.89	2.45
OME$_6$	4.88	2.47
Average	/	2.48

(b)

Code ID	$g^{md}(r)$	r(Å)
OME$_1$	5.09	2.67
OME$_2$	6.04	2.61
OME$_3$	8.06	2.53
OME$_4$	11.17	2.49
OME$_5$	9.01	2.47
OME$_6$	10.78	2.47
Average	/	2.54

(c)

Code ID	$g^{md}(r)$	r(Å)
OME$_1$	6.64	2.63
OME$_2$	8.14	2.63
OME$_3$	9.86	2.45
OME$_4$	13.88	2.51
OME$_5$	16.31	2.47
OME$_6$	17.01	2.47
Average	/	2.53

Fig. 5.12 The distribution of the diesel molecules (solvent) around the OME$_{1-6}$ molecules

(solute) for the: (a) NAP, (b) DBT, and (c) CAR. The values of $g^{md}(r)$ and *r* listed in the tables are the maximum $g^{md}(r)$ and the corresponding distance in each case.

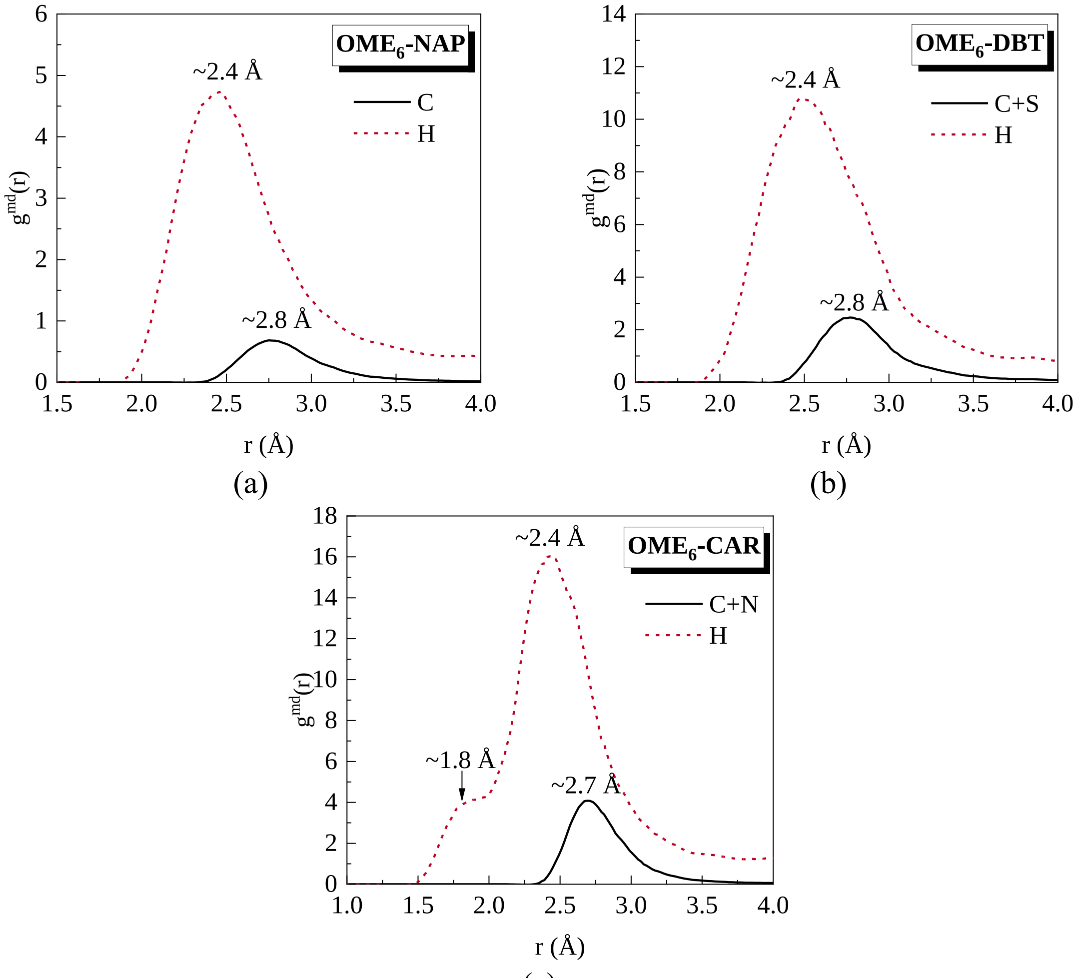

(a) (b)

(c)

Fig. 5.13 The atomic contribution of NAP, DBT, and CAR (solvent) to $g^{md}(r)$ of OME_6 (solute). Hydrogen, carbon, sulfur, and nitrogen atoms in solvent molecules are represented by H, C, S, and N, respectively. The red dash line represents the contribution of hydrogen atoms, and the black solid line is the contribution of other atoms.

5.3 Conclusions

The miscibility of polyoxymethylene dimethyl ethers and diesel blends at 300 K and 1 atm has been studied using molecular dynamics simulation. Various analyses have been conducted to determine the aggregation and separation behaviour of OME_n and diesel molecules. It is found that the miscibility of OME_n and diesel decreases with the increasing number of oxymethylene units. The paraffins and naphthenes in diesel tend to separate with OME_n molecules, while the heteroatomic molecules are prone to accumulate around OME_n. The distribution of aromatics is independent of OME_n molecules. The aromatics and heteroatomic molecules help maintain the stability of OME_n/diesel blends, but their negative impact on pollutant formation of diesel combustion also needs to be taken into account in practical applications.

The analyses of the intermolecular interactions between OME_n and diesel molecules show that the increasing vdW and electrostatic interaction contribute to the aggregation of OME_n and eventually lead to phase separation of OME_n/diesel blends. Electrostatic interaction plays a significant role in the liquid-liquid equilibrium of OME_n/diesel blends. Those types of molecules having strong electrostatic interaction with OME_n tend to accumulate around OME_n, while those with low electrostatic interaction molecules would separate from OME_n. Planar molecular structure and large electronegativity differences of atoms in diesel molecules would lead to the high electrostatic interaction. Molecules containing the polar functional groups and long carbon chains, such as biodiesel or long chain alcohol, have the potential to be used as an additive to stabilize the diesel and OME_n blends.

Minimum-distance distribution functions were used to determine the molecular arrangement of diesel molecules around the OME_n molecules, showing that the paraffins and naphthenes preferentially accumulate at a distance of ~2.36 Å from the surface of the OME_n. The chain structure and chain length of alkanes have little impact on the molecular distribution around OME_n. Compared to carbon, sulfur, and nitrogen atoms, the OME_n molecules tend to combine with the hydrogen atoms of aromatics and heteroatomic molecules at a distance of ~2.4 Å. This study provides a molecular basis for the interpretation of the OME_n/diesel interactions, which can be used to help optimise fuel blend compositions.

Chapter 6

Conclusion and Future Recommendations

6.1 Summary of current work

A number of topics have been investigated in this thesis, including the catalytic supercritical water gasification of cellulose, the nitrogen transfer mechanism during coal and ammonia co-pyrolysis, and the miscibility of the OME_n and diesel blend. MD simulation was performed with the reactive force field and classical force field (OPLS) according to whether or not a chemical reaction occurred. Some physicochemical mechanisms at the molecular level have been obtained.

First, ReaxFF molecular dynamic simulation was performed to elucidate the mechanism of Ni-catalysed supercritical water gasification of cellulose considering the effects of temperature and cellulose to water ratio. Simulations showed that Ni could decrease the activation energy of C-C and C-O bond cleavage, promoting the depolymerisation and ring-opening process of cellulose. The yields of gaseous products increase with the increasing temperature. H_2 yield mainly depends on H free radical number, which can be generated from cellulose dehydrogenation and water splitting reactions. These two reactions were promoted on Ni surface, leading to an increase in H_2 yield. In the presence of Ni catalyst, water plays a limited role in providing H free radicals to produce H_2, while the hydrogen atoms in cellulose are the primary source of H_2 generation. Meanwhile, reducing the concentration of $^{\bullet}OH$ could enhance H_2 production as the combination of $^{\bullet}OH$ and $^{\bullet}H$ is a H radical consumption process. Small organic fragments would be absorbed on the Ni surface, where they undergo deoxygenation via the cleavage of C-O bonds, resulting in a decrease in CO and CO_2 yields. The increase in water mass fraction would promote the H_2 yield as more H radical would be produced due to water splitting reaction. Moreover, the addition of water would occupy the Ni active sites and prevent the adsorption of organic fragments. These dissociative fragments are prone to produce more CO. The carbon deposition on the Ni surface results in the deactivation of the catalyst. Simulation results suggested that carbon deposition and permeation increase with increasing temperature. In contrast, the increase in water mass fraction can favour carbon elimination from the catalyst surface.

In the study of coal and ammonia co-pyrolysis, ReaxFF molecular dynamic simulation was performed to elucidate the effect of NH_3 on coal pyrolysis and nitrogen transformation during coal/NH_3 co-pyrolysis. The results indicate that the decomposition products of NH_3 and coal would react with each other to form gaseous N-containing species, which is less reactive during the subsequent formation of char and tar. Meanwhile, the detailed decomposition process of NH_3 was studied. It was found that the reaction $NH_3+H^{\bullet}\leftrightarrow NH_2^{\bullet}+H_2$ is the primary pathway for $NH_2^{\bullet}$ radical generation. The concentration of $NH_2^{\bullet}$ radical increases with increasing temperature due to the promoted splitting reaction of NH_3 and the dehydrogenation of coal. The increase in $NH_2^{\bullet}$ radical concentration promotes the reaction of $NH_2^{\bullet}$ and coal decomposition products. The cleavage of C-C and C-H bonds caused by higher temperatures also promotes the interaction between $NH_2^{\bullet}$ and coal fragments since it could generate more radical sites on coal fragments for attaching $NH_2^{\bullet}$. The nitrogen functionalities in the coal fragment would evolve into relatively stable N5 and N6 groups gradually. In addition, the morphological evolution routes of the N-functionalities in coal fragments were presented. This work provides molecular understandings on the mechanism of N transformation pathways during coal/NH_3 co-pyrolysis.

Finally, OPLS force field was used to investigate the miscibility of OME_{1-6} and diesel blends. The results suggest that the miscibility of OME_n and diesel blends decreases with the increasing number of oxymethylene units. The aromatics and heteroatomic molecules help maintain the stability of OME_n/diesel blends. The intermolecular interactions between OME_{1-6} and diesel molecules were investigated, which revealed that the electrostatic interaction plays a significant role in the liquid-liquid equilibrium of OME_n/diesel blends. The molecules in diesel having strong electrostatic interaction with OME_n are prone to accumulate around OME_n. The electrostatic interaction between diesel and OME_n molecules depends on the molecular structure and electronegativity differences of atoms in diesel molecules. The analyses of MD results coupled to minimum-distance distribution functions show an accumulation of paraffins and naphthenes close to OME_n at ~2.36 Å, and suggest a strong interaction of OME_n with diesel carbazole molecules via hydrogen bonds. The results also indicate that the chain length and structure of alkanes have little impact on the molecular distribution around OME_n.

6.2 Future recommendation

6.2.1 Catalytic SCWG of cellulose and lignin

Lignin is the third major component of lignocellulose, accounting for 10~35% by weight and up to 40% of energy in biomass [176]. The SCWG of lignin has been studied widely, as listed in Chapter 1 Table 1.1. However, the investigation of the synergistic mechanism of cellulose and lignin SCWG with the addition of a catalyst is not carried out yet. Cellulose and lignin have different structural features. A significant proportion of the hydrogen atoms in lignin are bonded to aromatic carbons. It was found that the H radicals generated in the SCWG system would react with H atoms in biomass to produce H_2 in Chapter 3. The degree of dehydrogenation reaction varies between lignin and cellulose, leading to a different concentration of H radicals when the ratio of lignin to cellulose is altered. The effect of H radicals produced by one component on the reaction of the other component is currently unknown.

Furthermore, the structural difference between lignin and cellulose may affect coke deposition on the catalyst surface. The activation energy for C-C bond cleavage in aromatic rings and alkanes differs, and it is unclear which types of C atoms are prone to adsorption on the catalyst. Investigating the catalytic SCWG of a mixture of cellulose and lignin will provide a foundation for the industrial gasification of biomass.

6.2.2 Coal and ammonia co-combustion

In Chapter 4, the transformation of nitrogen in the co-pyrolysis of coal and ammonia was studied. However, the emission of NO_x during the co-combustion of coal and ammonia is currently unknown. It was suggested that the N-functionalities in the char formed during co-pyrolysis may influence NO_x emissions. Further research is needed to determine which types of N-functionalities are more prone to be oxidised into NO_x. To investigate the NO_x emissions during co-combustion, oxygen will be introduced to the system in addition to coal and ammonia. The effect of temperature on NO_x emissions and the mechanisms of nitrogen oxidation also require further study. Additionally, the impact of the ratio of ammonia added on NOx emissions requires further investigation.

6.2.3 Machine learning force fields development

Presently, the development of force fields is based mainly on a specific application scenario. For example, the acquisition of OPLS force field parameters for OME_n was based on OME_1. There is a deviation in using these parameters to calculate properties of OME_{5-6}. It is necessary to optimise the transferability of force fields. In recent years, machine learning (ML) techniques have been applied to the development of molecular dynamics (MD) force fields, referred to as ML-based force fields, with the goal of narrowing the gap between the accuracy of ab initio methods and the efficiency of classical force fields. The key concept is to learn the statistical relationship between chemical structure and potential energy without relying on predetermined notions of chemical bonds or understanding of relevant interactions [177, 178]. The use of machine learning in the development of force fields has the potential to improve the accuracy and efficiency of molecular dynamics simulations, making it possible to study a broader range of physicochemical phenomena.

References

[1] Tollefson J. Carbon emissions hit new high: warning from COP27. *nature News.* 2022.

[2] IEA. Energy statistics data browser; 2022. Available from: https://www.iea.org/data-and-statistics/data-tools/energy-statistics-data-browser.

[3] Hannah Ritchie, Max Roser, Rosado P. CO_2 and greenhouse gas emissions; 2020. Available from: https://ourworldindata.org/CO2-and-other-greenhouse-gas-emissions.

[4] Ishaq H, Dincer I, Crawford C. A review on hydrogen production and utilization: Challenges and opportunities. *International Journal of Hydrogen Energy* 2022;47(62):26238-64.

[5] Atilhan S, Park S, El-Halwagi MM, Atilhan M, Moore M, Nielsen RB. Green hydrogen as an alternative fuel for the shipping industry. *Current Opinion in Chemical Engineering* 2021;31:100668.

[6] Sazali N. Emerging technologies by hydrogen: A review. *International Journal of Hydrogen Energy* 2020;45(38):18753-71.

[7] Dincer I, Acar C. Review and evaluation of hydrogen production methods for better sustainability. *International journal of hydrogen energy* 2015;40(34):11094-111.

[8] Vojvodic A, Medford AJ, Studt F, Abild-Pedersen F, Khan TS, Bligaard T, et al. Exploring the limits: A low-pressure, low-temperature Haber–Bosch process. *Chemical Physics Letters* 2014;598:108-12.

[9] Macfarlane DR, Cherepanov PV, Choi J, Suryanto BHR, Hodgetts RY, Bakker JM, et al. A Roadmap to the Ammonia Economy. *Joule* 2020;4(6):1186-205.

[10] Society TR. 2020 Ammonia: Zero-carbon fertiliser, fuel and energy store.; 2020. Available from: https://royalsociety.org/topics-policy/projects/low-carbon-energy-programme/green-ammonia/.

[11] Kobayashi H, Hayakawa A, Somarathne KDKA, Okafor EC. Science and technology of ammonia combustion. *Proceedings of the Combustion Institute* 2019;37(1):109-33.

[12] Patil AR, Taji SG. Effect of oxygenated fuel additive on diesel engine performance and emission: A review. *IOSR Journal of Mechanical and Civil Engineering (IOSR-*

JMCE) 2013:30-5.

[13] Okolie JA, Rana R, Nanda S, Dalai AK, Kozinski JA. Supercritical water gasification of biomass: A state-of-the-art review of process parameters, reaction mechanisms and catalysis. *Sustainable Energy & Fuels* 2019;3(3):578-98.

[14] Shrotri A, Kobayashi H, Fukuoka A. Cellulose depolymerization over heterogeneous catalysts. *Accounts of Chemical Research* 2018;51(3):761-8.

[15] Lee CS, Conradie AV, Lester E. Review of supercritical water gasification with lignocellulosic real biomass as the feedstocks: Process parameters, biomass composition, catalyst development, reactor design and its challenges. *Chemical Engineering Journal* 2021;415:128837.

[16] Hu Y, Gong M, Xing X, Wang H, Zeng Y, Xu CC. Supercritical water gasification of biomass model compounds: A review. *Renewable and Sustainable Energy Reviews* 2020;118:109529.

[17] Hassan NS, Jalil AA, Vo DVN, Nabgan W. An overview on the efficiency of biohydrogen production from cellulose. *Biomass Conversion and Biorefinery* 2020.

[18] Yakaboylu O, Harinck J, Smit K, De Jong W. Supercritical water gasification of biomass: A literature and technology overview. *Energies* 2015;8(2):859-94.

[19] Hu Y, Gong M, Feng S, Xu C, Bassi A. A review of recent developments of pre-treatment technologies and hydrothermal liquefaction of microalgae for bio-crude oil production. *Renewable and Sustainable Energy Reviews* 2019;101:476-92.

[20] Guo Y, Wang S, Xu D, Gong Y, Ma H, Tang X. Review of catalytic supercritical water gasification for hydrogen production from biomass. *Renewable and Sustainable Energy Reviews* 2010;14(1):334-43.

[21] Ren J, Cao J, Zhao X, Yang F, Wei X. Recent advances in syngas production from biomass catalytic gasification: A critical review on reactors, catalysts, catalytic mechanisms and mathematical models. *Renewable and Sustainable Energy Reviews* 2019;116:109426.

[22] Zeng X, Fang M, Lv T, Tian J, Xia Z, Cen J, et al. Enhanced hydrogen production by the catalytic alkaline thermal gasification of cellulose with Ni/Fe dual-functional CaO based catalysts. *International Journal of Hydrogen Energy* 2021;46(65):32783-99.

[23] Lee I-G, Ihm S-K. Catalytic gasification of glucose over Ni/activated charcoal in supercritical water. *Industrial & Engineering Chemistry Research* 2009;48(3):1435-42.

[24] Grams J, Potrzebowska N, Goscianska J, Michalkiewicz B, Ruppert AM. Mesoporous silicas as supports for Ni catalyst used in cellulose conversion to hydrogen rich gas. *International Journal of Hydrogen Energy* 2016;41(20):8656-67.

[25] Ruppert AM, Niewiadomski M, Grams J, Kwapiński W. Optimization of Ni/ZrO_2 catalytic performance in thermochemical cellulose conversion for enhanced hydrogen production. *Applied Catalysis B: Environmental* 2014;145:85-90.

[26] Świerczyński D, Libs S, Courson C, Kiennemann A. Steam reforming of tar from a biomass gasification process over Ni/olivine catalyst using toluene as a model compound. *Applied Catalysis B: Environmental* 2007;74(3-4):211-22.

[27] Li H, Xu B, Jin H, Luo K, Fan J. Molecular dynamics investigation on the lignin gasification in supercritical water. *Fuel Processing Technology* 2019;192:203-9.

[28] Liu X, Wang T, Chu J, He M, Li Q, Zhang Y. Understanding lignin gasification in supercritical water using reactive molecular dynamics simulations. *Renewable Energy* 2020;161:858-66.

[29] Ponnuchamy V, Sandak J, Sandak A. Revealing of supercritical water gasification process of lignin by reactive force field molecular dynamics simulations. *Processes* 2021;9(4):714.

[30] Zhang Y, Li J, Wang J, Yang X, Wang B. ReaxFF MDSs-based studies on gasification of glucose in supercritical water under microwave heating. *International Journal of Hydrogen Energy* 2016;41(31):13390-8.

[31] Monti S, Srifa P, Kumaniaev I, Samec JSM. ReaxFF simulations of lignin fragmentation on a Palladium-based heterogeneous catalyst in methanol–water solution. *The Journal of Physical Chemistry Letters* 2018;9(18):5233-9.

[32] Wang T, Liu X, Liu H, He M. Synergistic effect of supercritical water and nano-catalyst on lignin gasification. *International Journal of Hydrogen Energy* 2021;46(70):34626-37.

[33] Zhang H, Chen F, Zhang J, Han Y. Supercritical water gasification of fuel gas production from waste lignin: The effect mechanism of different oxidized iron-based catalysts. *International Journal of Hydrogen Energy* 2021;46(59):30288-99.

[34] Han Y, Chen F, Ma T, Gong H, Al-Shwafy KWA, Li W, et al. Size effect of a Ni nanocatalyst on supercritical water gasification of lignin by reactive molecular dynamics simulations. *Industrial & Engineering Chemistry Research* 2019;58(51):23014-24.

[35] Saha B, Patra AS, Mukherjee AK, Paul I. Interaction and thermal stability of carboxymethyl cellulose on α-Fe_2O_3 (001) surface: ReaxFF molecular dynamics simulations study. *Journal of Molecular Graphics and Modelling* 2021;102:107787.

[36] Mueller JE, Van Duin ACT, Goddard WA. Development and validation of ReaxFF reactive force field for hydrocarbon chemistry catalyzed by Nickel. *The Journal of Physical Chemistry C* 2010;114(11):4939-49.

[37] Shin YK, Kwak H, Vasenkov AV, Sengupta D, Van Duin ACT. Development of a ReaxFF reactive force field for Fe/Cr/O/S and application to oxidation of butane over a pyrite-covered Cr_2O_3 catalyst. *ACS Catalysis* 2015;5(12):7226-36.

[38] Castro-Marcano F, Kamat AM, Russo MF, Van Duin ACT, Mathews JP. Combustion of an Illinois No. 6 coal char simulated using an atomistic char representation and the ReaxFF reactive force field. *Combustion and Flame* 2012;159(3):1272-85.

[39] Chenoweth K, Van Duin ACT, Goddard WA. ReaxFF reactive force field for molecular dynamics simulations of hydrocarbon oxidation. *The Journal of Physical*

Chemistry A 2008;112(5):1040-53.

[40] Song Z, Bai M, Yang Z, Lei H, Qian M, Zhao Y, et al. Gasification of α-O-4 linkage lignin dimer in supercritical water into hydrogen and carbon monoxide: Reactive molecular dynamic simulation study. *Fuel* 2022;329:125387.

[41] Wang T, Liu X, Huang S, Waheed A, He M. Modelling co-gasification of plastic waste and lignin in supercritical water using reactive molecular dynamics simulations. *International Journal of Hydrogen Energy* 2022;47(49):21060-6.

[42] Wei Z, Li Y, Zhang C, Yang L, Chu L. Revealing the mechanism on steam co-gasification of cellulose and polyethylene: A combined ReaxFF and DFT study. *Fuel* 2023;334:126784.

[43] Van Duin ACT, Dasgupta S, Lorant F, Goddard WA. ReaxFF: a reactive force field for hydrocarbons. *The Journal of Physical Chemistry A* 2001;105(41):9396-409.

[44] Rismiller SC, Groves MM, Meng M, Dong Y, Lin J. Water assisted liquefaction of lignocellulose biomass by ReaxFF based molecular dynamic simulations. *Fuel* 2018;215:835-43.

[45] Jin H, Wu Y, Zhu C, Guo L, Huang J. Molecular dynamic investigation on hydrogen production by furfural gasification in supercritical water. *International Journal of Hydrogen Energy* 2016;41(36):16064-9.

[46] Xu Y, Wang H, Liu X, Zhu J, Xu J, Xu M. Mitigating CO_2 emission in pulverized coal-fired power plant via co-firing ammonia: A simulation study of flue gas streams and exergy efficiency. *Energy Conversion and Management* 2022;256:115328.

[47] Chen P, Fang Y, Wang P, Gu M, Luo K, Fan J. The effect of ammonia co-firing on NO heterogeneous reduction in the high-temperature reduction zone of coal air-staging combustion: Experimental and quantum chemistry study. *Combustion and Flame* 2022;237:111857.

[48] Tamura M, Gotou T, Ishii H, Riechelmann D. Experimental investigation of ammonia combustion in a bench scale 1.2 MW-thermal pulverised coal firing furnace. *Applied Energy* 2020;277:115580.

[49] Wang X, Fan W, Chen J, Feng G, Zhang X. Experimental study and kinetic analysis of the impact of ammonia co-firing ratio on products formation characteristics in ammonia/coal co-firing process. *Fuel* 2022;329:125496.

[50] Ishihara S, Zhang J, Ito T. Numerical calculation with detailed chemistry on ammonia co-firing in a coal-fired boiler: Effect of ammonia co-firing ratio on NO emissions. *Fuel* 2020;274:117742.

[51] Zhang J, Ito T, Ishii H, Ishihara S, Fujimori T. Numerical investigation on ammonia co-firing in a pulverized coal combustion facility: Effect of ammonia co-firing ratio. *Fuel* 2020;267:117166.

[52] Sousa Cardoso J, Silva V, Eusébio D, Tarelho LAC, Hall MJ, Grinberg Dana A. Numerical modelling of ammonia-coal co-firing in a pilot-scale fluidized bed reactor: Influence of ammonia addition for emissions control. *Energy Conversion and Management* 2022;254:115226.

[53] Chen P, Wang Y, Wang P, Gu M, Jiang B, Luo K, et al. Oxidation mechanism of ammonia-N/coal-N during ammonia-coal co-combustion. *International Journal of Hydrogen Energy* 2022;47(83):35498-514.

[54] Jiao T, Fan H, Liu S, Yang S, Du W, Shi P, et al. A review on nitrogen transformation and conversion during coal pyrolysis and combustion based on quantum chemical calculation and experimental study. *Chinese Journal of Chemical Engineering* 2021;35:107-23.

[55] McCarthy MI, Rosmus P, Werner HJ, Botschwina P, Vaida V. Dissociation of NH_3 to NH_2+H. *The Journal of Chemical Physics* 1987;86(12):6693-700.

[56] Mänz U, Reinsch E-A, Rosmus P, Werner H-J, Neil SO. Dissociation of NH_3 to NH + H_2. *J Chem Soc, Faraday Trans* 1991;87(12):1809-14.

[57] Stańczyk K. Nitrogen oxide evolution from nitrogen-containing model chars combustion. *Energy & fuels* 1999;13(1):82-7.

[58] Liu X, Luo Z, Yu C, Xie G. Conversion mechanism of fuel-N during pyrolysis of biomass wastes. *Fuel* 2019;246:42-50.

[59] Deng L, Jin X, Zhang Y, Che D. Release of nitrogen oxides during combustion of model coals. *Fuel* 2016;175:217-24.

[60] Hong D, Yuan L, Wang C. Competition between NH_3-O_2 reaction and char-O_2 reaction and its influence on NO generation and reduction during char/NH_3 co-combustion: Reactive molecular dynamic simulations. *Fuel* 2022;324:124666.

[61] Zhang P, Zhang K, Cheng X, Liu Y, Wu H. Analysis of inhibitory mechanisms of ammonia addition on soot formation: A combined reaxff md simulations and experimental study. *Energy & Fuels* 2022;36(19):12350-64.

[62] Zheng M, Li X. Investigation of N transfer during coal char oxidation by reactive molecular dynamics. *Energy & Fuels* 2022;36(21):13073-83.

[63] Wang J, Wang Y, Li G, Ding Z, Lu Q, Liang Y. ReaxFF molecular dynamics study on nitrogen-transfer mechanism in the hydropyrolysis process of lignite. *Chemical Physics Letters* 2020;744:137214.

[64] Neer A, Koylu U. Effect of operating conditions on the size, morphology, and concentration of submicrometer particulates emitted from a diesel engine. *Combustion and Flame* 2006;146(1-2):142-54.

[65] Agarwal AK, Mustafi NN. Real-world automotive emissions: Monitoring methodologies, and control measures. *Renewable and Sustainable Energy Reviews* 2021;137:110624.

[66] Liu J, Wang H, Li Y, Zheng Z, Xue Z, Shang H, et al. Effects of diesel/PODE (polyoxymethylene dimethyl ethers) blends on combustion and emission characteristics in a heavy duty diesel engine. *Fuel* 2016;177:206-16.

[67] Ghadikolaei MA, Wong PK, Cheung CS, Ning Z, Yung K-F, Zhao J, et al. Impact of lower and higher alcohols on the physicochemical properties of particulate matter from diesel engines: A review. *Renewable and Sustainable Energy Reviews* 2021;143:110970.

[68] Kumar S, Cho JH, Park J, Moon I. Advances in diesel–alcohol blends and their effects on the performance and emissions of diesel engines. *Renewable and Sustainable Energy Reviews* 2013;22:46-72.

[69] Geng P, Cao E, Tan Q, Wei L. Effects of alternative fuels on the combustion characteristics and emission products from diesel engines: A review. *Renewable and Sustainable Energy Reviews* 2017;71:523-34.

[70] Jiang Z, Gan Y, Ju Y, Liang J, Zhou Y. Experimental study on the electrospray and combustion characteristics of biodiesel-ethanol blends in a meso-scale combustor. *Energy* 2019;179:843-9.

[71] Zhou Y, Gan Y, Gou X. Chemical kinetic modeling study of methyl esters oxidation: Improvement on the prediction of early CO_2 formation. *Fuel* 2020;279:118383.

[72] Zhou Y, Gan Y, Zhang C, Shi D, Jiang Z, Luo Y. Numerical study for influence of ozone on the combustion of biodiesel surrogates in a homogeneous charge compression ignition engine. *Fuel Processing Technology* 2022;225:107039.

[73] Burger J, Siegert M, Ströfer E, Hasse H. Poly(oxymethylene) dimethyl ethers as components of tailored diesel fuel: Properties, synthesis and purification concepts. *Fuel* 2010;89(11):3315-9.

[74] Awad OI, Ma X, Kamil M, Ali OM, Ma Y, Shuai S. Overview of polyoxymethylene dimethyl ether additive as an eco-friendly fuel for an internal combustion engine: Current application and environmental impacts. *Science of The Total Environment* 2020;715:136849.

[75] He J, Chen H, Su X, Xie B, Li Q. Combustion study of polyoxymethylene dimethyl ethers and diesel blend fuels on an optical engine. *Energies* 2021;14(15):4608.

[76] Zhu Q, Zong Y, Yu W, Yang W, Kraft M. Understanding the blending effect of polyoxymethylene dimethyl ethers as additive in a common-rail diesel engine. *Applied Energy* 2021;300:117380.

[77] Palazzo N, Zigan L, Huber FJT, Will S. Impact of oxygenated additives on soot properties during diesel combustion. *Energies* 2020;14(1):147.

[78] Preuß J, Munch K, Denbratt I. Performance and emissions of renewable blends with OME_{3-5} and HVO in heavy duty and light duty compression ignition engines. *Fuel* 2021;303:121275.

[79] Härtl M, Seidenspinner P, Jacob E, Wachtmeister G. Oxygenate screening on a heavy-duty diesel engine and emission characteristics of highly oxygenated oxymethylene ether fuel OME_1. *Fuel* 2015;153:328-35.

[80] Lautenschütz L, Oestreich D, Seidenspinner P, Arnold U, Dinjus E, Sauer J. Physico-chemical properties and fuel characteristics of oxymethylene dialkyl ethers. *Fuel* 2016;173:129-37.

[81] Zhang X, Kumar A, Arnold U, Sauer J. Biomass-derived oxymethylene ethers as diesel additives: A thermodynamic analysis. *Energy Procedia* 2014;61:1921-4.

[82] Held M, Tönges Y, Pélerin D, Härtl M, Wachtmeister G, Burger J. On the energetic efficiency of producing polyoxymethylene dimethyl ethers from CO_2 using

electrical energy. *Energy & Environmental Science* 2019;12(3):1019-34.

[83] Liu H, Wang Z, Wang J, He X, Zheng Y, Tang Q, et al. Performance, combustion and emission characteristics of a diesel engine fueled with polyoxymethylene dimethyl ethers ($PODE_{3-4}$)/ diesel blends. *Energy* 2015;88:793-800.

[84] Han D, Cao Z, Shi W, Deng X, Yang T. Influence of polyoxymethylene dimethyl ethers on diesel fuel properties. *Energy Sources, Part A: Recovery, Utilization, and Environmental Effects* 2016;38(18):2687-92.

[85] Jin C, Zhang X, Wang X, Xiang Y, Cui X, Yin Z, et al. Effects of polyoxymethylene dimethyl ethers on the solubility of ethanol/diesel and hydrous ethanol/diesel fuel blends. *Energy Science & Engineering* 2019;7(6):2855-65.

[86] Jin C, Zhang X, Geng Z, Pang X, Wang X, Ji J, et al. Effects of various co-solvents on the solubility between blends of soybean oil with either methanol or ethanol. *Fuel* 2019;244:461-71.

[87] Li X, Yu H, Sun Y, Wang H, Guo T, Sui Y, et al. Synthesis and application of polyoxymethylene dimethyl ethers. *Applied Mechanics and Materials* 2014;448:2969-73.

[88] Omari A, Heuser B, Pischinger S, Rüdinger C. Potential of long-chain oxymethylene ether and oxymethylene ether-diesel blends for ultra-low emission engines. *Applied Energy* 2019;239:1242-9.

[89] Yang Z, Ren C, Jiang S, Xin Y, Hu Y, Liu Z. Theoretical predictions of compatibility of polyoxymethylene dimethyl ethers with diesel fuels and diesel additives. *Fuel* 2022;307:121797.

[90] Luo Z, Jiang J. Molecular dynamics and dissipative particle dynamics simulations for the miscibility of poly (ethylene oxide)/poly (vinyl chloride) blends. *Polymer* 2010;51(1):291-9.

[91] Gupta J, Nunes C, Vyas S, Jonnalagadda S. Prediction of solubility parameters and miscibility of pharmaceutical compounds by molecular dynamics simulations. *The Journal of Physical Chemistry B* 2011;115(9):2014-23.

[92] Ghazipour H, Gutiérrez A, Mohammad-Aghaie D, Alavianmher MM, Hosseini SM, Aparicio S. Insights on biodiesel blends with alkanol solvents. *Journal of Molecular Liquids* 2021;332:115864.

[93] Oliveira IPd, Caires ARL. Molecular arrangement in diesel/biodiesel blends: A molecular dynamics simulation analysis. *Renewable Energy* 2019;140:203-11.

[94] Oliveira IPd, Caires ARL, Baskar K, Ponnusamy S, Lakshmanan P, Veerappan V. Biodiesel as an additive for diesel-ethanol (diesohol) blend: physical-chemical parameters and origin of the fuels' miscibility. *Fuel* 2020;263:116753.

[95] Požar M, Lovrinčević B, Zoranić L, Primorać T, Sokolić F, Perera A. Micro-heterogeneity versus clustering in binary mixtures of ethanol with water or alkanes. *Physical Chemistry Chemical Physics* 2016;18(34):23971-9.

[96] Kim S. Issues on the choice of a proper time step in molecular dynamics. *Physics Procedia* 2014;53:60-2.

[97] Berendsen HJC, Postma JPMv, Van Gunsteren WF, DiNola A, Haak JR. Molecular dynamics with coupling to an external bath. *The Journal of chemical physics* 1984;81(8):3684-90.

[98] Hünenberger PH. Thermostat algorithms for molecular dynamics simulations. *Advanced computer simulation* 2005:105-49.

[99] Andersen HC. Molecular dynamics simulations at constant pressure and/or temperature. *The Journal of chemical physics* 1980;72(4):2384-93.

[100] Nosé S. A unified formulation of the constant temperature molecular dynamics methods. *The Journal of chemical physics* 1984;81(1):511-9.

[101] Hoover WG. Canonical dynamics: Equilibrium phase-space distributions. *Physical review A* 1985;31(3):1695.

[102] Frenkel D, Smit B, Ratner MA. Understanding molecular simulation: from algorithms to applications. Academic press San Diego; 1996.

[103] Verlet L. Computer "experiments" on classical fluids. I. Thermodynamical properties of Lennard-Jones molecules. *Physical review* 1967;159(1):98.

[104] Van Gunsteren WF, Berendsen HJC. A leap-frog algorithm for stochastic dynamics. *Molecular Simulation* 1988;1(3):173-85.

[105] Swope WC, Andersen HC, Berens PH, Wilson KR. A computer simulation method for the calculation of equilibrium constants for the formation of physical clusters of molecules: Application to small water clusters. *The Journal of chemical physics* 1982;76(1):637-49.

[106] Cornell WD, Cieplak P, Bayly CI, Gould IR, Merz KM, Ferguson DM, et al. A second generation force field for the simulation of proteins, nucleic acids, and organic molecules J. Am. Chem. Soc. *Journal of the American Chemical Society* 1996;118(9):2309-.

[107] Jorgensen WL, Maxwell DS, Tirado-Rives J. Development and testing of the OPLS all-atom force field on conformational energetics and properties of organic liquids. *Journal of the American Chemical Society* 1996;118(45):11225-36.

[108] Vanommeslaeghe K, Hatcher E, Acharya C, Kundu S, Zhong S, Shim J, et al. CHARMM general force field: A force field for drug-like molecules compatible with the CHARMM all - atom additive biological force fields. *Journal of computational chemistry* 2010;31(4):671-90.

[109] Martin MG, Siepmann JI. Transferable potentials for phase equilibria. 1. United-atom description of n-alkanes. *The Journal of Physical Chemistry B* 1998;102(14):2569-77.

[110] Rappe AK, Goddard Iii WA. Charge equilibration for molecular dynamics simulations. *The Journal of Physical Chemistry* 1991;95(8):3358-63.

[111] Van Duin ACT, Dasgupta S, Lorant F, Goddard WA. ReaxFF: A reactive force field for hydrocarbons. *The Journal of Physical Chemistry A* 2001;105(41):9396-409.

[112] Mueller JE, Van Duin ACT, Goddard WA. Application of the ReaxFF reactive force field to reactive dynamics of hydrocarbon chemisorption and decomposition. *The Journal of Physical Chemistry C* 2010;114(12):5675-85.

[113] Chen C, Volpe R, Jiang X. A molecular investigation on lignin thermochemical conversion and carbonaceous organics deposition induced catalyst deactivation. *Applied Energy* 2021;302:117557.

[114] BIOVIA. Materials Studio. San Diego: Dassault Systèmes.

[115] Chatzigoulas A, Karathanou K, Dellis D, Cournia Z. Nanocrystal: A web-based crystallographic tool for the construction of nanoparticles based on their crystal habit. *Journal of Chemical Information and Modeling* 2018;58(12):2380-6.

[116] So/rensen MR, Voter AF. Temperature-accelerated dynamics for simulation of infrequent events. *The Journal of Chemical Physics* 2000;112(21):9599-606.

[117] Han Y, Ma T, Chen F, Li W, Zhang J. Supercritical water gasification of naphthalene over iron oxide catalyst: A ReaxFF molecular dynamics study. *International Journal of Hydrogen Energy* 2019;44(57):30486-98.

[118] Salmon E, Van Duin ACT, Lorant F, Marquaire P-M, Goddard WA. Early maturation processes in coal. Part 2: Reactive dynamics simulations using the ReaxFF reactive force field on Morwell Brown coal structures. *Organic Geochemistry* 2009;40(12):1195-209.

[119] Martínez L, Andrade R, Birgin EG, Martínez JM. PACKMOL: A package for building initial configurations for molecular dynamics simulations. *Journal of Computational Chemistry* 2009;30(13):2157-64.

[120] Aktulga HM, Fogarty JC, Pandit SA, Grama AY. Parallel reactive molecular dynamics: Numerical methods and algorithmic techniques. *Parallel Computing* 2012;38(4-5):245-59.

[121] Thompson AP, Aktulga HM, Berger R, Bolintineanu DS, Brown WM, Crozier PS, et al. LAMMPS - a flexible simulation tool for particle-based materials modeling at the atomic, meso, and continuum scales. *Computer Physics Communications* 2022;271:108171.

[122] Kabyemela BM, Adschiri T, Malaluan RM, Arai K. Glucose and fructose decomposition in subcritical and supercritical water: Detailed reaction pathway, mechanisms, and kinetics. *Industrial & Engineering Chemistry Research* 1999;38(8):2888-95.

[123] Si T, Huang K, Lin Y, Gu M. ReaxFF study on the effect of CaO on cellulose pyrolysis. *Energy & Fuels* 2019;33(11):11067-77.

[124] Chen C, Zhao L, Wang J, Lin S. Reactive molecular dynamics simulations of biomass pyrolysis and combustion under various oxidative and humidity environments. *Industrial & Engineering Chemistry Research* 2017;56(43):12276-88.

[125] Yoshida T, Oshima Y, Matsumura Y. Gasification of biomass model compounds and real biomass in supercritical water. *Biomass and Bioenergy* 2004;26(1):71-8.

[126] Ding N, Azargohar R, Dalai AK, Kozinski JA. Catalytic gasification of cellulose and pinewood to H_2 in supercritical water. *Fuel* 2014;118:416-25.

[127] Peters W, Seidel A, Herzog S, Bösmann A, Schwieger W, Wasserscheid P. Macrokinetic effects in perhydro-N-ethylcarbazole dehydrogenation and H_2 productivity optimization by using egg-shell catalysts. *Energy & Environmental Science* 2015;8(10):3013-21.

[128] Bühler W, Dinjus E, Ederer HJ, Kruse A, Mas C. Ionic reactions and pyrolysis of glycerol as competing reaction pathways in near- and supercritical water. *The Journal of Supercritical Fluids* 2002;22(1):37-53.

[129] Muroya Y, Yamashita S, Lertnaisat P, Sanguanmith S, Meesungnoen J, Jay-Gerin JP, et al. Rate constant for the $H^{\cdot}+H_2O \rightarrow {}^{\cdot}OH+H_2$ reaction at elevated temperatures measured by pulse radiolysis. *Physical Chemistry Chemical Physics* 2017;19(45):30834-41.

[130] Che F, Ha S, McEwen JS. Catalytic reaction rates controlled by metal oxidation state: C−H bond cleavage in methane over nickel-based catalysts. *Angewandte Chemie* 2017;129(13):3611-5.

[131] Shen DK, Gu S. The mechanism for thermal decomposition of cellulose and its main products. *Bioresource Technology* 2009;100(24):6496-504.

[132] Wu C, Wang Z, Huang J, Williams PT. Pyrolysis/gasification of cellulose, hemicellulose and lignin for hydrogen production in the presence of various nickel-based catalysts. *Fuel* 2013;106:697-706.

[133] Soria FA, Di Valentin C. Reactive molecular dynamics simulations of hydration shells surrounding spherical TiO_2 nanoparticles: implications for proton-transfer reactions. *Nanoscale* 2021;13(7):4151-66.

[134] Wu C, Liu R. Carbon deposition behavior in steam reforming of bio-oil model compound for hydrogen production. *International Journal of Hydrogen Energy* 2010;35(14):7386-98.

[135] Steinhardt PJ, Nelson DR, Ronchetti M. Bond-orientational order in liquids and glasses. *Physical Review B* 1983;28(2):784-805.

[136] Zhao J, Song W, Xin T, Song Z. Rules of hierarchical melt and coordinate bond to design crystallization in doped phase change materials. *Nature Communications* 2021;12(1).

[137] Yu X, Yu D, Liu F, Han J, Wu J, Xu M. Synergistic effects, gas evolution and ash interaction during isothermal steam co-gasification of biomass with high-sulfur petroleum coke. *Energy* 2022;240:122840.

[138] Liang Y, Wang F, Zhang H, Wang J, Li Y, Li G. A ReaxFF molecular dynamics study on the mechanism of organic sulfur transformation in the hydropyrolysis process of lignite. *Fuel Processing Technology* 2016;147:32-40.

[139] Li Y, Li G, Zhang H, Wang J, Li A, Liang Y. ReaxFF study on nitrogen-transfer mechanism in the oxidation process of lignite. *Fuel* 2017;193:331-42.

[140] Hong D, Li P, Si T, Guo X. ReaxFF simulations of the synergistic effect mechanisms

during co-pyrolysis of coal and polyethylene/polystyrene. *Energy* 2021;218:119553.

[141] Kowalik M, Ashraf C, Damirchi B, Akbarian D, Rajabpour S, Van Duin ACT. Atomistic scale analysis of the carbonization process for C/H/O/N-based polymers with the reaxff reactive force field. *The Journal of Physical Chemistry B* 2019;123(25):5357-67.

[142] Li X, Zheng M, Ren C, Guo L. ReaxFF molecular dynamics simulations of thermal reactivity of various fuels in pyrolysis and combustion. *Energy & Fuels* 2021;35(15):11707-39.

[143] Evans DJ, Holian BL. The nose-hoover thermostat. *The Journal of chemical physics* 1985;83(8):4069-74.

[144] Damhus T, Hartshorn RM, Hutton AT. Nomenclature of inorganic chemistry: IUPAC recommendations 2005. *Chemistry International* 2005.

[145] Yu M, Chen C, Xing Z, Jiang X. ReaxFF molecular dynamics simulation of nickel catalysed gasification of cellulose in supercritical water. *International Journal of Hydrogen Energy* 2022.

[146] Russo C, Tregrossi A, Ciajolo A. Dehydrogenation and growth of soot in premixed flames. *Proceedings of the Combustion Institute* 2015;35(2):1803-9.

[147] Wei L, Wen L, Yang T, Zhang N. Nitrogen transformation during sewage sludge pyrolysis. *Energy & Fuels* 2015;29(8):5088-94.

[148] Liu H, Wang Z, Zhang J, Wang J, Shuai S. Study on combustion and emission characteristics of Polyoxymethylene Dimethyl Ethers/diesel blends in light-duty and heavy-duty diesel engines. *Applied Energy* 2017;185:1393-402.

[149] Bekker H, Berendsen H, Dijkstra E, Achterop S, Vondrumen R, Vanderspoel D, et al. Gromacs-a parallel computer for molecular-dynamics simulations. *4th International Conference on Computational Physics (PC 92).* World Scientific Publishing; 1993:252-6.

[150] Chandran P, Shah JK. A molecular simulation approach to the computation of mutual solubility of water and organic liquids: Application to fatty acids. *Fluid Phase Equilibria* 2018;472:48-55.

[151] Vermaas JV, Crowley MF, Beckham GT. Molecular lignin solubility and structure in organic solvents. *ACS Sustainable Chemistry & Engineering* 2020;8(48):17839-50.

[152] Zhang J, Seyyedi M, Clennell MB. Molecular dynamics simulation of transport and structural properties of CO_2-alkanes. *Energy & Fuels* 2021;35(8):6700-10.

[153] Chen C, Jiang X. Transport property prediction and inhomogeneity analysis of supercritical n-Dodecane by molecular dynamics simulation. *Fuel* 2019;244:48-60.

[154] Garrido NM, Jorge M, Queimada AJ, Gomes JRB, Economou IG, Macedo EA. Predicting hydration Gibbs energies of alkyl-aromatics using molecular simulation: a comparison of current force fields and the development of a new parameter set for accurate solvation data. *Physical Chemistry Chemical Physics* 2011;13(38):17384.

[155] Sonibare K, Rathnayaka L, Zhang L. Comparison of CHARMM and OPLS-aa

forcefield predictions for components in one model asphalt mixture. *Construction and Building Materials* 2020;236:117577.

[156] Darden T, York D, Pedersen L. Particle mesh Ewald: An N · log(N) method for Ewald sums in large systems. *The Journal of Chemical Physics* 1993;98(12):10089-92.

[157] Hess B, Bekker H, Berendsen HJC, Fraaije JGEM. LINCS: A linear constraint solver for molecular simulations. *Journal of computational chemistry* 1997;18(12):1463-72.

[158] Bussi G, Donadio D, Parrinello M. Canonical sampling through velocity rescaling. *The Journal of Chemical Physics* 2007;126(1):014101.

[159] Berendsen HJC, Postma JPM, Van Gunsteren WF, Dinola A, Haak JR. Molecular dynamics with coupling to an external bath. *The Journal of Chemical Physics* 1984;81(8):3684-90.

[160] Humphrey W, Dalke A, Schulten K. VMD: Visual molecular dynamics. *Journal of Molecular Graphics* 1996;14(1):33-8.

[161] Shirley WIS, Pluhackova K, Böckmann RA. Optimization of the OPLS-AA force field for long hydrocarbons. *Journal of Chemical Theory and Computation* 2012;8(4):1459-70.

[162] Dodda LS, Vilseck JZ, Tirado-Rives J, Jorgensen WL. 1.14*CM1A-LBCC: Localized bond-charge corrected CM1A charges for condensed-phase simulations. *The Journal of Physical Chemistry B* 2017;121(15):3864-70.

[163] Kulkarni A, García EJ, Damone A, Schappals M, Stephan S, Kohns M, et al. A force field for poly(oxymethylene) dimethyl ethers (OME_n). *Journal of Chemical Theory and Computation* 2020;16(4):2517-28.

[164] Wang X, Pan J, Wu J, Liu Z. Surface tension of dimethoxymethane and methyltert-butyl ether. *Journal of Chemical & Engineering Data* 2006;51(4):1394-7.

[165] Burger J, Ströfer E, Hasse H. Production process for diesel fuel components poly(oxymethylene) dimethyl ethers from methane-based products by hierarchical optimization with varying model depth. *Chemical Engineering Research and Design* 2013;91(12):2648-62.

[166] Lide DR. Handbook of chemistry and physics. Internet Version 2005 ed. Boca Raton: CRC press; 2005.

[167] O’Neil MJ. the Merck Index: An Encyclopedia of Chemicals, Drugs,and Biologicals. 15th ed. Cambridge, UK: Royal Society of Chemistry; 2013.

[168] Yaws CL. Thermophysical properties of chemicals and hydrocarbons. William Andrew; 2008.

[169] Muzet N, Engler E, Wipff G. Demixing of binary water-chloroform mixtures containing ionophoric solutes and ion recognition at a liquid-liquid interface: A molecular dynamics study. *The Journal of Physical Chemistry B* 1998;102(52):10772-88.

[170] Biswas R, Ghosh P, Banerjee T, Ali SM, Singha Deb AK. Interfacial behavior of

Cs+, K+, Na+, and Rb+extraction in the presence of Dibenzo-18-Crown-6 from the Nitrobenzene–water biphasic system: Experimental, quantum chemical, and molecular dynamic studies. *ACS Omega* 2018;3(2):1663-74.

[171] Baaden M, Burgard M, Wipff G. TBP at the water-oil interface: The effect of TBP concentration and water acidity investigated by molecular dynamics simulations. *The Journal of Physical Chemistry B* 2001;105(45):11131-41.

[172] Kaplan IG. Intermolecular interactions: physical picture, computational methods and model potentials. John Wiley & Sons; 2006.

[173] Martínez L, Shimizu S. Molecular interpretation of preferential interactions in protein solvation: A solvent-shell perspective by means of minimum-distance distribution functions. *Journal of Chemical Theory and Computation* 2017;13(12):6358-72.

[174] Martínez L. ComplexMixtures.jl: Investigating the structure of solutions of complex-shaped molecules from a solvent-shell perspective. *Journal of Molecular Liquids* 2021:117945.

[175] Cheng Z, Xu W, Tang L. Theory and practice of molecular modeling. Beijing: Chemical Industry Press; 2007.

[176] Liu W, Li W, Jiang H, Yu H. Fates of chemical elements in biomass during its pyrolysis. *Chemical Reviews* 2017;117(9):6367-98.

[177] Unke OT, Chmiela S, Sauceda HE, Gastegger M, Poltavsky I, Schütt KT, et al. Machine learning force fields. *Chemical Reviews* 2021;121(16):10142-86.

[178] Poltavsky I, Tkatchenko A. Machine learning force fields: Recent advances and remaining challenges. *The Journal of Physical Chemistry Letters* 2021;12(28):6551-64.